Nanoparticle Drug Delivery to Brain Tumors: From Intravenous to Intrathecal

by

Kyle Thomas Householder

A Dissertation Presented in Partial Fulfillment
of the Requirements for the Degree
Doctor of Philosophy

Approved June 2018 by the
Graduate Supervisory Committee:

Rachael W. Sirianni, Chair
Sarah Stabenfeldt
Brent Vernon
Michael Caplan
Robert Wechsler-Reya

ARIZONA STATE UNIVERSITY

August 2018

ABSTRACT

Achieving effective drug concentrations within the central nervous system (CNS) remains one of the greatest challenges for the treatment of brain tumors. The presence of the blood-brain barrier and blood-spinal cord barrier severely restricts the blood-to-CNS entry of nearly all systemically administered therapeutics, often leading to the development of peripheral toxicities before a treatment benefit is observed. To circumvent systemic barriers, intrathecal (IT) injection of therapeutics directly into the cerebrospinal fluid (CSF) surrounding the brain and spinal cord has been used as an alternative administration route; however, its widespread translation to the clinic has been hindered by poor drug pharmacokinetics (PK), including rapid clearance, inadequate distribution, as well as toxicity. One strategy to overcome the limitations of free drug PK and improve drug efficacy is to encapsulate drug within nanoparticles (NP), which solubilize hydrophobic molecules for sustained release in physiological environments. In this thesis, we will develop NP delivery strategies for brain tumor therapy in two model systems: glioblastoma (GBM), the most common and deadly malignant primary brain tumor, and medulloblastoma, the most common pediatric brain tumor. In the first research chapter, we developed 120 nm poly(lactic acid-co-glycolic acid) NPs encapsulating the chemotherapy, camptothecin, for intravenous delivery to GBM. NP encapsulation of camptothecin was shown to reduce the drug's toxicity and enable effective delivery to orthotopic GBM. To build off the success of intravenous NP, the second research chapter explored the utility of 100 nm PEGylated NPs for use with IT administration. Using *in vivo* imaging and *ex vivo* tissue slices, we found the NPs were rapidly transported by the convective forces of the CSF along the entire neuraxis and were retained for over 3 weeks. Based on their wide spread delivery and prolonged circulation, we examine the ability of the NPs to localize with tumor lesions in a

leptomeningeal metastasis (LM) model of medulloblastoma. NPs administered to LM bearing mice were shown to penetrate into LM mets seeded within the meninges around the brain. These data show the potential to translate our success with intravenous NPs for GBM to improve IT chemotherapy delivery to LM.

DEDICATION

First, I want to express my love and gratefulness to my girlfriend Tristan. Whether it was a “Thibodeau peptalk”, nourishing meal, or just a sympathetic ear to vent to, you always stayed by my side and gave me all the support you could. We have been through some stressful times these past 3 years and there will more to come, but I feel ready and excited to face them together. Houston, let’s start an adventure!

To my Family, thank you for all for being my greatest role models and always providing your support. I know I will always be the “baby” of the family but I am also now the only doctor of the family. To Mom and Dad, thank you for teaching me to explore, create, and challenge the world around me and for always reminding me to learn from my failures. I would not be where I am today without the opportunities you provided and your continued love and guidance.

To my AZ FRamily, Kyle, Tyler, Krystal, John, Trent, and Landmine (an eclectic group to say the least) thank you for being the unique, kind, generous and amazing people you are. I cannot express all the ways you have each supported me and helped me grow. To the Garfield House, everyone thought we were crazy to live together (and maybe we were), but I would never give the time or friendships back for anything else. To Christian, Laura, and Sergio, thank you for the friendship and memories made out on the rock. Lastly, I would like to thank Dr. Kelsey Potter and Dr. Jeffrey Capadona. Without your mentorship as an undergrad, I would not have found my passion for research and the brain.

ACKNOWLEDGMENTS

My sincerest gratitude to my adviser Dr. Rachael Sirianni for being an amazing boss, mentor and friend over the past 5 years. Thank you for always being available no matter what and providing guidance when needed while still allowing me to explore **many** diverse topics. Thank you for every challenge you presented me and especially for helping me improve my communication skills. I admire your work/life balance and willingness to share the gritty topics others hide. You have been an exceptional role model to me, both in and out of the lab. I cannot fully express all that your guidance has done or meant to me, but I know any student is lucky to work and learn from you. I wish you the best and can't wait to see where the lab goes next!

I would also like to acknowledge my committee members Drs. Sarah Stabenfeldt, Robert Wechsler-Reya, Brent Vernon and Michael Caplan. Thank you all for your guidance and patience in developing my thesis, and for continually challenging me to analyze and push the science one step further. I appreciate all of your help and support in my academic achievements.

A big thank you to all of the Sirianni Lab members who made this work possible. The lab was always a place of collaboration and support for both scientific and professional growth. I would especially like to thank the undergraduate students, Eugene, Greg, Regina, Justine, Sara and Shruti, I had the privilege of mentoring over the years. It has been truly rewarding experiences seeing each of you grow as a scientist. Thank you all for your hard work on these projects and for teaching me every day.

Lastly, I would like to acknowledge the generous funding provided by Arizona State University, the Achievement Rewards for College Scientists Foundation, Ben and Dawn Senger, the Ben and Catherine Ivy Foundation and the Barrow Neurological

Foundation. Thank you for supporting my research and enabling me to present this work at numerous academic conferences.

TABLE OF CONTENTS

Page

CHAPTER Page

LIST OF FIGURES

Figure Page

PREFACE

This dissertation includes an original research article published by the primary author. Chapter 2 describes the formulation of polymeric nanoparticles for the solubilization and delivery of camptothecin to orthotopic glioblastoma tumors[1]. The use of these previously published works was approved by all co-authors (Appendix A).

CHAPTER 1

Introduction

1.1. Nanoparticle Drug Carriers

Nanoparticles (NP) are colloidal particles ranging in size from 1 to 1000 nm and can be formulated from a variety of diverse materials, including metals[2–4], proteins[5,6], lipids[7,8], viral vectors[9], and polymers[10–12]. The ability to alter and tune their biophysical and biochemical properties has made them a versatile asset in modern medicine and particularly appealing as carriers for therapeutic drug delivery. Due to their favorable biocompatibility and low toxicity, organic polymers and lipids have led the field for NP drug delivery in the clinic[13–15]. Polymeric and lipid based NPs also have the potential to encapsulate and release a wide range of therapeutics, including hydrophilic and hydrophobic small molecule drugs, proteins, and gene therapies[16].

Loading a drug into a NP can offer distinct and significant advantages over utilizing its free form counterpart. While the biophysical properties of many potential drug candidates restrict their compatibility with most or all administration routes, NPs are relatively easily formulated for administration by oral, local, topical, intranasal, and parenteral (intravenous, intramuscular, subcutaneous) routes, with intravenous (IV) administration being the most extensively studied, both clinically and preclinically. For example, paclitaxel's water insolubility is incompatible with IV administration, but solubilization of paclitaxel within albumin [17] or poly(lactic acid)-co-poly(ethylene glycol)[18] NPs enables IV injection and improves both its tolerability and efficacy. The solubilization of drugs within the NP matrix also restricts the interaction of the drug with the body until the drug is released from the NP. This helps protect the body from unwanted side effects associated with the drug, and it protects the drug, especially proteins and genes, from becoming inactivated or degraded within the physiological

environment[19,20]. For example, while free doxorubicin, a potent chemotherapy, is effective across numerous tumor types, use of doxorubicin is associated with severe cardiotoxicity[21]. Doxil, a doxorubicin-loaded liposome, maintains the drug's efficacy but significantly lowers the risk for cardiac toxicity and allows for more opportunities for combination treatments[22]. Importantly, Doxil and many NP formulations also exhibit prolonged circulation compared to their free drug form[23–25]. Thus, drug encapsulation within NPs can improve efficacy and tolerability through multiple mechanisms, depending on the limitations imposed by the drug's biophysical properties.

1.1.1. Nanoparticle Design Considerations

To maximize the benefit of NP encapsulation, the biophysical properties of the nanocarrier itself must be considered. The ideal set of NP properties for a given drug will change depending on the barriers presented to the NP based on target tissue and delivery route. Despite these differences, across tissues and administration routes, the size of the NP, surface charge, mechanism of drug release and targeting are key design considerations known to drastically alter the efficacy of NP therapies[26–29].

NP size is well documented to be a critical biophysical property governing the fate of NPs following administration by most routes, including IV[30–32], oral[33,34], intranasal[35,36], and convection enhanced delivery (CED)[37,38]. The extent and manner by which size affects distribution for each route varies greatly, including the size range that would be expected to optimize NP distribution. For example, NP size has a particularly strong effect on the rate of NP clearance following IV injection[32,39,40], which in turn can significantly alter organ localization[31]. A NP size between 30 and 150 nm is typically considered ideal for IV administration. This is due to relatively strict size cutoffs imposed by the filtration organs and immune system. At the lower end, NPs <10 nm in size are rapidly filtered by the kidneys for renal excretion, while NPs in the 10-20 nm range

experience accelerated liver filteration[40]. Above 200 nm, NPs circulation is significantly reduced due to increased phagocytosis and clearance by the reticulo-endothelial system[41]. Comparatively, size has shown a relatively minimal effect on orally administered NPs. Since the GI tract does not exhibit size dependent clearance mechanisms that are observed for intravenous routes of delivery, the clearance and overall efficacy of orally administered NPs is reported to be more dependent on the mucoadhesive surface properties of the NP[34]. However, given the same adhesion properties, decreasing NP size can improve efficacy via better penetration through the mucosal lining of the intestines[33]. NP size is known to alter NP distribution, regardless of delivery route, and engineering the best NP requires understanding the magnitude and types of effects imposed.

Surface charge (zeta potential) is a key parameter dictating NP interactions with proteins and cells for all routes of administration. Applications requiring high intracellular NP delivery, like gene therapy, favor the use of cationic NPs, which promote cellular uptake due to the negative charge of cellular membrane lipids[42,43]. Similarly, cationic NPs are desired for intranasal and oral administration, where the positive charge significantly prolongs their retention within the negatively charged mucus of the nose and GI tract[34,44,45]. In contrast, the success of IV and CED administered NP heavily relies on their ability to avoid non-specific cellular and protein interactions[38,46–50]. Generally, a large positive or negative surface charge promotes NP-protein interactions, while a near neutral (-10 to +10 mV) charge significantly reduces protein adsorption[51,52]. Thus, NPs are frequently surface coated with poly(ethylene glycol) or other molecules to create a hydrophilic, near neutral layer around the NP, which can improve the distribution of NPs administered by either CED or IV. CED utilizes the convective forces of the infusion to drive NP movement through the extracellular space. The addition of a

dense PEG layer significantly reduces NP-extracellular matrix interactions, enabling the NPs to reach a larger volume of distribution[47,50]. For IV NPs, the adsorption of serum proteins, especially opsonins, to the NP surface increases the phagocytosis and clearance of NPs by the mononuclear phagocyte system. PEGylated surfaces resist the deposition of these proteins on the NP surface, which leads to significantly longer circulation times compared to their non-PEGylated counterparts[46,53,54]. For example, Klibanov et al. showed PEGylation of their liposomal nanoparticles increased the circulation half-life from 30 min to 5 hours[24]. These results exemplify the potent effects of surface properties on the NP's interaction with the cells and proteins of its environment and the resulting changes to their distribution.

Further modifications to the NP surface with peptides[50,55–57], aptamers[58–60] and antibodies[61–63] can be employed to increase NP interactions with a specific target. The efficacy of these targeting strategies is thought to be determined by a combination of factors, including the specificity and affinity of the moiety for its target, how unique the target is to the cell or tissue of interest, and accessibility of the NP to the target[28,55,64]. Technologies like bacteriophage biopanning and systematic evolution of ligands by exponential enrichment (SELEX), along with advances in antibody design, have allowed for the identification of new moieties with high affinity and specificity for unique targets[65–68]. Incorporation of targeting ligands onto the surface of NP can improve NP efficacy through increase carrier retention and payload delivery within specific tissues[65,69,70], enhance NP internalization[71,72] or direct NP fate to specific intracellular organelles[73,74]. Although NP size and surface charge are thought to have the greatest effect on overall NP distribution, the addition of targeting ligands has received significant attention to improve NP specificity, reduce off-target delivery and overcome biological barriers to NP delivery.

The efficacy of NPs relies upon efficient release of drug at the target site. In the ideal scenario drug would only be released after reaching the desired target tissue. Towards this goal, drug release from NP carriers can be modified to occur passively over minutes to weeks[75–79]. If the drug release is too rapid, the benefit of prolonged NP circulation is lost. If the release is too slow, the NPs will be cleared before the therapy is delivered. For example, cisplatin-loaded liposomes showed reduced off target side effects and nearly 5-fold increased tumor accumulation compared to free cisplatin[80], which would be expected to provide improved efficacy. However, the rate of cisplatin release from the liposomes was so slow that a therapeutically relevant concentration of free drug is not achieved within the tumor. Thus to engineer NP drug systems for maximal efficacy, it is necessary tune drug release with an understanding of the pharmacokinetics of the carrier itself.

Despite extensive studies to characterize the key NP biophysical parameters necessary to enable successful IV administration and improve drug distribution, NP design and use for intrathecal (IT) administration remains poorly characterized. Polymeric and liposomal drug carriers have been utilized successfully for IT therapy to overcome the rapid clearance of hydrophilic therapies[81–86], although most studies were centered on their use as sustained release depots for local delivery to injured spinal cord. In the context of chemotherapies, DepoCyt, a 10 μm liposomal system, is FDA approved (1999) for lymphomatous meningitis from leukemia. DepoCyt successfully provides sustained release of cytarabine, requiring only a single injection every 2 weeks compared to twice weekly for free drug. However, it does not alter cytarabine's overall distribution along the neuraxis, which is reflected in its equivalent clinical treatment response compared to free drug[101,110–113]. DepoCyt's large microscopic size means its efficacy must rely on the release and subsequent movement of the drug to the cancer cells, limiting its

utility for delivering lipophilic compounds. These studies show the feasibility and safety of drug carriers for IT administration, but additional work is needed to characterize the effects of key biophysical properties on NP distribution after IT injection.

1.2. Cerebrospinal Fluid System

The cerebrospinal fluid (CSF) system includes the cerebral ventricles, perivascular spaces, and the brain and spinal cord subarachnoid spaces. The subarachnoid space (SAS) lies between the arachnoid and pia mater meninges and is spanned by a mesh-like network of collagen trabeculae[92,93]. CSF is a clear, mainly acelluar, electrolyte rich fluid produced by the choroid plexus within the lateral ventricles of the brain. The flow of CSF out through the 4th ventricle into the cisterna magna and throughout the SAS plays a critical role in maintaining homeostasis through regulation of electrolytes, transport of neuro-active molecules, and elimination of metabolites[93–95] . The pulsatile forces generated by our cardiac and respiratory cycles cause an ebb and flow movement of the CSF, while interactions with microanatomies of the SAS, such as trabeculae and nerves, are thought to produce local vortices of CSF mixing[92,96–98]. CSF exits the SAS into the periphery either directly into blood through the arachnoid villi, or into the lymphatic system through the nasal cribriform plate and along spinal nerve roots[94]. The constant production and adsorption of CSF leads to complete turnover of the CSF volume 4 times per day in humans, and 12 times per day in mice[95,99]. Although CSF is rapidly turned over, the circulation of CSF throughout the entire CNS maintains it as an attractive delivery medium for neurological therapies.

1.3. Leptomeningeal Metastasis in Medulloblastoma

Medulloblastoma (MB) arises in the cerebellum and is the most common malignant pediatric brain tumor[100]. The overall 5-year survival across all 4 medulloblastoma (MB) subtypes is about 85%, but survival drops to 60% for patients

exhibiting leptomeningeal metastasis (LM). LM is characterized by the spread of tumor cells through the cerebrospinal fluid (CSF) to the meninges surrounding the brain and spinal cord[100–102]. The Group 3 subtype of MB has the highest incidence of LM at approximately 50% and is also associated with the lowest 5-year survival at only 32%[100]. Because LM is not typically accessible for resection, treatment consists of a combination of one or more modalities, including radiation, intrathecal (IT) chemotherapy, and high-dose systemic chemotherapy. Although radiation of the cerebellar-spinal axis improves survival outcomes, severe long-term side effects, including cognitive deficits, endocrine disorders, and secondary malignancies, have driven efforts to reduce radiation doses in favor of other treatments[103–105]. Similarly, debilitating peripheral organ toxicities often occur from the high-doses of chemotherapy required to overcome the limited central nervous system (CNS) penetration of systemic agents past the blood-brain and blood-CSF barriers[106,107]. Thus, new therapies for the treatment of LM are desperately needed to reduce peripheral chemotherapy and CNS radiation related toxicities.

1.4. Intrathecal Chemotherapy

IT chemotherapy is an appealing alternative to IV or oral administration for LM therapy, since compounds administered IT bypass the blood-CSF barrier and achieve high drug concentrations within the CSF at a fraction of the systemic dose[108,109]. Additionally, the continuous pulsatile movement of the CSF throughout the SAS provides convective forces to disburse drugs along the neuraxis[96–98,110], where they would have potential to directly interact with LM lesions. However, the widespread adoption of IT administration for chemotherapy has been significantly limited by the incompatibility of most potential drug candidates due to their biophysical properties[111–113].

Chemotherapies suitable for intrathecal administration are described to require a lack of neurotoxicity following systemic administration and adequate water solubility for

injection[114–116]. Currently, only four chemotherapies are FDA approved for IT administration, specifically for the treatment of leukemia that has spread to the CNS[117–120]. Two therapies, methotrexate and cytarabine, are often used off-label in the treatment of MB, mainly due to their compatibility with IT use. Methotrexate and cytarabine work as antimetabolites for nucleotides to inhibit DNA replication but are only effective in the S-phase of the cell cycle. While their hydrophilicity enables them to be distributed by CSF movement, it also results in their rapid clearance with the turnover of CSF[95,121]. Their mechanism of action and cell cycle dependency require prolonged high concentrations exposure to kill cancer cells. In order to maintain of adequate concentrations of hydrophilic chemotherapies, patients must receive lumber injections 2-3x per week or have an additional invasive surgery to implant a subcutaneous Ommaya Reservoir with an intraventricular catheter[91,119]. Still, the clinical benefit of current IT chemotherapy for treating LM is debated[116,122].

Lipophilic chemotherapies are typically incompatible with IT administration due to toxicity and lack of efficacy[116,119,123]. Both phenomena are believed to result from a lack of distribution away from the injection site. Their lipophilicity causes the drugs to rapidly get cleared to systemic circulation or enter nearby parenchymal cells before they can be distributed by the CSF[124,125]. Incompatibility with IT administration severely limits the chemotherapy options available for the treatment of LM, and new technologies are desperately needed to overcome the pharmacokinetic limitations of lipophilic chemotherapies.

1.5. Overview and Specific Aims

The versatility of NP properties allows them to be rationally designed for the encapsulation of a wide range of therapeutics and their subsequent delivery by nearly any administration route. In this work, we aim to develop NP delivery strategies for the

treatment of 2 brain tumor models, glioblastoma and medulloblastoma. The first research chapter we focus on the development of an intravenous NP system for delivery to orthotopic glioblastoma. In the second and third chapters, we aim to build upon the success and lessons learned from the use of intravenous NPs to begin to elucidate the key parameters in deciding NP fate after IT administration. Our central hypothesis is IT administered NPs will be transported by the convective flow of CSF to enable wide spread delivery along the neuraxis and to LM, and that NP fate will depend upon NP size and surface properties. The long-term goal of these studies is to define the key NP biophysical properties to enable effective IT delivery of lipophilic chemotherapies for the treatment of LM in MB. We address this hypothesis in the following chapters through the testing of these specific aims:

1.5.1. Specific Aim 1

Test the capacity of NPs to solubilize and enable the effective IV delivery of an otherwise intolerable lipophilic chemotherapy.

1.5.2. Specific Aim 2

Characterize the ability of NPs to be distributed by the convective flow of CSF to identify engineering opportunities for the design of IT NP systems.

1.5.3. Specific Aim 3

Identify a targeting ligand for LM cells and investigate the ability of targeting to alter NP fate after CSF administration.

CHAPTER 2

Intravenous Delivery of Camptothecin-loaded PLGA Nanoparticles for the Treatment of Intracranial Glioma

2.1. Abstract

Effective treatment of glioblastoma multiforme remains a major clinical challenge, due in part to the difficulty of delivering chemotherapeutics across the blood-brain-barrier. Systemically administered drugs are often poorly bioavailable in the brain, and drug efficacy within the central nervous system can be limited by peripheral toxicity. Here, we investigate the ability of systemically administered poly (lactic-co-glycolic acid) nanoparticles (PLGA NPs) to deliver hydrophobic payloads to intracranial glioma. Hydrophobic payload encapsulated within PLGA NPs accumulated at ~10x higher levels in tumor compared to healthy brain. Tolerability of the chemotherapeutic camptothecin (CPT) was improved by encapsulation, enabling safe administration of up to 20mg/kg drug when encapsulated within NPs. Immunohistochemistry staining for γ-H2AFX, a marker for double-strand breaks, demonstrated higher levels of drug activity in tumors treated with CPT-loaded NPs compared to free drug. CPT-loaded NPs were effective in slowing the growth of intracranial GL261 tumors in immune competent C57 albino mice, providing a significant survival benefit compared to mice receiving saline, free CPT or low dose CPT NPs (median survival of 36.5 days compared to 28, 32, 33.5 days respectively). In sum, these data demonstrate the feasibility of treating intracranial glioma with systemically administered nanoparticles loaded with the otherwise ineffective chemotherapeutic CPT.

2.2. Introduction

Malignant gliomas are the most common form of primary brain tumors, afflicting as many as 12,000 patients per year in the United States[126,127]. Glioblastoma multiforme

(GBM) tumors, a grade IV astrocytoma, are distinguished by their fast growing and infiltrative nature. Even after aggressive treatment, which includes tumor resection, radiation, and chemotherapy, the median survival for patients diagnosed with GBM is only 12-14 months [128], and few new treatments have advanced to the clinic in the past three decades.

One major challenge to achieving better treatment of GBM is the difficulty of delivering drugs across the blood-brain barrier (BBB), a network of endothelial cells that present both active and passive barriers to the uptake of systemically delivered agents. Chemotherapeutics capable of crossing the BBB are typically poorly soluble and may clear rapidly, and thus high systemic doses are needed to achieve efficacy. This large systemic dose can often have severe toxic effects on peripheral tissue and organs before a treatment benefit is observed.

Thus, many drugs that could be of interest for treating GBM cannot be delivered in doses that are both effective and safe. For example, camptothecin (CPT), a potent DNA damaging chemotherapeutic, is effective at killing cells in vitro, but failed in clinical trials due to dose-limiting toxicities and, ultimately, poor efficacy. CPT is rapidly hydrolyzed at physiological pH from its active lactone form to a 10-fold less active, more toxic carboxylate form, which is cleared rapidly once bound to plasma proteins [129].

Encapsulation of therapeutics such as CPT in polymeric or liposomal nanoparticles is a one strategy that could be used to improve drug action. Drug that has been encapsulated is effectively solubilized and protected from degradation, which prolongs circulation time and increases bioavailability. For example, poly (lactic-co-glycolic acid) (PLGA) is a biocompatible and biodegradable polymer that can be formed into nanoparticles for encapsulation and sustained release of drug payloads. PLGA nanoparticles are capable of encapsulating a wide range of active agents for sustained

release in biological environments, including CPT [130–132]. CPT potency is improved by encapsulation and sustained release when infused directly into tumors [19,133]. However, the question of whether CPT-loaded PLGA nanoparticles are capable of treating tumors within the brain when administered intravenously remains unanswered.

The goal of this work was to evaluate the ability of systemically administered CPT-loaded PLGA NPs to treat intracranial GBM in mice. GL261 is a syngeneic mouse glioma cell line that mimics many of the proliferative, invasive, and diffuse characteristics of human GBM [134,135]. The use of luciferase expressing GL261 cells allows us to track tumor growth *in vivo* with bioluminescence and, therefore, NP efficacy in immune-competent C57BL/6 albino mice. Nanoparticles were administered to mice bearing orthotopic GL261-Luc2 tumors to evaluate specific payload delivery to tumor, peri-tumor, and healthy brain tissue. Efficacy of free CPT versus CPT encapsulated at two doses was determined by tumor growth and survival to test the hypothesis that encapsulation of chemotherapeutic in a nanoparticle could improve systemic therapy of orthotopic GBM.

2.3. Materials and Methods

2.3.1. Materials

Camptothecin (CPT), 1,1'-Dioctadecyl-3,3,3',3'-Tetramethylindotricarbocyanine Iodide (DiR), dichloromethane (DCM), methanol, dimethyl sulfoxide (DMSO), 10% neutral buffered formalin, E-TOXA-Clean and polyvinyl alcohol (PVA) were all purchased from Sigma-Aldrich (St. Louis, MO, USA). Ester terminated poly (lactic-co-glycolic acid) (PLGA) (50:50; inherent viscosity = 0.59 dL/g) was obtained from Lactel (Birmingham, AL, USA). All water used in nanoparticle fabrication was endotoxin free (<0.0050 EU/ml) purchased from G-biosciences (St. Louis, MO, USA). Dulbecco's modified Eagle medium (DMEM), fetal bovine serum (FBS), 0.25% trypsin-EDTA and

geneticin selective antibiotic (G-418) were purchased from Gibco Invitrogen (Carlsbad, CA, USA). Greiner T25 tissue culture flasks with filter cap and Costar 96 well assay plates (black, flat-bottom, non-treated polystyrene) were purchased from VWR International (Radnor, PA, USA). Beetle luciferin, potassium salt was purchased from Promega (Madison, WI, UAS). GL261-Luc2 cells were a generous gift from Dr. Adrienne Scheck (Barrow Neurological Institute, Phoenix, AZ, USA).

2.3.2. Cell Culture

GL261-luc2 expressing cells were maintained at 37°C and 5% CO2 on T25 tissue cultures flasks in DMEM supplemented with glucose, L-glutamine, 10% FBS and G-418 antibiotic. Cells were detached with 0.25% trypsin-EDTA and counted using a cellometer mini (Nexcelom Bioscience, Lawrence, MA, USA) to obtain a final concentration of 50,000 cells/2 µl for tumor inductions.

2.3.3. Nanoparticle Fabrication

Nanoparticles were fabricated in endotoxin-free conditions. All glassware and centrifuge tubes were soaked overnight in a 1% w/v E-TOXA-Clean solution and glassware was baked at 250° C for 30 min. Nanoparticles were produced by single emulsion-solvent evaporation[136] with slight modification. Briefly, 100 mg of PLGA and either 625 µg DiR or 8 mg CPT was dissolved in 1 ml of a 4:1 DCM: methanol mixture. The dissolved PLGA was added dropwise into 2 ml of 5% (w/v) PVA under vortexing and probe sonicated (Fisher Scientific Model 705 Sonic Dismembrator, Waltham, MA, USA) on ice in 3, 10-second bursts at 40% amplitude. The resulting emulsion was added to 50 ml of 0.3% PVA, and this solution was stirred for 3 hours to evaporate solvent. Nanoparticles were collected by centrifugation for 20 min at 20,000 RCF and the resulting nanoparticle pellet was washed three times with DI water. The final nanoparticle pellet was resuspended in 1 ml endotoxin free water containing 25 mg

Trehalose, frozen, lyophilized for 48 hours, and stored at -80°C. Blank nanoparticles were made by the same method as above without the addition of CPT or DiR.

2.3.4. Nanoparticle Sizing and Morphology

To visualize surface morphology, lyophilized nanoparticles were mounted on double-sided carbon tape and sputter coated with gold for 30s at 40 mA. Samples were imaged on a SEM-XL30 Environmental FEG at 10 kV. Nanoparticle diameters were measured with ImageJ (v. 1.48, NIH) for a minimum of 200 nanoparticles taken from 5 images. The hydrodynamic diameter and zeta potential of nanoparticles were determined at a concentration of 1mg/ml in water by dynamic light scattering (DLS) using a Delsa Nano C (Beckman Coulter, Pasadena, CA, USA).

2.3.5. Drug Loading

Loading of CPT and DiR were determined by fluorescence. Nanoparticles were dissolved in DMSO to a concentration of 5 mg/ml. The nanoparticle solution (40µl) and DMSO (10µl) were pipetted into a black flat bottom 96 well plate and read on a fluorescent plate reader at the appropriate wavelengths (EX/EM 370/428 nm or 750/780 nm, for CPT or DiR respectively). Three samples were read with technical triplicates averaged. Control curves were constructed by dissolving blank nanoparticles as described above and spiking with known amounts of drug or dye.

2.3.6. Controlled Release

The method for measuring release of CPT from nanoparticles was adapted from a method described previously[137]. Nanoparticles (150 µg) with or without CPT were suspended in 2 mL of 1x PBS and incubated at 37°C on a shaker. At regular intervals (0.5, 2, 4, 6, 24 and 48 hours) samples were removed and centrifuged for 10 min at 20,000 RCF. The nanoparticle pellet was discarded and 970 µL of the supernatant was removed and added to 30 µL of quantification fluid (DMSO: 1 N HCL: 10% SDS). Control

curves were constructed by spiking blank particle samples with known quantities of CPT for fluorescent readout by the method described above. Three samples were measured for each time point.

2.3.7. In Vivo Studies

Nanoparticle brain distribution and tumor treatment efficacy were examined *in vivo* in a total of 64 C57BL/6 albino mice (Harlan Laboratories, Indianapolis, IN, USA). All procedures and animal care practices were performed in accordance with the Barrow Neurological Institute's Institutional Animal Care and Use Committee.

2.3.8. Tumor Inductions

Tumor induction protocol followed the methods established by Abdelwahab et al. with some modifications[138]. Mice were anesthetized with an intraperitoneal injection of ketamine (100 mg/Kg) and xylazine (10 mg/Kg) and mounted on a small animal stereotaxic instrument (Model 900, Kopf Instruments, Tujunga, CA, USA). Animal temperature was maintained using a circulating water heating pad placed beneath the frame. A sterile surgical field was obtained by three alternating passes of betadine solution and 70% isopropanol over the surgical site. An incision was made down the midline of the scalp to expose the skull and a burr hole was drilled to target the striatum (2mm lateral and 0.1mm posterior from bregma). A Hamilton syringe filled with 2 μL of the cell suspension (50k cells) was lowered to a depth of 3 mm and allowed to equilibrate with tissue for 1 min. The syringe was then withdrawn to a depth of 2.6 mm and the cells were infused over 2 min. The syringe was left in place for 1 min before it was removed to reduce back flow. The incision was closed using staples and a triple antibiotic ointment was applied to the scalp before placing the animal in a clean cage over a heating pad to recover. All animals received a single subcutaneous (SQ) injection of Buprenorphine (0.1 mg/Kg). Ibuprofen was provided in drinking water for 1 week post-op to control pain.

2.3.9. Tumor Growth

Tumor growth was monitored every 3-4 days after tumor induction using the Xenogen IVIS Spectrum in vivo imaging system (Caliper Life Sciences, Hopkinton, MA, USA). Mice received a SQ injection of 150 mg Luciferin/kg and were imaged under anesthesia (2% isoflurane) at 25 minutes post injection. Regions of interest (ROIs) were drawn by hand to measure total flux (photons/s) using the IVIS Living Image software.

2.3.10. Tumor Localization of Particles

25 tumor bearing C57BL/6 albino mice were used to measure accumulation of payload in tumor, peri-tumor and healthy brain tissue. Mice were imaged on the IVIS system one day prior to injection to determine tumor size. On days 4, 8, 12, 16 or 20, mice (n=5/ day) were injected with DiR-loaded nanoparticles (180 mg/kg) in 0.2mL by tail vein. 2 hours post-injection a blood sample was collected by cardiac puncture before mice were sacrificed and the brain removed, rinsed, and stored at -80°C. Frozen brains were sliced into 2 mm thick sections and imaged on a LI-COR Odyssey CLx (LI-COR Biosciences, Lincoln, NE, USA). After slices were imaged, 2 mm diameter punches were taken from tumor, peri-tumor and healthy (contralateral) striatal regions. The tissue punches were probe sonicated in 2.5% w/v water for 2, 10s bursts (40% amplitude). Tissue homogenates (50 μl) were mixed with DMSO (10 μl) in triplicate in a 96 well plate for fluorescent readout (EX/EM 750/780 nm). Control curves were constructed by processing punches from tumor bearing mice that did not receive nanoparticles (n=8 mice) and spiking with known amounts of DiR.

2.3.11. Tumor Treatment Efficacy

The antitumor efficacy of CPT-loaded PLGA nanoparticles was tested in 31 C57BL/6 albino mice bearing orthotopic GL261-luc2 tumors. Animals were randomized into four treatment groups: saline, free CPT (10 mg/kg CPT), nanoparticle-encapsulated

CPT at a low dose (10 mg/kg CPT) (NP-10), and nanoparticle-encapsulated CPT at a high dose (20 mg/kg CPT) (NP-20). Free CPT was prepared for injection by dissolving CPT (50 mg/ml) in 1 M NaOH and titrating the pH to ~7 with PBS for a final solution of 1 mg/ml CPT. Nanoparticles were prepared for injection by resuspension in sterile saline, and sonicated for 10 min to ensure no aggregates remained (Fisher Scientific Model FS30). Treatments were administered intravenously (IV) by tail vein injection on days 8, 15 and 22 after tumor induction. Treatment efficacy was determined by tumor growth measured by IVIS, as described in 2.4.2, every 3-4 days following tumor induction and differences in mean survival time. Mice were monitored daily and euthanized upon > 15% weight loss or signs of neurological symptoms.

2.3.12. Camptothecin Activity

CPT activity *in vivo* was evaluated using immunohistochemistry (IHC). C57BL/6 albino mice bearing orthotopic GL261-luc2 tumors received an injection of saline, free CPT or NP-20 and were euthanized 2 hours after treatment by cardiac perfusion with heparinized saline followed by 10% buffered formalin. Animal brains from each treatment group were harvested for tissue analysis. Formalin fixed brains were sliced into thick sections and embedded in paraffin. H & E staining and IHC staining were performed as described previously [139]. Briefly, 5 μM thick sections from the tissue blocks were baked at 65°C for 1 hour, deparaffinized in three xylene washes, dehydrated in series graded ethanol, and rehydrated in water. Each slide was blocked in blocking buffer (3% Goat Serum, 1% BSA in PBS) and antigens were retrieved using a sodium citrate buffer (pH 6.5) for 20 minutes (BondMax autostainer; Vision Biosystems, Norwell, MA). IHC staining for γH2A.X (#9718, Cell Signaling Technology) and CD31 (ab28364, Abcam) was performed on serial sections from tissue blocks. Slides were incubated with primary antibodies, rinsed, and incubated with a HRP-conjugated secondary antibody

for 30 minutes followed by a DAB substrate. Lastly, sections were counterstained with hematoxylin and coverslipped.

2.3.13. Statistics

All data analysis was performed in GraphPad Prism 5 software. Brain distribution data were evaluated by a 2-way ANOVA followed by Bonferroni post-test. Tumor growth curves were evaluated by fitting the growth data with a first-order exponential and comparing tumor doubling times using an ANOVA followed by Tukey's multiple comparison test. Survival differences were evaluated from the Kaplan-Meier plot with the Mantel-Cox test. Differences were considered statistically significant for an alpha level of 0.05.

2.4. Results

2.4.1. Nanoparticle Characterization

SEM analysis confirmed that nanoparticles possessed a spherical shape with smooth surface morphology (Figure 2.1A, Figure 2.5). Nanoparticles sizes were relatively monodisperse (Figure 2.1A,C) with a mean particle diameter of 123 ± 31 and 119 ± 37 nm for CPT and DiR nanoparticles, respectively, as measured by SEM. DLS measurements yielded hydrodynamic diameters of 206 ± 32 and 204 ± 41 nm respectively and zeta potentials of -21.1 and -23.7 mV for CPT and DiR loaded nanoparticles, respectively (Figure 2.1C). Hydrophobic agents were effectively encapsulated in the NPs with drug loading efficiency of 9.6% for CPT and 0.5% for DiR. The CPT release profile of the particles was determined in vitro in PBS at 37°C (Figure 2.1B). Drug was initially released from nanoparticles in a burst of ~80% over 6 hours, and complete CPT release was observed within 24 hours.

2.4.2. Tumor Localization

NPs loaded with DiR, a hydrophobic, near infrared dye shown to release less than 5% in 24 hours and commonly used to track NPs [140,141], were administered IV to evaluate the ability of NPs to deliver hydrophobic payload to an intracranial GL261-Luc2 tumors. Biopsy punches were taken from the tumor core, peri-tumor region below the tumor, and contralateral (healthy) hemisphere (Figure 2.2A). Nanoparticle payload accumulated in the tumor core at significantly higher concentrations compared to both healthy and peri-tumor brain regions ($p < 0.05$) at day 12, 16 and 20 (Figure 2.2B). Payload delivery was positively correlated to tumor size for both tumor core and peri-tumor regions ($p = 0.0002$ and 0.048, respectively) (Figure 2.2C).

2.4.3. Tumor Treatment Efficacy

The tolerability and efficacy of CPT delivered in nanoparticle-encapsulated versus free form were evaluated in C57BL/6 albino mice bearing intracranial GL261-luc2 tumors. Subjects received weekly injections of saline, free CPT, NP-10, or NP-20 for 3 cycles. Subjects that received nanoparticle encapsulated CPT at both low and high dose experienced similar weight loss following treatment when compared to free CPT (Figure 2.3A, shown with error bars in Figure 2.6). Tumor growth in saline-treated subjects was exponential, and no significant differences in tumor size were observed for mice treated with free CPT or NP-10 (Figure 2.3B). However, tumor growth was significantly slowed by treatment with NP-20. Additionally, NP-20 provided a significant survival benefit over the other treatment groups with a median survival of 36.5 days compared to 28, 32 and 33.5 days for saline, free CPT and NP-10 respectively (Figure 2.3C). In a separate series of experiments, we established that blank nanoparticles did not alter survival when compared to saline treated controls (Figure 2.7).

2.4.4. Camptothecin Activity

CPT bioactivity was examined by γH2A.X staining in intracranial tumors of animals treated with saline, free CPT, and nanoparticle encapsulated CPT (Figure 2.4). Tumor sections taken from NP-20 treated mice showed an increase in staining intensity of γH2A.X compared to free CPT, with an average score of 3.0 as compared to 2.0, respectively (blinded scoring performed by board certified pathologist). These data support the hypothesis that encapsulation of CPT in nanoparticles allows for the delivery of greater amounts of CPT without adverse effects (Figure 2.4). To rule out the possibility that higher delivery of nanoparticle encapsulated CPT was due to higher vascularity of those particular subjects, we also examined CD31 staining intensity across different treatment groups [142]. Each treatment group showed similar CD31 staining intensity.

2.5. Discussion

This study presents the use of CPT-loaded PLGA NPs for the systemic treatment of an orthotopic murine glioma. We achieved a loading of CPT in our nanoparticles of ~10% by weight; this value is higher than our theoretical loading of 8%, indicating that more PLGA was lost than CPT during the nanoparticle fabrication process. Loss of PLGA during nanoparticle fabrication has been reported previously[133], and our loading is consistent with the 5-25% loading reported by other groups encapsulating CPT in PLGA [137,143]. The average hydrated nanoparticle diameter measured by DLS (~200 nm) was larger than the diameter measured by SEM (~120 nm), which is expected, given that NPs will become hydrated in the aqueous environment required for DLS and that a fraction of nanoparticles will experience aggregation after resuspension. The zeta potential of our nanoparticles was approximately -21 mV, which is more negative than the purposed optimal range of -10 to +10 mV required to minimize nonspecific nanoparticle interactions and MPS cell clearance [51]. NPs displayed CPT release kinetics typically

observed for PLGA nanoparticles, with an initial, rapid burst release followed by a period of slowed release and the majority of drug being released within several days. Drug was therefore effectively encapsulated for subsequent release in physiological environments.

One advantage of using PLGA nanoparticles as drug delivery vehicles is that encapsulation of hydrophobic agents can improve their solubility and reduce toxicity. Toxicity remains a problem for CPT, which has a literature reported maximum tolerated dose (MTD) of 8-10 mg/Kg [62]. In our hands, injection of free CPT at a dose of 16 mg/Kg caused almost instant death (5-10 seconds), presumably due to its poor solubility. However, CPT was well-tolerated when encapsulated in PLGA NPs; no signs of acute drug toxicity were observed for doses of up to 30 mg/kg. We observed an MTD for PLGA-CPT NPs of 20 mg/Kg CPT, with higher doses resulting in weight loss after treatment (data not shown). This increase in CPT tolerability could be due to a combination of increased solubility and reduction of peak dose due to prolonged release of CPT from the particles. The extended release profile seen could also increase tolerability by allowing particles to deliver CPT to the tumor or be cleared before a majority of the CPT is released, thereby reducing CPT exposure to healthy cells.

The difficulty of delivering drugs across the BBB makes the use of an intracranial tumor model critical for evaluating nanoparticle drug delivery; however, the most common GBM models (i.e. U87, U118, 9L) grow as bulky tumors, with well-defined borders and a highly disrupted BBB [134,135]. The GL261 tumor model was chosen for this work for several reasons. First, human GBM is characterized by diffuse and highly infiltrative growth, and it has been shown that GL261 tumors better recapitulate these characteristics with tumor cells invading into surrounding brain parenchyma where the BBB is still intact [144,145]. Additionally, GL261 cells share key genomic features with human GBM, including activated K-ras (mutant) and mutant p53, along with increased

activation of the PI3K/Akt pathway [134,146]. Here we utilized a Luc2 transfected GL261 model, which has been shown to have the same growth characteristics *in vivo* as the parent cell line, while enabling noninvasive tracking of tumor growth over time[138,147]. In future work, this model could be used to evaluate the delivery of molecularly targeted drugs that would not otherwise cross the BBB.

It is well-established that nanoparticles can extravasate from peripheral circulation through leaky tumor vasculature into tumor core, a phenomenon termed the enhanced permeation and retention (EPR) effect; however, the optimal nanoparticle size for achieving the greatest EPR effect will depend on a number of factors including tumor type, location, and size of tumor. EPR data has been reported for nanoparticles ranging from 20-1000 nm in various tumor models [148–151]. Previously 10 nm DSPE-PEG micelles have been shown to passively accumulate in intracranial GL261 tumors; however, to our knowledge, the nanoparticle size requirement for EPR-mediated delivery to intracranial GL261 tumors has not been evaluated. Thus, we were interested to study how nanoparticle payload was delivered selectively to tumor core versus periphery during tumor progression. Biopsy punches taken from the brains of tumor bearing mice administered PLGA-DiR NPs demonstrated that NPs preferentially accumulate in the tumor core, and this preferential delivery increased as a function of tumor size and with time post-tumor induction. These data suggest that effective delivery of hydrophobic payloads can be achieved even in late stages of growth in this intracranial model.

The growth of intracranial GL261-Luc2 tumors was unaffected by treatment with free drug or with encapsulated drug at the MTD for free drug of 10mg/kg. However, CPT-loaded PLGA nanoparticles delivered systemically at a dose of 20 mg/Kg CPT slowed tumor growth and produced a significant increase in survival compared to all other treatments. CPT is a potent DNA damaging therapy and acts on cells by inhibiting

enzyme DNA topoisomerase I, which leads to generation of DNA double strand breaks (DSB), leading to apoptosis. DSB activates the DNA damage response (DDR) and produces accumulation of phosphorylated histone H2A.X (γH2A.X), a hallmark of DDR [152]. IHC analysis of γH2A.X validates that the slowed tumor growth and significant increase in survival of animals treated with NP-20 was due to the enhanced tolerability of nanoparticle encapsulated CPT, which enabled a higher total dose to be delivered.

PLGA is both biocompatible and biodegradable, and has been used extensively for improving the action of chemotherapeutics [130–132], including in humans. For example, PLA-PEG nanoparticles encapsulating the chemotherapeutic drug doxorubicin are the subject of a phase II clinical trial in prostate cancer and non-small cell lung carcinoma [27]. Other groups have encapsulated CPT within PLGA nanoparticles, and these formulations were effective when delivered directly to intracranial tumors, either by convection enhance delivery or from inside a hydrogel implant [19,133]. The data presented here confirm that encapsulation of CPT can improve its activity. To our knowledge, this study is the first to report effective therapy of an intracranial tumor by systemic administration of CPT-loaded PLGA nanoparticles. Surface modification of nanoparticles – for example, attachment of poly (ethylene glycol) to improve circulation time, or ligands designed to facilitate transport of nanoparticles across the BBB could further improve payload delivery to the CNS [153]. Enhancing delivery across an intact BBB to provide pan-CNS delivery of chemotherapies will improve drug access to invading cancer cells to improve tumor therapy.

2.6. Tables and Figures

A

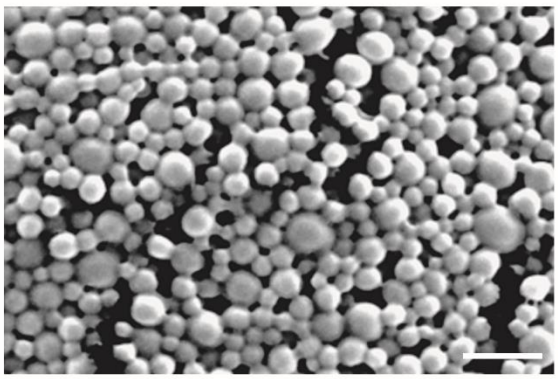

B

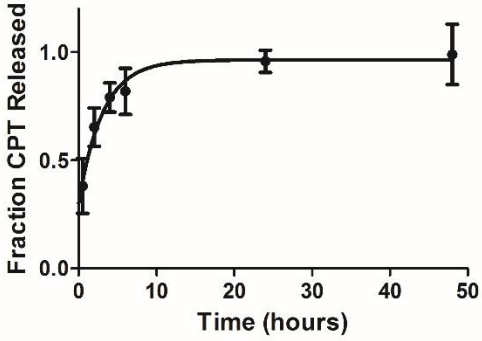

C

Nanoparticles	SEM Diameter (nm)	DLS Diameter (nm)	Zeta Potential (mV)	Loading (%)
PLGA-CPT	123 ± 31	206 ± 32	-21.1	9.6
PLGA-DiR	119 ± 37	204 ± 41	-23.7	0.5

Figure 2.1: Nanoparticle characterization. (A) Representative SEM image of CPT-loaded PLGA nanoparticles. (B) CPT was released from nanoparticles into buffer, with ~80% of total drug released after 6 hours. Points and error bars represent the mean ± SD, with 3 samples measured for each time point. (C) CPT- and DiR-loaded nanoparticles had similar diameters, as measured by SEM and DLS, and similar surface charges. (Scale bar = 500 μm)

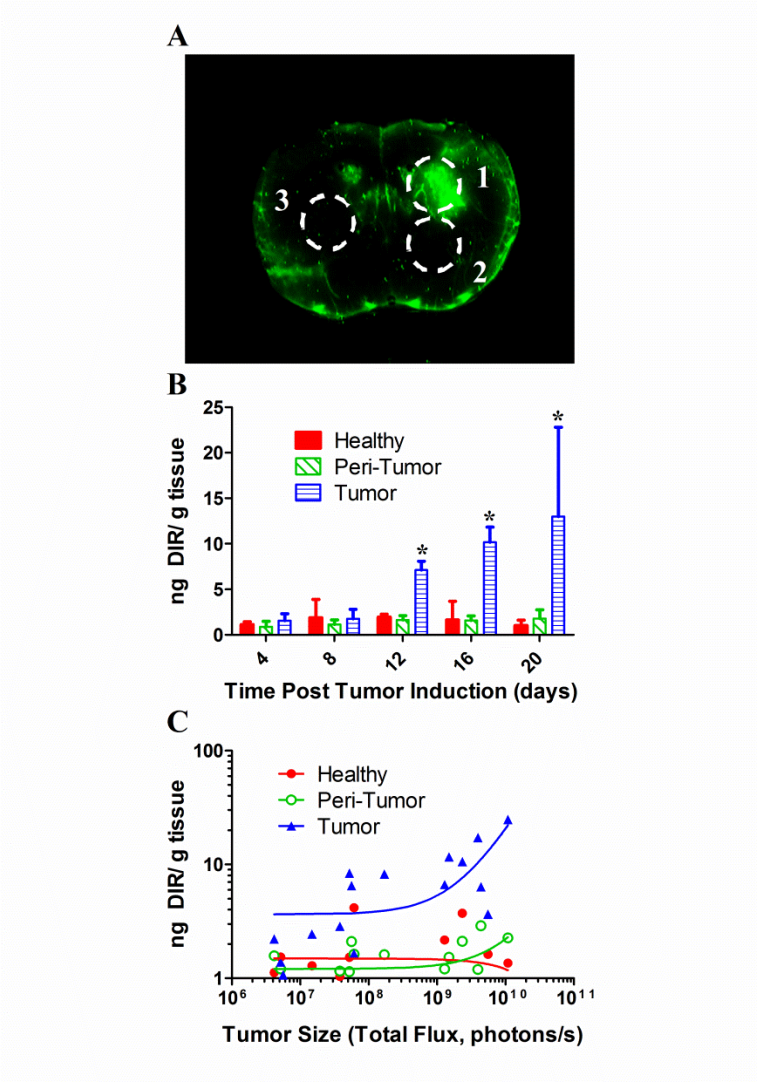

Figure 2.2: NP payload delivery to orthotopic GL261 tumors.(A) DiR distribution (green) in a tumor bearing mouse brain captured on the LI-COR Oddyssey. Regions marked indicate example tissue punch locations used for tumor (1), peri-tumor (2) and healthy brain (3). (B) DiR accumulation was significantly higher in the tumor compared to peri-tumor or healthy brain regions, 12, 16 and 20 days post tumor implantation ($p=0.01$) Bars indicate mean ±SD (n=5 mice/day). (C) The amount of DiR/ g tissue, quantified by fluorescence for each region, positively correlated with tumor size for both tumor core and peri-tumor regions ($p=0.002$ and 0.048 respectively).

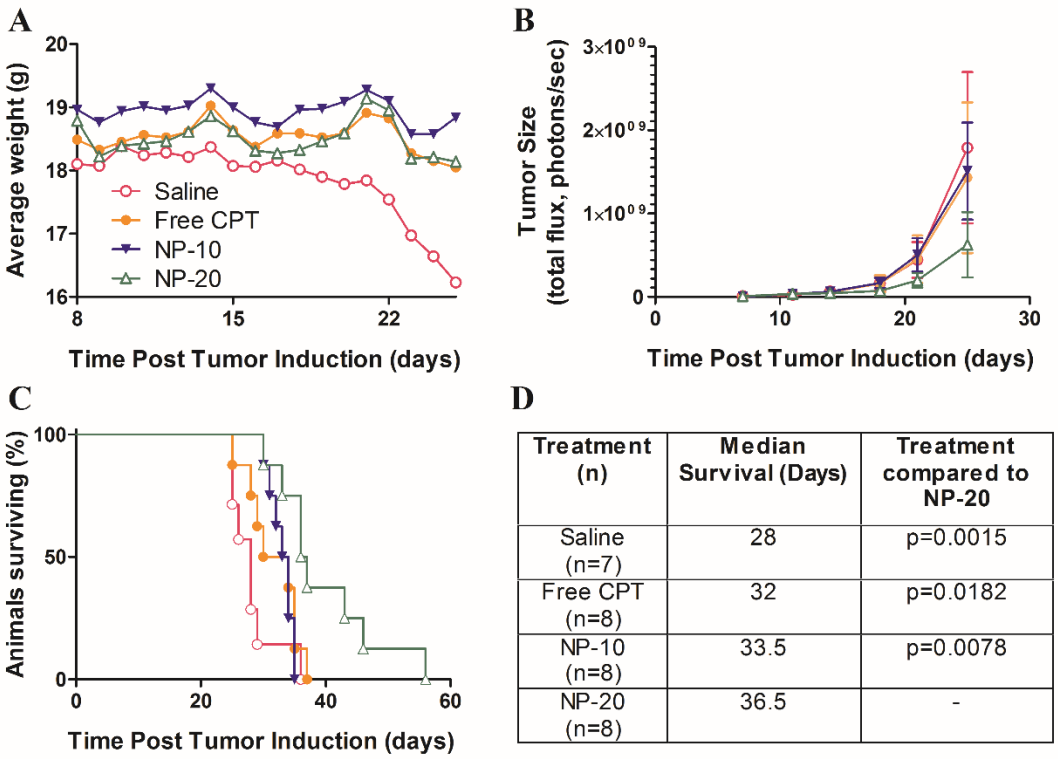

Treatment (n)	Median Survival (Days)	Treatment compared to NP-20
Saline (n=7)	28	p=0.0015
Free CPT (n=8)	32	p=0.0182
NP-10 (n=8)	33.5	p=0.0078
NP-20 (n=8)	36.5	-

Figure 2.3: Treatment efficacy studies. (A) Mice receiving CPT either freely or in a NP showed similar weight fluctuations over the course of treatments. Saline treated mice weight remained steady until the tumor burden became too great. (B) Tumor burden monitored by IVIS showed NP-20 significantly slowed tumor growth (p=0.01) and provided a significant survival benefit (C & D) compared to all other treatments. Error bars indicate ± SD.

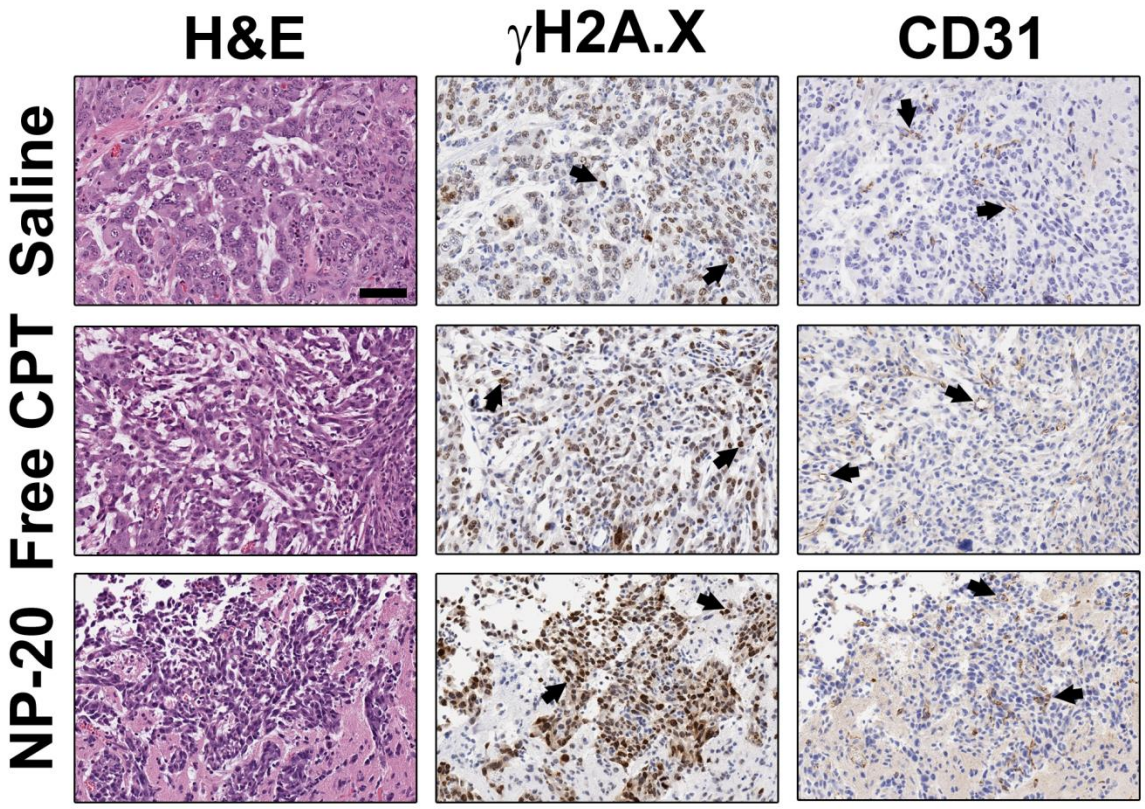

Figure 2.4: Camptothecin bioactivity. Left panel shows H & E staining of the tumor cells in saline, free CPT and nanoparticle encapsulated CPT (20 mg/Kg) treated animals. Center panel shows γH2A.X staining on the serial section, and demonstrates very high γH2A.X staining for animals treated with nanoparticle encapsulated CPT (20 mg/Kg) (IHC Score =3) as compared to saline (IHC score = 1-2) and free CPT (IHC score = 2) treated animals. Right panel shows the CD31 staining on the serial section, and demonstrates similar staining intensity in all the treatment group. Positive staining in each section is indicated by black arrow. All the images are taken at 20X magnification (scale bar in top left panel = 100 μm). (n=3 mice/treatment)

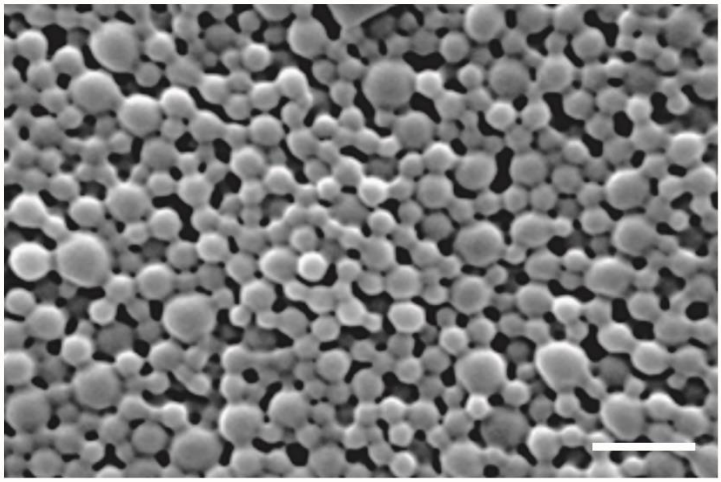

Figure 2.5: Representative SEM image of DiR-loaded PLGA nanoparticles. (Scale bar = 500 μm)

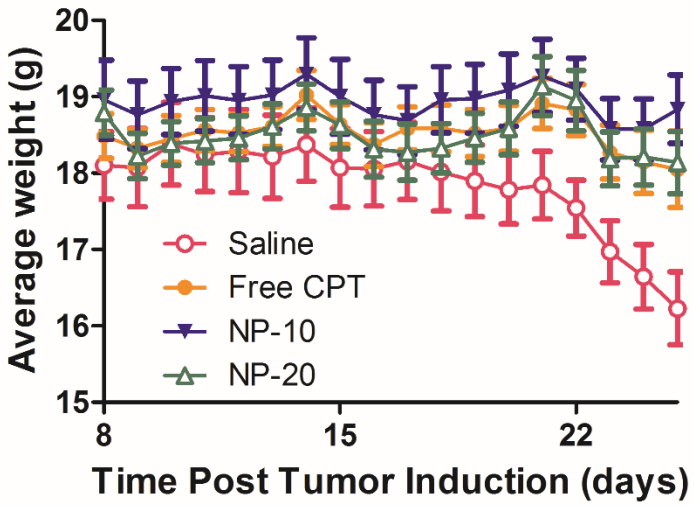

Figure 2.6: Treatment tolerability. Mice receiving CPT either freely or in a NP showed similar weight fluctuations over the course of treatments. Saline treated mice weight remained steady until the tumor burden became too great. Error bars indicate ± SD. (n=7-8 mice/treatment)

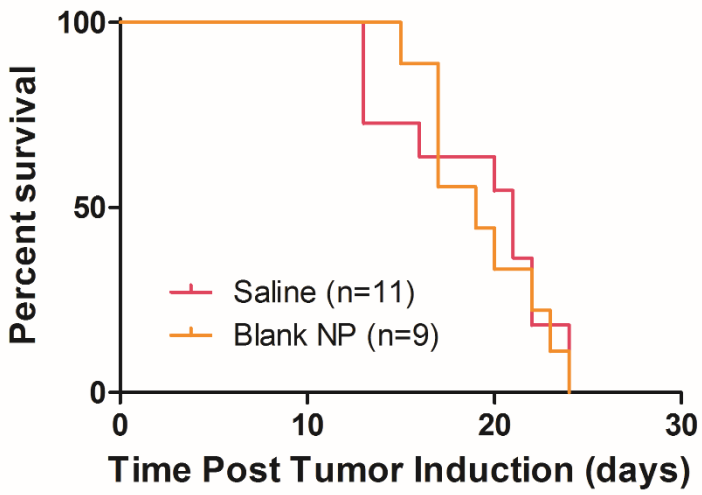

Figure 2.7: Effects of blank NPs on GL2621 tumor growth. Kaplan-Meier survival curves for the treatment of intracranial GL261-Luc2 tumors. Either saline or blank NPs (no drug) were delivered intravenously on days 7, 14 and 21. No significant survival differences were observed with a median survival of 21 days versus 19 days for saline and blank NPs respectively (Mantel-Cox test, p= 0.8229).

CHAPTER 3

Evaluating the Transport and Fate of Nanoparticles within the Cerebrospinal Fluid after Intrathecal Administration

3.1. Abstract

Effective treatment of neurological diseases remains a significant challenge to our society, due largely to the inability of systemic therapeutics to reach the central nervous system. The circulation of cerebrospinal fluid (CSF) around the entire brain and spinal cord makes it an attractive delivery medium to avoid systemic barriers; however, most therapies administered intrathecally have failed due to inadequate distribution and rapid clearance. Despite extensive use of nanoparticle (NP) drug carriers to prolong circulation and alter distribution of systemic therapies, the potential use of NPs for intrathecal (IT) administration remains poorly characterized. Here, we tracked the distribution and retention of 100 nm NPs after IT administration to evaluate their potential as a drug delivery system for IT therapies. We found NPs were well tolerated and rapidly distributed along the entire neuraxis within 2 hours by the convective forces of the CSF after IT administration. A significant population of NPs was retained within the CSF space for over 3 weeks, with a majority of clearance occurring through the cribriform plate. Comparison of NP localization around the brain and spinal cord showed distinctive distribution patterns due their unique anatomies and geometries. Taken in sum, these studies demonstrate the ability of 100 nm NP to achieve wide spread delivery along the neuraxis and highlight their potential for IT drug delivery applications.

3.2. Introduction

Achieving effective drug delivery to the central nervous system (CNS) remains one of the greatest challenges in treating CNS diseases. Systemically administered therapies are largely ineffective due to the presence of the blood-brain and blood spinal

cord barriers, which exclude an estimated 98% of small molecules and all large molecules[154]. Active agents capable of crossing these barriers still typically require large doses to achieve adequate CNS concentrations, often resulting in severe off-target effects in peripheral organs and tissues.

To circumvent these systemic barriers, administration of active agents directly into the cerebrospinal fluid (CSF) surrounding the brain and spinal cord has gained renewed attention as a potential delivery route. Intrathecal (IT) administration is especially appealing due to its ability to achieve high concentrations of drug in the CSF at a fraction of the dose necessary by systemic routes[108,109]. However, its translation into patients has presented several challenges, and most therapies have failed clinically due to poor pharmacokinetics and toxicity [90,155–159]. While hydrophilic compounds are typically capable of distributing through the CSF, they tend to suffer from rapid clearance with the continuous turnover of CSF and require frequent dosing[91,118,121,124,160]. The high propensity of hydrophobic/lipophilic compounds to enter cells and bind to extracellular matrix proteins restricts their distribution close to the site of injection, which limits the ability of locally administered agents to treat diseases affecting non-focal regions of the CNS[123–125,161].

Encapsulation of therapeutics within polymeric or liposomal nanoparticles (NPs) has been utilized extensively to overcome similar pharmacokinetic limitations of systemically administered agents[1,14,15,132,162,163], yet NP-based drug delivery approaches have received minimal attention for improving intrathecal therapies. The versatility of NP properties allows for a wide range of compounds to be effectively encapsulated and then released over prolonged periods of time[162]. Thus, if NPs could be designed to effectively move through CSF filled compartments in the CNS, it would be possible to further develop them to deliver drugs across CSF-exposed tissues. Here, we evaluated

the ability of NPs to distribute throughout the CNS via the CSF after intracisternal administration in healthy mice. To understand the broad kinetics of NP movement along the neuraxis, we tracked the distribution FluoSpheres (fluorescent polystyrene beads) *in vivo* using an IVIS imaging system. We also used confocal microscopy on *ex vivo* tissue slices to examine NP fate with respect to tissue structures to identify potential barriers and opportunities for NP drug delivery by IT administration. These studies are expected to have broad implications on the use and design of NPs for CSF delivery across CNS diseases.

3.3. Materials and Methods

3.3.1. Materials

100 nm carboxylate-modified FluoSpheresTM (red fluorescent, Ex/Em 580/605nm), 10 μm FluoSpheres (green fluorescent, Ex/Em 468/508nm) and 20x Borate Buffer were purchased from ThermoFisher Scientific (Waltham, MA USA). All water was endotoxin-free (<0.0050 EU/ml), obtained from G-Biosciences (St. Louis, MO, USA). Poly(ethylene glycol)-amine (mPEG-Amine, 2 kDa MW) was purchased from Creative PEGWorks (Chapel Hill, NC USA). All other chemicals or reagents were purchased from Sigma-Aldrich (St. Louis, MO USA) unless specified.

3.3.2. FluoSphere PEGylation and Characterization

Carboxylate-modified FluoSphereTM (FS, 100 nm) NPs were covalently modified with mPEG-Amine (2k Da MW) by carboiimide chemistry as previously described by Nance et al.[38]. FS in 500 μl aliquots were washed to remove sodium azide using 0.5 ml Amicon-Ultra centrifugation filters (10k MWCO). Retained FS were resuspended with water bath sonication in 2 ml endotoxin-free water. mPEG-amine (5x molar excess) was added to the FS and allowed to stir for 15 min. Next, 6.5 mg N-Hydroxysuccinimide (NHS) dissolved in 6 ml borate buffer (200 mM, pH8) was added to the stirring FS

solution, followed by 15.4 mg 1-Ethyl-3-(3-dimethylaminopropyl) carbodiimide (EDC). The reaction was left stirring for 3 hrs at room temperature before quenching with excess glycine (100 mM) for 30 min. Unreacted PEG, EDC, NHS and glycine were removed by dialysis (100k MWCO) against 4 L DI water for 24 hours. FS were collected, further washed by centrifugation using 15ml Amicon-Ultra centrifugation filters (100k MWCO), and resuspended to 20 mg/ml in 1x PBS for storage at 4°C until use.

3.3.3. Size and Zeta Potential

FS size and zeta potential was measured in 1 mM KCl before and after PEGylation using the NanoBrook 90Plus Zeta (Brookhaven Instruments, Holtsville, NY USA). Each sample was measured 10 times and averaged across 3 technical repeats.

3.3.4. In Vivo Studies

All procedures and animal care practices were performed in accordance with the Barrow Neurological Institute's Institutional Animal Care and Use Committee. Healthy C57 albino mice (Charles River) were used for the following *in vivo* experiments.

3.3.5. FluoSphere Administration

FS were administered directly into the CSF through the cisterna magna. Mice were anesthetized with ketamine/xylazine (100/10 mg/kg) and mounted in a stereotaxic frame (Kopf Instruments, Tujunga, CA, USA) on top of an infrared heating pad. The head was shaved and sterilized with three alternating passes of betadine and ethanol. A 1 cm incision was made over the cerebellum and neck before removing the bite bar and dropping the head to a 60° angle with the body. The muscle over the neck was carefully retracted to expose the dura covering the cisterna magna. A Hamilton syringe (29 gauge needle, 30° beveled tip) containing 2 µl FS was inserted through the membrane to a depth of 1.5 mm. The syringe was then retracted to 1 mm and allowed to equilibrate for 1 min. The FS were injected over 1 min, and the needle was left in place for an additional 2

min before removing. The incision was closed with staples and treated with a topical antibiotic. All animals received a subcutaneous (SQ) injection of Buprenorphine SR (1 mg/kg) prior to surgery, and ibuprofen was provided in their water for 1 week to control pain.

3.3.6. In Vivo FluoSphere Tracking

Macroscopic FS fluorescent distribution and clearance kinetics were first examined using a Xenogen IVIS Spectrum In Vivo Imaging System. Prior to FS injection, clippers and Nair were used to remove the fur along head and back. A pre-injection image was captured to control for background autofluorescence. FS were administered as described above (3.3.5), except tissue glue was used instead of staples to reduce signal attenuation. At 5 min, 2, 6, 24 and 48 hours after injection, the mice were imaged in the IVIS (Filters: Ex 570/Em 620) under 2% isoflurane. Using the Living Image Software, a line profile was drawn along the length of the neuraxis to quantify FS intensity at each pixel. Background signal measured from the pre-injection image was subtracted within subject from each time point. FS intensity was normalized within each subject to the max intensity at 5 min.

3.3.7. Ex Vivo Neuraxis Collection

Mice were sacrificed at 2, 6, 24, 48 hrs, 1 and 3 wks post FS administration, to examine 100 nm FS fate at the cellular level. Mice were perfused through the heart with 15 ml heparinized PBS (1000U/ml) followed by 10 ml 4% paraformaldehyde (PFA). To preserve the integrity of the leptomeninges, the entire neuraxis, from nasal sinuses to sacral spinal region, was isolated with the aid of dissection scissors, removing the majority of muscle and skin but leaving the bone intact. The neuraxis was post-fixed in 4% PFA for an additional 48 hrs. The bone was decalcified in a 4% HCl and 4% Formic Acid v/v solution, replaced daily, for 5 days. This procedure enabled cryosectioning of

the neuraxis without removing the bone. After cryoprotection in a 30% (w/v) sucrose solution for 48 hrs, the brain and spinal cord were cut at the C1 vertebrae to enable separate processing. We validated that decalcification does not produce substantial loss or redistribution of fluorescence signal by IVIS imaging two complete neuroaxis before and after decalcification. Although the fluorescence signal was observed to increase slightly after decalcification, presumably because the reduction of signal attenuation by bone, the relative signal distribution along the neuraxis remained consistent.

3.3.8. Brain and Spinal Column Processing

The spinal column was dissected into a total of eight 5 mm sections starting at C1. These 8 sections were placed caudal side down in a disposable cryomold, embedded in Tissue-Tek OCT and frozen at -80° C. 20 μm slices were cut on a Leica cryostat, resulting in 8 coronal spinal sections of known distances along the spinal column. For the brain, a single hemisphere from each sample was embedded in OCT and frozen at -80° C before slicing into 20 μm sections. The slides were washed 3x with 1x PBS to remove the OCT, counterstained with Vectashield plus DAPI mounting medium, and cover slipped. A Zeiss LSM confocal microscope was used for all imaging. Brain sections and spinal sections were imaged for FS (Ex 560/ Em 605 nm) using a 10x objective, and T-PMT was used to provide a contrast image of the anatomy. Laser intensities and gain were maintained across samples and time points. For quantification of the spinal cord distribution, an average background pixel intensity (based on non-injected controls) was subtracted from each image and the FS intensity was measured by ImageJ (v1.47, NIH).

3.3.9. Statistical Testing

All statistical tests were performed using the GraphPad Prism 5 software. Comparisons of AUC over time were made with a 1-way ANOVA with Bonferroni Multiple Comparisons test. Statistical significance is reported for $p < 0.05$.

3.4. Results

3.4.1. FluoSphere PEGylation

Successful PEGylation of FS via EDC chemistry was confirmed by DLS, via observation of the expected increase in average diameter and shift in zeta potential towards a more neutral charge. After PEGylation, the 100 nm FS diameter increased to 122 ± 8.17 nm and the zeta potential shifted from -45 ± 5.4 to -14 ± 2.2 mV.

3.4.2. In Vivo FluoSphere Tracking

FS distribution along the neuraxis was monitored in intact mice over the course of 2 days using an IVIS Spectrum imaging system. FS were administered directly into the CSF through the cisterna magna, and the mice were imaged 5 min, 2, 6, 24 and 48 hours post-injection. It is important to note that due to the limitations of fluorescence penetration, IVIS could only reliably detect the FS along a short segment of the spinal column, in the middle of the back, where the signal was not obstructed by the musculature of the shoulders and hind legs. Beginning at the first time point measured (5 min post injection), the FS signal was focused at the injection site with no detectable signal along the spinal cord (Figure 3.1A). By 2 hrs, the FS signal spread over the entire brain region and was detected along the spinal cord, although the strongest signal remained focused at the injection site. From 2 to 48 hours post-injection, FS signal around the brain continued to move away from the injection site towards the olfactory bulb. The brain AUC significantly decreased from 6.6 at 2 hrs to 2.7 AU*hrs by 48 hrs ($p=.0098$, Figure 1C) with the greatest clearance observed from 2 to 6 hrs (6.6 to 4.8). Although there was a modest decrease in FS AUC along the spinal cord from 2 to 6 hrs (1.9 to 0.86), the signal AUC increased back to 1.2 by 48 hours. Overall, there were no significant changes to the total FS delivery along the spinal cord.

3.4.3. Ex Vivo Spinal Column Distribution

Transverse cryosections, taken from known distances along the spinal column, were imaged by confocal microscopy to visualize FS distribution around and along the spinal cord. Although it is difficult to visualize the boundary between the pia matter and the parenchyma, our initial observations did not suggest any significant FS penetration into the spinal parenchyma from the CSF. In a subset of animals, we removed the bone and meninges prior to imaging. Removal of the meninges resulted in a loss of nearly all detectable FS signal, providing some evidence that the FS are almost completely retained within or at least very strongly associated with the meninges. 100 nm FS were observed along the entire length of the spinal cord within 2 hours and encompassed the entire circumference of the spinal cord, including within the meninges of exiting nerve roots (Figure 3.2 and 3.3). There was a slight tendency at all time points to observe a greater concentration of FS along the ventral spinal cord surface. Interestingly, we consistently observed a small population of FS within the central canal at each time point, specifically in cervical and thoracic spinal sections. At 3 weeks after injection, the FS were still readily detected along the entire length of the spinal column; although they appeared as more punctate foci compared to earlier time points. To test if the rapid distribution of the FS to the sacral spinal cord was size dependent, we examined the ability of 10 μm non-PEGylated FluoSpheres (MFS) to transverse the leptomeningeal space. Surprisingly, the MFS could be found in the sacral region within 2 hours, albeit very infrequently (3 total in 54 slices observed). We also did not find more than 2 MPS per tissue slice past 10 mm down the spinal column.

Quantification of FS intensity by ImageJ revealed a gradual exponential decay in fluorescent signal moving caudal from the injection site towards the sacral spinal section (Figure 3.4). Overall, the tissue slice quantification agreed with the trends seen in the

IVIS tracking. For the first 48 hours and even out to 1 week, the total FS delivery (AUC) to the spinal column did not significantly change (Figure 3.3H). We did observe a similar decrease in AUC from 2 to 6 hours (3.4E9 to 2.4E9), followed by a slight increase in delivery from 24 to 48 hours (2.7E9 to 3.0E9). Interestingly, the FS concentration along the spinal cord continued to trend upwards from 48 hours to 1 week (3.0E9 to 3.8E9) and was significantly higher at 3 weeks post-injection (5.1E9) compared to 6, 24 and 48 hours ($p<0.05$).

3.4.4. Ex Vivo Brain Distribution

To visualize the anterior/posterior distribution of FS around the complex geometries of the brain, the brain was sliced in sagittal sections (Figure 3.6). Consistent with our observations along the spinal cord, we found minimal evidence of FS penetration across the pia mater into the brain parenchyma. In general, FS distributed throughout the entire meningeal network on the surface of the brain. FS were observed to follow the meninges into the sulci of the cerebellum and along the trigeminal nerve. FS delivery was consistently concentrated along the ventral side of the brain compared to the dorsal side, and FS signal was especially sparse along the dorsal prefrontal cortex region at all time points. To test whether the ventral preference was an artifact of the mouse lying in the prone position after injection, we injected 3 additional mice but kept them on their back for 2 hours post-injection prior to perfusion. Interestingly, recovery position did not produce any obvious qualitative changes to the FS distribution, and delivery to the prefrontal cortex region remained sparse (Figure 3.6). In all mice, we observed the greatest concentrations of FS within concave structures around the brain, specifically the supracerebellar cistern between the cortex and cerebellum on the dorsal side of the brain and the pituitary recess anterior of the pons on the ventral side of the brain

3.4.5. Peripheral Clearance

We found evidence of FS clearance across the cribriform plate into the nasal sinuses (Figure 3.5) at all time points. To test whether cisternally administered FS were cleared into peripheral compartments, we examined the liver and spleen with confocal microscopy. There was no observable FS signal above background in the liver at any of the time points (data not shown). FS were detectable within the spleen at all time points, although the greatest concentration of FS was seen at 2 hours after injection (Figure 3.7). Anatomically, FS appeared to be consolidated around the white pulps of the spleen.

3.5. Discussion

The presence of CSF around the entire brain and spinal cord and through the parenchymal interstitial spaces makes it an attractive delivery medium for neurological therapies. CSF is produced by the choroid plexus, after which it moves through the ventricles into the cisterna magna, where it distributes down the spinal cord and around the brain through the leptomeningeal space [93,164]. Although the overall magnitude of a bulk or net directional flow of CSF is debated, it is generally accepted that CSF moves in a pulsatile fashion due to the rhythmic forces generated by the cardiac and respiratory cycles [96–98,110]. The ebb and flow of CSF along the neuraxis is predicted to further interact with the complex network of trabeculae and exiting nerve roots within the SAS to generate local vortexes of CSF mixing. Between the convective forces of CSF flow and the local areas of CSF mixing, it would be expected that drugs administered into the CSF would rapidly disperse along the neuraxis. However, most therapies of interest for neurological disease are believed to be unable to distribute through the CSF, and the use of intrathecal administration in the clinic has been mainly limited to analgesics. SPECT studies by Wolf et al suggest the limited distribution is due to the biophysical properties of the drugs, with the propensity of the therapy to bind cellular and ECM components

dictating the ability of the molecule to move away from the injection site [124].While this is advantageous for the translation of highly lipophilic analgesics for intrathecal therapy, where local delivery is a necessity to avoid possible detrimental respiratory side effects, many therapies for CNS diseases are also lipophilic but require therapeutic delivery throughout the neuraxis. The objective of our studies was to evaluate whether the biophysical properties of 100 nm PEGylated nanoparticles allow them to distribute through the CSF to achieve uniform delivery along the entire neuraxis after intracisternal administration.

Nanoparticles have been administered intrathecally previously, but most studies did not track nanoparticle distribution following administration[123,165–167] or only showed efficacy in providing local sustained delivery for the treatment of spinal cord injury[84–86]. Our studies show 100 nm FS administered through the cisterna magna were well tolerated and distribute through the meninges along the entire neuraxis, including into the sulci of the brain and along nerve bundles (trigeminal, optic and exiting spinal nerve roots). Distribution of the 100 nm FS to the sacral portion of the spinal column within 2 hours post administration is too rapid for Fickian diffusion alone, supporting the hypothesis nanoparticles are carried convectively by CSF flow. Movement of the FS in all directions from the cisterna magna is supportive of CSF mixing driving solute movement, rather than strictly directional laminar CSF flow[96,97,110,113].

CSF mixing has been proposed to be especially important along the spinal cord, where multiple studies predict the overall CSF movement to be nearly completely ossillatory[98,168,169]. The magnitude of these oscillations is expected to decrease caudally along the spinal column. We observed here that while FS were able to access even distal regions of the spinal cord, a gradient exists in the rostral-caudal direction. This gradient could represent an equilibrium established by the decreasing oscillatory forces produced.

The more punctate clustering of the FS signal at 3 week does suggest a possible contribution from some FS becoming trapped by the microanatomy of the SAS as they move down the spinal column. Based on prior works by Wolf et al. and Papisov et al., the observed moderate exponential FS gradient along the spinal column is consistent with the distribution of hydrophilic, low-binding small molecules injected intracisternally or intraventricularly[124,160]. Whereas, if the FS were experiencing significant tissue binding, as would be typically observed for hydrophobic/lipophilic small molecules, we would expect to see a significantly faster decay in signal[124,160]. When the same hydrophilic molecules were administered by lumbar injection, especially with the addition of a saline flush, distribution along the spinal cord increased and was more uniform while minimally reducing FS delivery to the brain SAS. Due to the compliance of the cisterna magna membrane and lack thereof along the spinal column, the cisterna magna is thought to accept the excess volume administered at the lumbar region, driving solute movement towards the cranial SAS. Thus, we expect a similar approach could be applied to the nanoparticle injection to further improve the uniformity of delivery across the neuraxis.

Distribution of FS around the brain was considerably more heterogeneous than the spinal cord. While no obvious preference for either hemisphere was observed, both sagittal and coronal brain sections showed a strong preference for FS movement along the ventral side of the brain. This asymmetrical distribution does not appear to be dependent on solute molecular weight: we observed this for 100nm FS, as it was similarly observed for both a small molecule (99mTc-DMSA, ~500 Da) and a protein (idursulfase, 76 kDa) following lumbar injection[124,160]. We also confirmed the ventral distribution was not an artifact of animal position following injection, suggesting there might be inherent differences in net CSF movement/clearance around the dorsal and

ventral brain. To our knowledge, this has not been directly measured. FS are clearly capable of redistributing in all directions following their injection into the cisterna magna. A relatively high FS concentration is observed in the supracerebellar cistern at all time points, whereas a relatively small population of FS appear to move past the cistern towards the olfactory bulb, with a fewer but significant number of FS observed in the olfactory bulb. We saw a similarly pronounced concentration of FS within the pituitary recess on the ventral brain, except significantly more FS moved rostrally beyond the recess. We expect the increased deposition of FS within concave structures around the brain is a result of strong areas of local CSF mixing, similar to the phenomenon of platelet deposition within an aneurysm[170,171]. The different orientations and potential differences in trabeculae densities between the supracerebellar cistern and the pituitary recess may also contribute to the stark differences in the movement of FS past these regions. Taken in sum, our data demonstrate that 100nm FS are capable of distributing throughout the entire leptomeninges of the brain. However, there were significant differences, consistent across time points, observed in FS distribution to specific regions around the brain. We cannot say whether the distinct patterns of delivery observed for 100nm FS could be generalized to other substances injected into the CSF, such as small molecules, proteins, or gene therapies. However, the kinds of differences observed for FS were of an order of magnitude that would be expected to influence the activity of therapeutic molecules. These results therefore highlight the need for additional work to further elucidate how microanatomy of the leptomeninges and regional CSF dynamics influence the distribution and activity of delivered agents.

In addition to inadequate distribution, many compounds injected into the CSF also suffer from short half-lives, typically on the order of a few hours[121]. This rapid clearance gives minimal time for the drug to distribute along the neuraxis to its target

before being cleared. Here, we found 100 nm FS, which are non-degradable, remained distributed throughout the neuraxis for over 3 weeks. This long residence time may be useful from a drug delivery perspective, allowing ample time for a drug carrier to distribute to target regions, interact with cells, and release its payload over days to weeks. Considering the continuous turnover of CSF multiple times a day (4x/day in human, 12x/day in mice)[95,99], the prolonged retention of our 100 nm FS was unexpected. It is likely that the long residence time is a function of FS size. CSF clearance is proposed to occur through multiple routes, including, 1, direct to blood transfer through arachnoid villi, 2, movement across the cribriform plate into the nasal mucosa, and, 3, perineural transport along both cranial and spinal nerve roots. The significance of each of these routes across species is often debated [94,110,172–174]. Both our IVIS and confocal data suggest the majority of FS clearance occurs from the brain compartment with minimal clearance along the spinal cord. In agreement with prior works in rodents, we see strong evidence for CSF movement across the cribriform plate into the nasal mucosa as a major clearance route for FS at all time points. Although we do observe some FS being cleared to the spleen, suggesting FS are accessing the blood, we are unable to discern whether these come from FS that leaked into the muscle at the injection site or FS cleared from CSF into blood. One possible explanation for the lack of FS along the dorsal brain is due to clearance into venous circulation through arachnoid villi along the Superior Sagittal Sinus (SSS); however, recent works suggest direct CSF to blood clearance is minimal in mice[172,173] and we failed to observe direct interactions of the FS within the SSS in coronal sections. We consistently observed FS interactions with exiting nerve roots along the spinal cord but were not able to follow them into the periphery. While our data suggests minimal change in FS concentration along the spinal cord over time, FS exiting into the periphery combined with FS in the cisterna magna acting as a source may contribute to

the observed lack of clearance and the concentration gradient along the spinal column. Future studies using whole body imaging would be necessary to fully understand the contribution of each of these clearance routes in the context of nanoparticle distribution.

Nanoparticle size is one of the most important biophysical parameters governing nanoparticle fate following delivery by most routes of administration, including intravenous[30,32], oral[34,175], intranasal[35,36], or convection enhanced delivery[37,38]. Due to the small pores formed by the heterogeneous distribution of arachnoid trabeculae within the leptomeningeal space[176,177], we expected that large nanoparticles would not be capable of traversing the subarachnoid space to reach CNS tissues distant from the injections site. Although it's known a small population of DepoCyt, a 10 μm multilamellar liposome, reaches the lumbar region within a day following intraventricular administration in humans, we expected the smaller mouse anatomy would be more restrictive to microparticle movement. In contrast to this expectation, we found 10 μm non-PEGylated FS were capable of navigating the SAS to the sacral spinal cord within 2 hours of IC administration in mice. However most distal slices contained no FS and those that did never contained more than 1 FS/slice. While these microparticle systems can help overcome the issue of rapid drug clearance through prolonged drug release, the minimal number of FS in distal regions means these systems must still inevitably rely on the drug to diffuse or be carried away from the particle to its target. Smaller nanoparticle systems, such as the 100 nm NPs used here, should not need to rely on drug movement due to their more uniform and complete distribution. In addition, their small size means they can be easily taken up into cells, allowing for opportunities to potentially increase delivery to specific cells or regions through targeting. As anticipated, the minimal penetration of 100 nm nanoparticles across the pia mater or diffusion along perivascular routes in the parenchyma, limiting their use for applications requiring delivery to deep

CNS regions. Although nanoparticles as large as 100 nm can maneuver through brain perivascular spaces under convection enhanced delivery[38], sub-50 nm and ideally >20 nm nanoparticles are necessary to achieve significant penetration from the SAS into the brain[178,179]. The retention of 100 nm FS within the leptomeningeal space does support future work examining their potential for overcoming the pharmacokinetic limitations of therapies for treating diseases of the meninges, including meningitis, meningiomas and leptomeningeal metastasis from solid tumors. Ultimately, our data provide the first direct evidence that 100nm NPs are capable of distributing rapidly through the leptomeninges of the brain and spinal cord following cisternal administration in healthy mice, which opens new therapeutic opportunities to consider delivery of drug loaded NPs via this administration route.

3.6. Tables and Figures

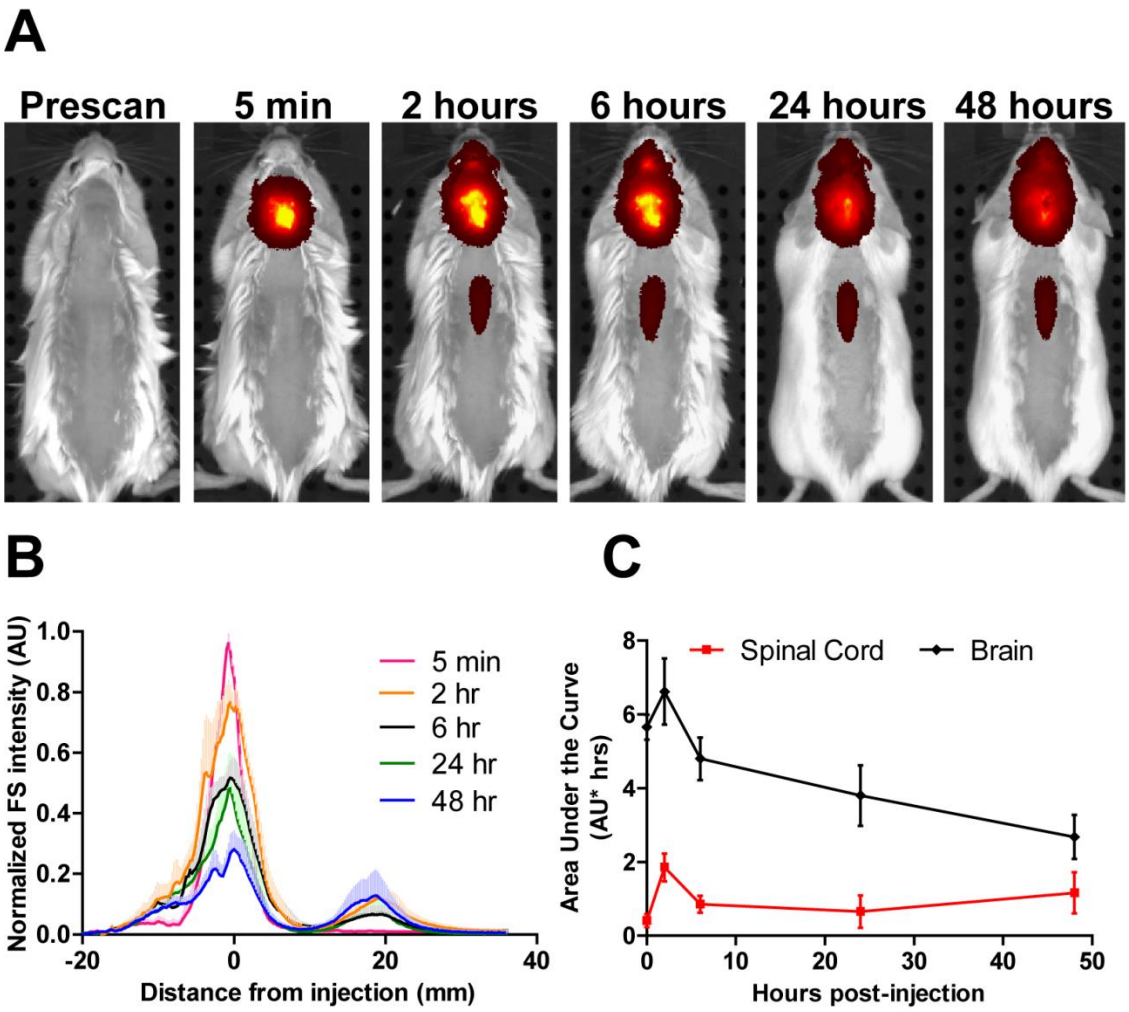

Figure 3.1: IVIS tracking of FS distribution after IC administration in intact healthy mice. (A) Representative images showing the spread of FS away from the cisterna magna over time. FS were detectable along the spinal cord by 2 hours but only along the mid of the back unobstructed by the extra muscle of the fore and hind legs. (B) Graph of FS intensity along the neuraxis quantified using a line profile from nose to tail. The FS signal was normalized within each mouse to the max intensity at 5 min and averaged across mice (n=4 mice). (C) AUCs of the brain signal (-20 to 10 mm) and spinal signal (10 to 40 mm) showed significant clearance of FS from the brain region from 2 to 48

hours ($p<0.05$, 1-way ANOVA), while the FS intensity along the spinal cord did not significantly change over the 48 hours. Mean+ SD shown in B to help keep lines visible. AUC points show mean ± SD.

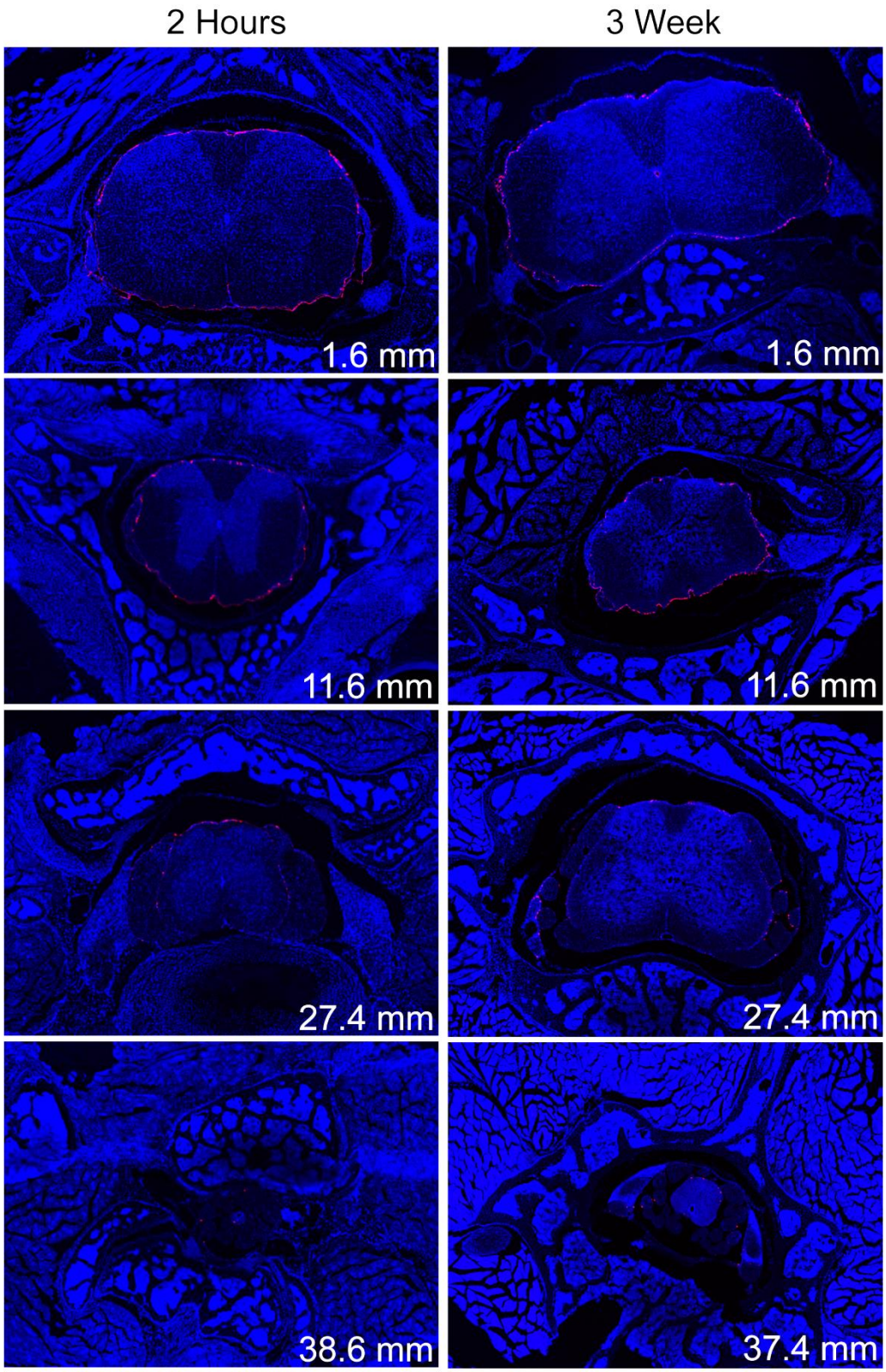
2 Hours
3 Week
1.6 mm
1.6 mm
11.6 mm
11.6 mm
27.4 mm
27.4 mm
38.6 mm
37.4 mm

Figure 3.2: Representative confocal images of FS distribution at along the spinal cord at 2 hours and 3 weeks. FS (red) distributed to the sacral regions of the spinal column within 2 hours and remained for over 3 weeks. Even at later time points, the FS appeared to be confined to meninges with minimal evidence for parenchymal penetration. The location of the slice along the spinal column is given in the lower left. Equivalent linear adjustments were made to the FS signal in each image to enable better visualization. Cell nuclei (DAPI) is shown in blue.

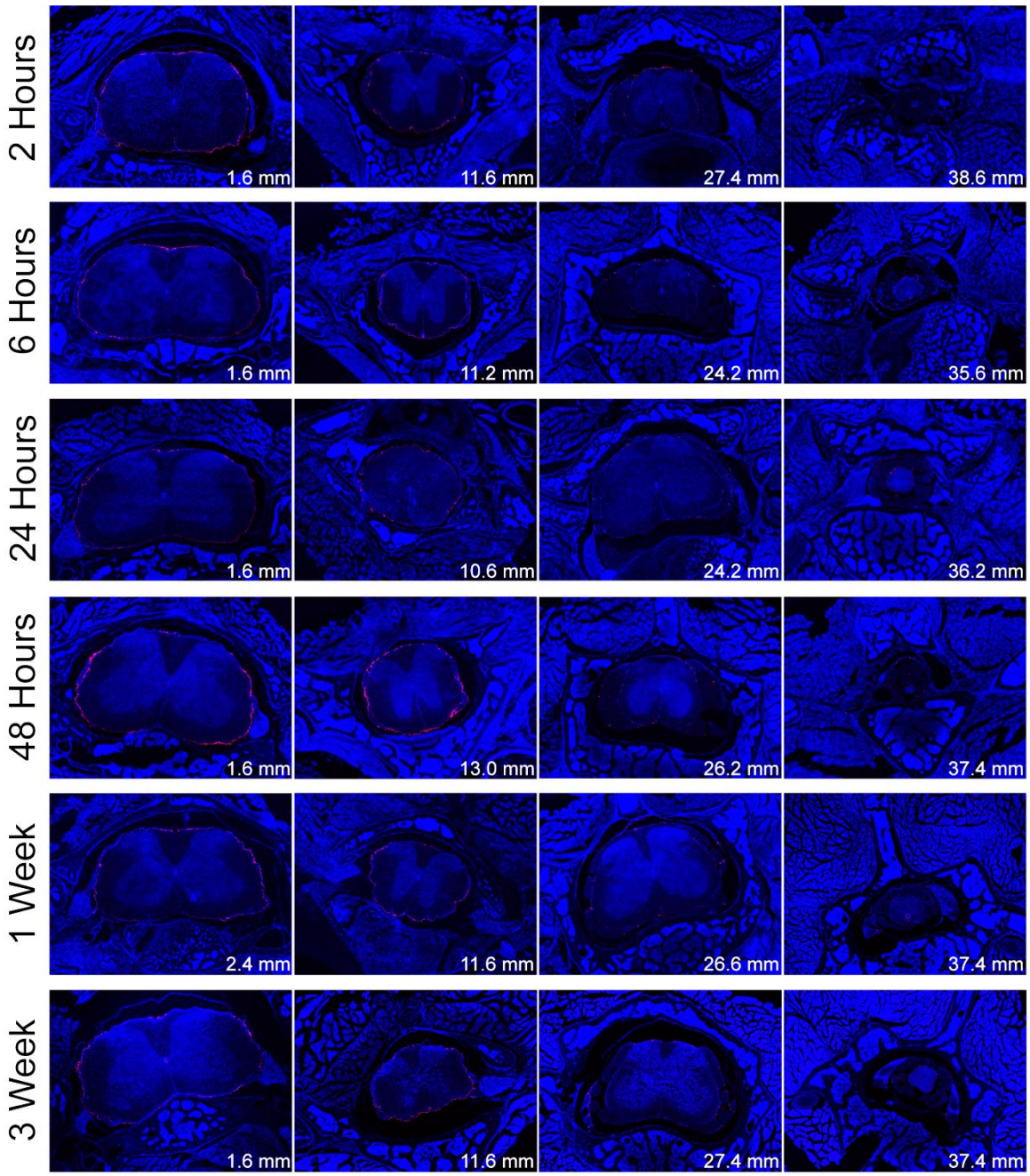

Figure 3.3: Representative confocal images of FS distribution at different locations along the spinal column over time. FS delivery along the spinal column appeared to be consistent over time. Equivalent linear adjustments were made to the FS signal in each image to enable better visualization. Cell nuclei (DAPI) is shown in blue.

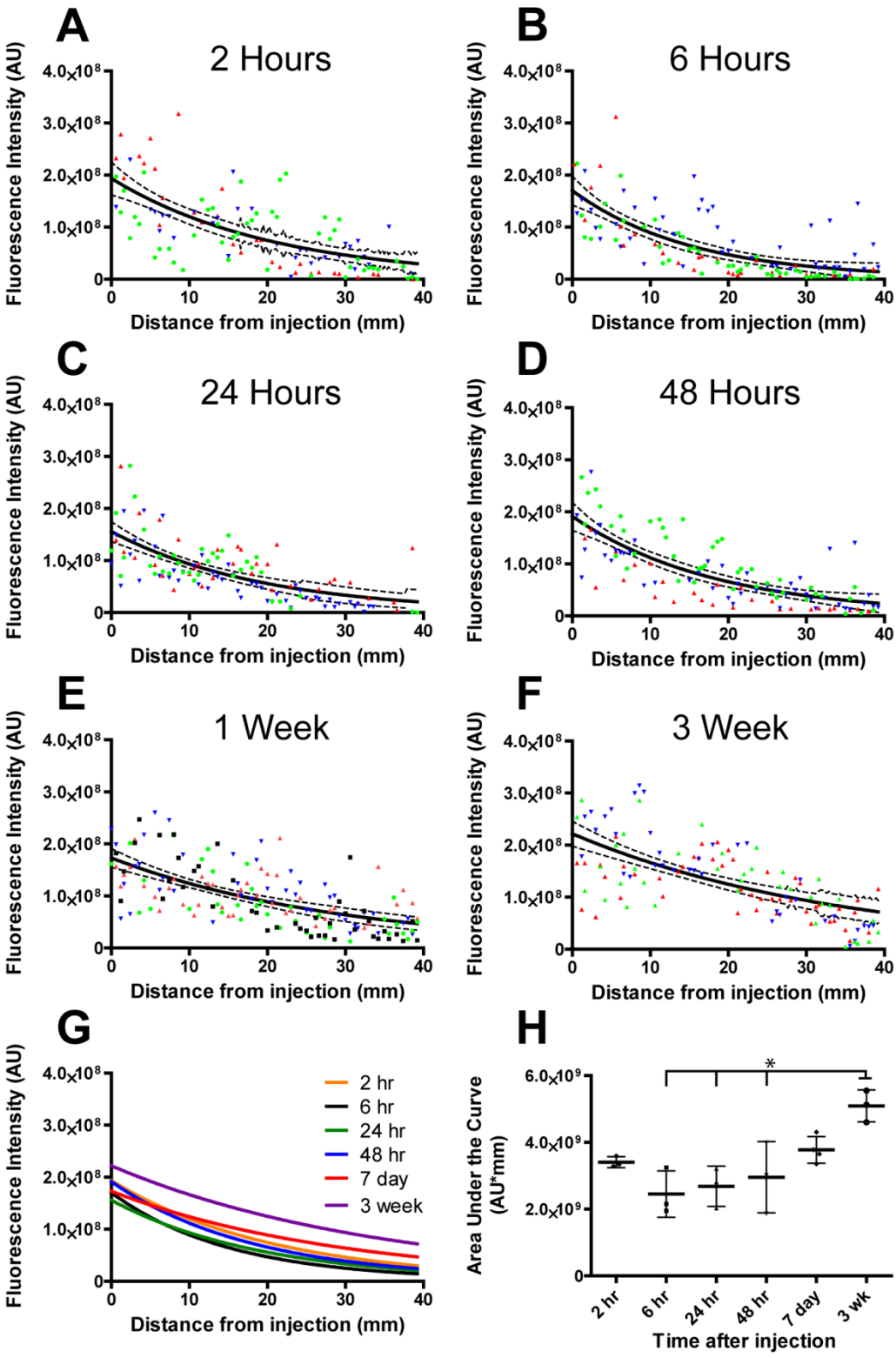
A
2 Hours
B
6 Hours
C
24 Hours
D
48 Hours
E
1 Week
F
3 Week
G
H
Fluorescence Intensity (AU)
Distance from injection (mm)
4.0x10^8
3.0x10^8
2.0x10^8
1.0x10^8
0
0
10
20
30
40
2 hr
6 hr
24 hr
48 hr
7 day
3 week
Area Under the Curve (AU*mm)
6.0x10^9
4.0x10^9
2.0x10^9
*
2 hr
6 hr
24 hr
48 hr
7 day
3 wk
Time after injection

Figure 3.4: Quantification of FS intensity along the spinal column following IC injection. (A-F) Scatter plots for each time point showing the distribution of measured FS intensity and the resulting exponential curve fit of all the data points (solid line) with the 95% confidence interval (dashed line). Each point represents the measured intensity within a given tissue slice, and within each graph, the same color and shape represent tissue slices from the same animal. (G) Single graph showing the shape of the FS intensity curve fits remained constant across time points. (H) AUC of the curve fits for individual mice at each time point shows FS delivery to the spinal cord trended upwards over time and was significantly higher at 3 weeks compared to 6, 24 and 48 hours ($p<0.05$, 1-way ANOVA with Bonferroni's Multiple Comparison Test). Mean ± SD shown.

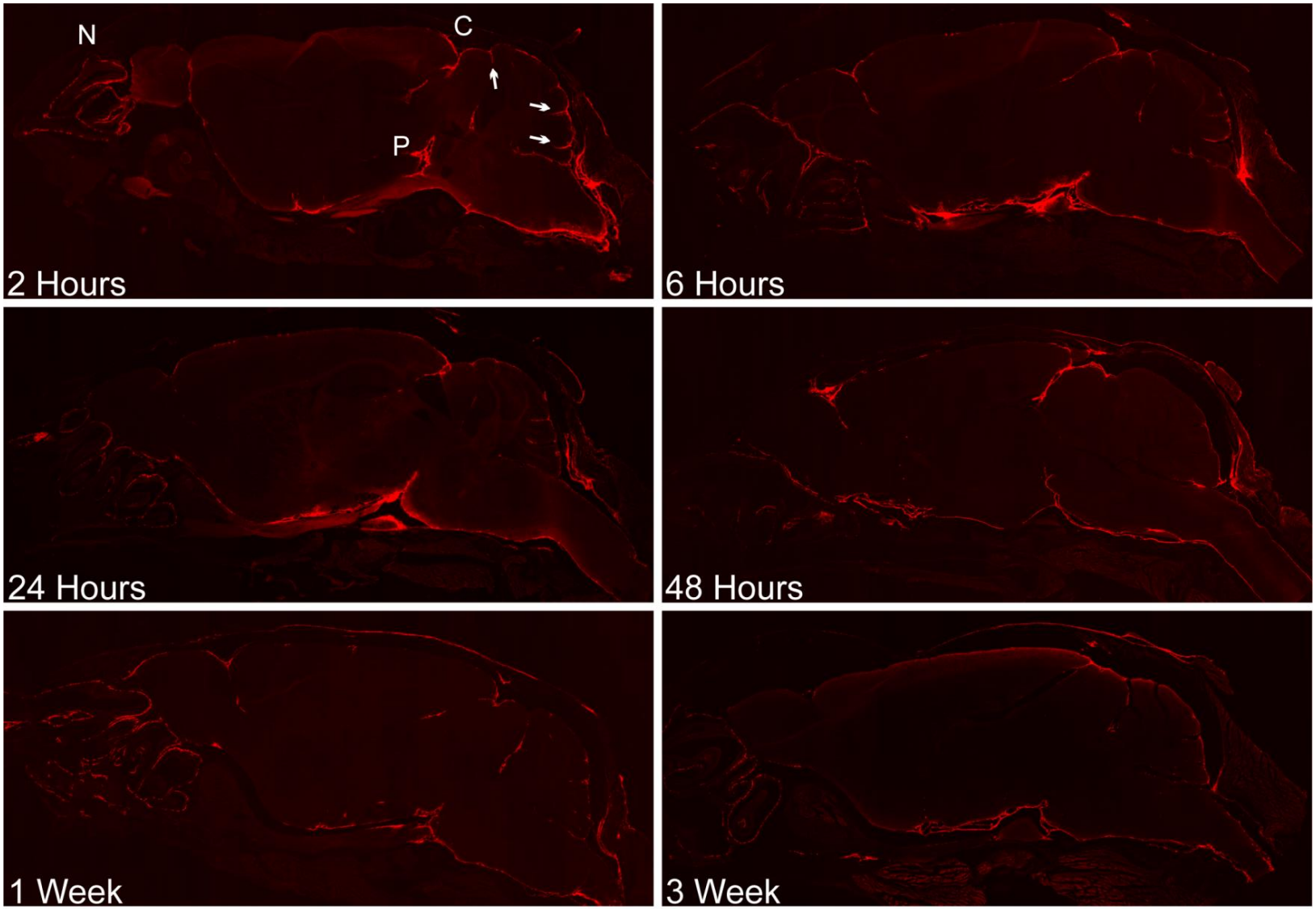
N
C
P
2 Hours
6 Hours
24 Hours
48 Hours
1 Week
3 Week

Figure 3.5: Representative confocal images of FS distribution around the brain. FS (red) were distributed around the entire brain and could be seen following the meninges into the sulci of the cerebellum (arrows). There was a strong preference for ventral distribution and consistently high delivery to the supracerebellar cistern (C) and pituitary recess (P). Clearance of FS across the cribriform plate into the nasal mucosa (N) was seen at all time points. Qualitatively, a general decrease in total FS intensity was observed over time. Linear corrections were applied equally across images to better show FS distribution and the gross anatomy of the brain.

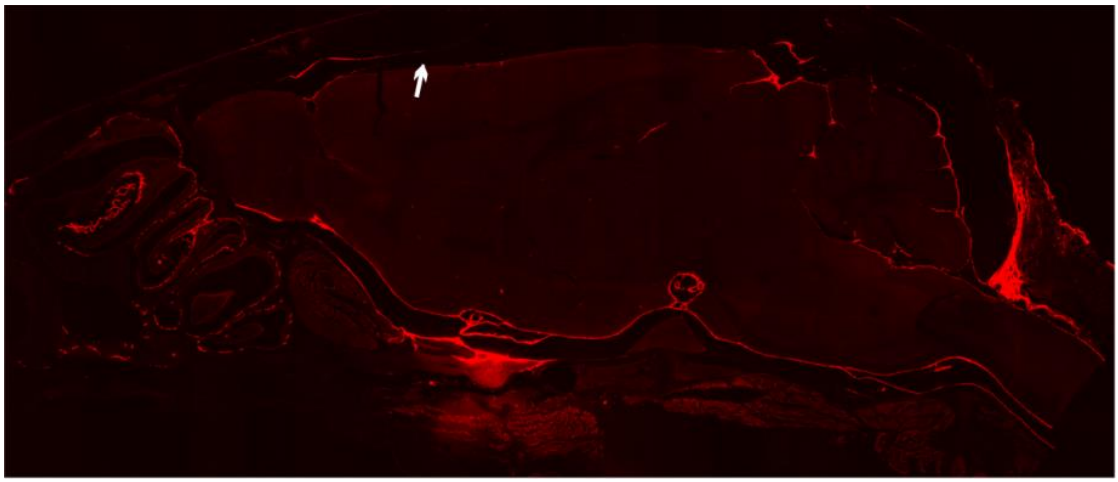

Figure 3.6: Mouse position does not affect FS distribution around the brain. Brain image from a mouse allowed to recover on its back during the 2 hours after injection. FS (red) distribution was still favored towards the ventral brain and minimal delivery was observed to the prefrontal cortex regions of the SAS (arrow).

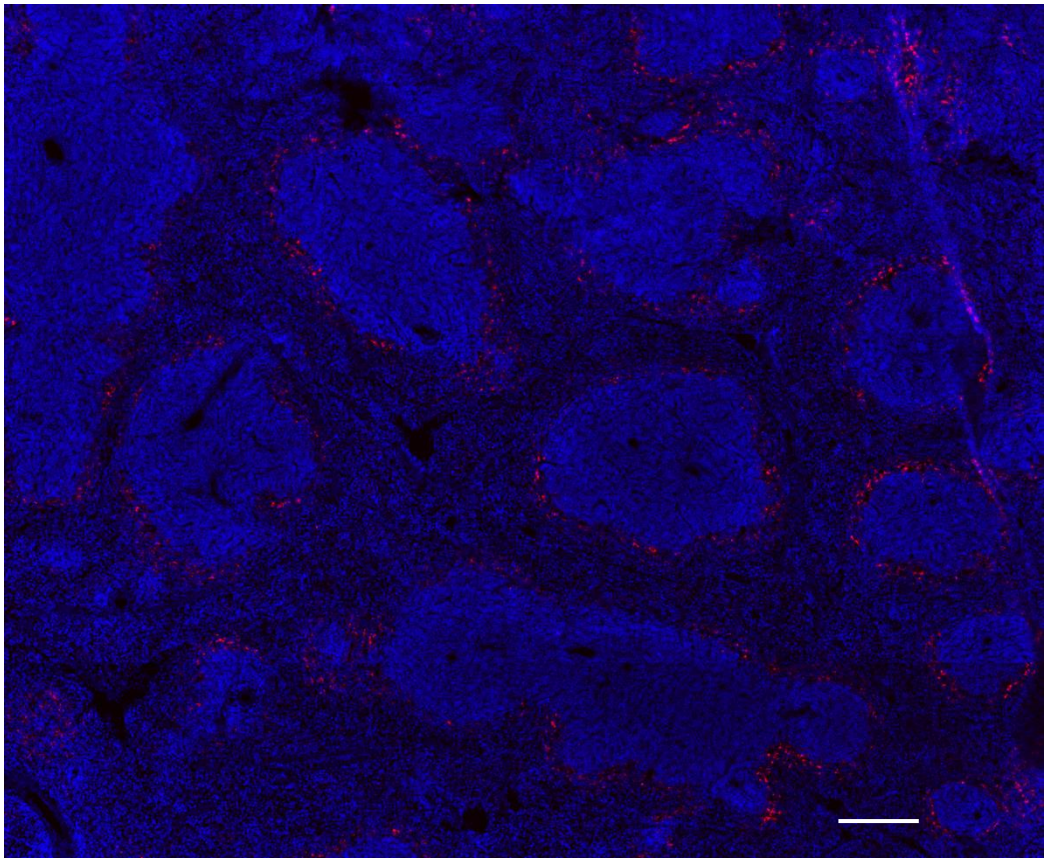

Figure 3.7: Representative confocal image of FS distribution to the spleen at 2 hours. FS (red) appeared to be localized around the white pulp. Cell nuclei (DAPI) shown in blue. Scale bar = 100 μm

CHAPTER 4

Evaluation of Nanoparticle Delivery to Leptomeningeal Metastasis by Intrathecal Administration and the Effects of CGKRK-targeting on Nanoparticle Fate

4.1. Abstract

Medulloblastoma (MB) arises in the cerebellum and is the most common pediatric brain tumor. While there are some effective treatment options for the primary tumor, patients exhibiting leptomeningeal metastasis (LM) have a significantly worse prognosis. LM involves the spread of the tumor to the cerebrospinal fluid (CSF) and infiltration into the meninges surrounding the brain and spinal cord. Intrathecal (IT) injection of chemotherapy directly into the CSF is an appealing approach to avoid systemic barriers to treatment, but poor distribution and rapid clearance of IT therapies has limited efficacy of this approach. We have previously shown that IT administered nanoparticles (NPs) exhibit prolonged wide spread distribution along the subarachnoid space of the neuraxis in healthy mice, but their potential for delivery to LM remains unexplored. Modification of NP with targeting ligands has been shown to be a potential strategy to increase or prolong NP localization with target cells after intravenous administration, which opens the possibility that this approach could be useful for enhancing NP localization with target cells when NPs are administered IT. Thus, the goal of this work was to evaluate the ability of IT administered NPs to localize with LM lesions and test the effects of an LM-targeting ligand on NP fate within the CSF. We identified CGKRK as an LM-targeting peptide in a mouse model of LM and showed CGKRK-targeted NPs exhibited altered distribution within the CSF compared to non-targeted. Although we did not find any benefit from targeting to increase NP localization with LM, both targeted and non-targeted NPs were found to distribute through the CSF

and penetrate into LM lesions around the entire brain. These data support future development of drug loaded NPs for delivery to LM after IT administration and open new avenues for developing targeted systems via this route of administration.

4.1. Introduction

Medulloblastoma (MB) is the most common malignant pediatric brain tumor. Although MB arises in the cerebellum, approximately 1/3 of patients with MB exhibit Leptomeningeal Metastasis, which is characterized by the spread of the tumor through the cerebrospinal fluid (CSF) to the meninges surrounding the brain and spinal cord[100–102]. Because LM cannot be surgically resected, it must be treated with a combination of high dose chemotherapy and cerebrospinal radiation. However, the blood-brain and blood-spinal cord barriers restrict CNS delivery of nearly all systemically administered drugs, and long-term outcomes for patients affected by LM remain poor[106,107]. Intrathecal (IT) injection of chemotherapies directly into the CSF has been used as an alternative to systemic administration, but poor distribution of active agents and toxicity has limited the efficacy of IT therapy for chemotherapy in the clinic[111–113]. Thus, new approaches are needed to overcome the limitations of free drug movement in the CSF and enable more effective LM treatments.

In previous work, we have shown the ability of nanoparticle (NP) encapsulation to overcome the limitations of free drug distribution and improve drug efficacy following intravenous administration[1]. Additionally, we demonstrated the ability of 100 nm NPs administered by IT injection to be distributed by the CSF to achieve rapid and wide spread delivery along the neuraxis of healthy mice. While these data support the feasibility of IT administered NPs to be delivered to LM lesions, which are exposed to CSF, the known issues with neurotoxicity for free drug highlight the need to develop strategies that will target NP delivery to malignant cells while sparing healthy tissues.

Surface modification of nanoparticle (NP) drug carriers with targeting ligands has been proposed as a method to enhance NP drug delivery to specific tissues and cells through interactions with cell surface receptors or extracellular matrix proteins[50,63,180,181]. Depending on the ligand and NP system, targeting has shown potential to improve NP efficacy through prolonged NP retention[65,69,70], increase payload delivery[55,69,182], enhance NP internalization[71,72] or direct NP fate to specific organelles[73,74]. Despite the extensive use of targeted NP systems with most routes of administration, including intravenous[23,63,69], intranasal[45,183,184], and convection enhanced delivery[50,185,186], the potential role of targeting for NPs administered by intrathecal (IT) injection remains unexplored. Access to the ligand's target has been shown to be one of the major limitations to achieving targeting by intravenous administration[55,64,187]. The NP must first be carried by the blood to the target tissue and then extravasate out of the blood vessel before the ligand can interact with its target. Given that LM lesions are in direct contact with the CSF, the over-arching hypothesis for this work was that the distribution of a NP administered IT could be altered through surface modification with targeting ligands.

No specific peptides have been previously identified to target LM. We therefore used bacteriophage biopanning to identify potential peptide candidates for LM targeting. Phage display allows for the expression of a wide diversity of exogenous peptides (10^9 or more unique sequences) and offers a powerful method to identify novel peptides that bind to LM lesions without necessitating pre-identification of a target receptor or molecule[188–190]. In addition to the potential peptides found by phage display, we also selected 3 known tumor-targeting peptides, CGKRK, CREQA and Angiopep, predicted to have targets expressed on the LM cells or within their microenvironment. The CGKRK peptide was discovered by *in vivo* phage display against squamous cell carcinoma[191] but

has been shown to possess a high affinity for both the tumor neovasculature and the tumor cells in multiple solid tumors[182,192–194]. The proposed binding target of CGKRK, heparan sulfate, was previously shown to be upregulated within the blood vessels of human cerebral tumors and the extracellular matrix of primary MB tumors[195,196]. CREQA, often referred to as CREKA, was also discovered by *in vivo* phage display and was found to bind to fibrin deposits within the blood vessels and stroma of multiple tumor types[197–200]. The final peptide, Angiopep, was designed for specific interaction with the low-density lipoprotein-related protein 1 (LRP-1) on the blood-brain barrier[201]. In addition to high expression on brain vasculature, LRP-1 has been shown to be upregulated on tumor cells in both neuroblastoma[202] and glioblastoma[203] brain tumors.

Here, we used a mouse MB model of LM to evaluate the capacity of 3 targeting ligands to bind to LM lesions *ex vivo*. Although all 3 of these peptides have been shown to improve NP interactions with multiple tumor types following intravenous administration, our studies are the first to assess their binding affinity for LM and to test their ability to improve NP interactions with LM lesions via IT administration. The identified LM-targeting peptide was attached to the surface of 100 nm PEGylated NPs by Michael-addition reaction. Finally, we tested the ability of targeting to alter NP fate *in vivo* in LM-bearing mice. Using a multispectral approach to allow for within subject comparisons, the distributions of targeted and non-targeted NPs were evaluated at 6, 24, 48 and 1 week after IT administration. These studies are the first to test whether surface modification alters NP distribution following IT administration and bring us closer to our long-term goal of developing NP systems for LM-targeted chemotherapy in MB.

4.2. Materials and Methods

4.2.1. Materials

100 nm carboxylate-modified FluoSpheresTM (red fluorescent, Ex/Em 580/605 and yellow-green fluorescent, Ex/Em 505/515), SuperBlock Buffer, streptavidin-Alexa Fluor 405 and streptavidin- Alexa Fluor 633 were purchased from ThermoFisher Scientific (Waltham, MA USA). Endotoxin free water (<0.0050 EU/ml) purchased from G-Biosciences (St. Louis, MO USA) was used for all buffers and washes. Poly(ethylene glycol)-amine (mPEG-Amine, 2 kDa MW) and maleimide-poly(ethylene glycol)-amine (mal-PEG-Amine, 2 kDa MW) were obtained from Creative PEGWorks (Chapel Hill, NC USA). 5-FAM N-terminal modified peptides (>90% purity): ADARYKS, IVTQIPM, CGKRK, Angiopep (TFFYGGSRGKRNNFKTEEY) and CREKA (CRQKA), and unmodified CGKRK peptide (>95% purity) were purchased from GenScript (Piscataway, NJ USA). Mouse anti-human CD2:biotin (clone LT2) was bought from Bio-Rad (Hercules, CA USA). NeuroCult Mouse Basal Medium was purchased from STEMCELL Technologies (Cambridge, MA USA). All other chemicals and reagents were purchased from Sigma-Aldrich, unless otherwise specified.

4.2.2. Bacteriophage Biopanning for LM Targeting Peptides

Phage biopanning was completed using the Ph.D.-7 Phage Display Peptide Library (New England Biolabs, NEB). We conducted 3 rounds of *ex vivo* screening, with each round consisting of 3 negative selections with freshly isolated neuraxis from healthy mice followed by a positive selection with a neuraxis isolated from mice with LM lesions. Neuraxis from healthy and LM bearing mice were freshly isolated before each incubation step and maintained in 1x PBS. For the first negative selection, 10^9 phage were incubated for 1 hour at 37°C with healthy meninges under gentle shaking. After 1 hour, the meninge-phage solution was centrifuged and the supernatant

(containing unbound phage) was transferred to a fresh plate containing a new healthy neuraxis. After 3 negative selections, the resulting supernatant was incubated once with an LM bearing neuraxis. The phage bound to the LM meninges were eluted into DMEM with 1% FBS using a dounce homogenizer and used for amplification for the next round of selections. All e coli. and phage cultures were performed as described in the NEB phage handbook. After 3 total rounds of selections, 48 phage clones were isolated and prepped for Sanger Sequencing using a QiaPrep mini-kit following the provided protocol.

4.2.3. FluoSphere PEGylation and Peptide Conjugation

Non-targeted carboxylate-modified FluoSphere™ (FS, 100 nm) nanoparticles were covalently modified with mPEG-Amine (2k Da MW) by carboiimide chemistry. FS in 500 µl aliquots were washed to remove the sodium azide using 0.5 ml Amicon-Ultra centrifugation filters (10k MWCO). Retained FS were resuspended with water bath sonication in 10 ml MES buffer (10 mM, pH 6). mPEG-amine (5x molar excess) was added to the FS and allowed to stir for 15 min. Next, 4 mg 1-Ethyl-3-(3-dimethylaminopropyl) carbodiimide (EDC) was added to the stirring solution. The reaction was left stirring for 3 hrs at room temperature before quenching with excess glycine (100 mM) for 30 min. Unreacted PEG, EDC, and glycine were removed with 3 centrifugation washes using 15ml Amicon-Ultra centrifugation filters (100k MWCO), and resuspended to 20 mg/ml in 1x PBS for storage at 4°C until use. Targeted FS (CGKRK-FS) were produced by the same methods except 10% w/w mal-mPEG-amine was added to the reaction. Following the initial washes to remove unreacted PEG, the FS were diluted in 5 ml MES buffer (200 mM, pH 5.5) and CGKRK peptide (5x molar excess) was attached via thiol-maleimide coupling for 1 hour at room temperature. Unreacted

peptide was removed by 3 additional centrifugation washes before resuspension to 20 mg/ml in 1x PBS.

4.2.4. FluoSphere Characterization

FS size and zeta potential was measured in 1 mM KCl before and after PEGylation using the NanoBrook 90Plus Zeta (Brookhaven Instruments, Holtsville, NY USA). Each sample was measured 10 times and averaged across 3 repeats. Peptide conjugation was confirmed by 1H NMR. Lyophilized FS samples before and after peptide conjugation were dissolved at 1 wt% in CDCl3 and analyzed by 1H NMR (400 MHz Varian).

4.2.5. In Vivo

All procedures and animal care practices were performed in accordance with the Barrow Neurological Institute's Institutional Animal Care and Use Committee. NOD SCID gamma (NSG) mice (Jackson Labs, Bar Harbor, ME USA) were used for all *in vivo* experiments.

4.2.6. Leptomeningeal Metastasis Model

Here, we utilized a novel genetically engineered mouse model of MYC-driven MB, developed in the Wechsler-Reya Lab[204] (See citation for detailed analysis). Briefly, this tumor model (referred to as MP tumors) uses postnatal cerebellar stem cells from C57 mice transfected to over-express MYC and dominant-negative mutant Trp53. MP tumors are serially passaged orthotopically in the cerebellum of mice to maintain key histological and genetic features of Group 3 MB. These tumors also express luciferase and a truncated version of human CD2, allowing for bioluminescent monitoring of tumor growth and immunofluorescent tracking of cells.

LM seeding of MP tumors was induced by injection of MP cells directly into the CSF via cisterna magna. Isoflurane (0.5-2%) was used to maintain proper depth of anesthesia (confirmed by toe pinch) throughout the procedure. Mice were mounted on

a stereotaxic frame (Kopf Instruments, Tujunga, CA USA) on top of an infrared heating pad. After shaving the fur, a sterile surgical site was prepped over the brain and neck using 3 alternating passes of betadine and 70% ethanol. A ~ 1 cm incision was made along the back of the neck before dropping the head from the bite bar to a 60° with the body. Blunt dissection was used to carefully part the muscle to expose the membrane covering the cisterna magna. An ice cold Hamilton syringe (29 gauge, 30° beveled needle) containing 10k MP cells in a 1:1 mixture of NeuroCult media and growth factor reduced Matrigel was inserted to a depth of 1.3 mm through the membrane, and the cells were injected over 1 min. The needle was left in place for an additional 2 min to reduce backflow. Staples were used to close the incision, and triple antibiotic ointment was applied over the wound. All animals received a subcutaneous injection of Buprenorphine SR (1 mg/kg) prior to surgery, and ibuprofen was provided in their water for 1 week to reduce pain.

4.2.7. Tumor Tracking

Tumor seeding and growth was monitored by bioluminescent imaging using the Xenogen IVIS spectrum imaging system, as previously described[1]. Briefly, mice were injected subcutaneously with 150 mg Luciferin/ kg 10 min prior to imaging, under 2% isoflurane. Tumor size was measured using the IVIS Living image software by drawing an ROI around each tumor signal.

4.2.8. FluoSphere Administration

FS were administered to CSF of LM bearing mice by the same procedure as tumor cells as described in 4.3.5, with minor alterations. In isoflurane anesthetized mice, a Hamilton syringe (29 gauge, 30° beveled needle) was used to inject 2 µl 1:1 mix of non-targeted FS (yellow) and CGKRK-FS (red) (20 mg/ml in PBS) over 1 min at a depth of 1

mm in the cisterna magna. The needle was left in place for 2 min after injection to reduce backflow, before closing the wound.

4.2.9. Neuraxis Collection

Mice were sacrificed at 6, 24 and 48 hrs, and 1 week (n=3-4/ time point) post FS administration, to examine FS distribution and localization with LM lesions. Mice were sacrificed by cardiac perfusion with 15 ml heparinized PBS (1000U/ml) followed by 10 ml 4% paraformaldehyde (PFA). The entire brain and spinal column, from nasal sinuses to sacral spinal region, was isolated by removing the majority of muscle and skin but leaving the bone left intact to preserve the integrity of the leptomeninges. The neuraxis was post-fixed in 4% PFA for an additional 24 hrs, before decalcification of the bone in a 4% HCl and 4% Formic Acid v/v solution, replaced daily, for 5 days. Following decalcification, the neuraxis was transferred to a 30% (w/v) sucrose solution for 48 hrs for cryoprotection. The brain and spinal cord were separated at the C1 vertebrae. One hemisphere from each brain was embedded in OCT and frozen at -80° C before slicing into 20 μm sagittal sections.

4.2.10. Ex Vivo CGKRK-FS Targeting

To confirm peptide functionality after conjugation to the FS, brains were isolated from LM bearing mice and incubated ex vivo with either non-targeted or CGKRK-modified FS. Each brain was incubated for 4 hrs with 0.2 mg FS at 37°C with rocking. Each sample was washed 3 times with 5 ml PBS for 20 min with agitation to remove unbound FS, before being fixed in 5 ml 4% PFA for 24 hours. 30% sucrose for 48 hrs was used to cryoprotect the brains before being embedded in OCT and frozen at -80° C for slicing.

4.2.11. Image Collection

A Zeiss LSM confocal microscope was used for all imaging. Laser intensities and gains were kept constant within each experiment. It was confirmed that the particles did not show spectral overlap under our imaging conditions. Using mixtures of red and green FS, the gains for comparing the targeted and non-targeted FS were set such that the total fluorescence measured with ImageJ from both formulations would be equivalent at equal concentrations.

4.3. Results and Discussion

4.3.1. Bacteriophage Biopanning and Free Peptide Binding to LM

In chapter 3, we showed the safety and feasibility of 100 nm PEGylated NPs to achieve widespread distribution along the neuraxis in healthy mice, following administration into the CSF through the cisterna magna. Surface modification of NPs with targeting ligands has been extensively studied for most routes of administration, including intravenous[23,63,69], intranasal[45,183,184], and convection enhanced delivery[50,185,186], but to our knowledge, never for IT delivery. Since a cell's microenvironment is known to affect both protein expression and receptor localization[205–208], it is important to test ligands against cells as close to their native state as possible. Thus, we utilized *ex vivo* incubation for our bacteriophage biopanning. Although some of the outermost meninges are lost during brain removal, the *ex vivo* brains are expected to better maintain native cellular and extracellular architecture of the LM lesions compared to *in vitro*. Additionally, we wanted to isolate peptides displaying minimal interaction with healthy tissue to reduce off target NP delivery. Since our data in chapter 3 suggests 100 nm NPs have minimal penetration across the pia mater into the CNS parenchyma, we used healthy neuraxis to select against peptides with an affinity for healthy meningeal cells and the arachnoid trabeculae. From the 3 rounds of biopanning, we found the peptides

ADARYKS and IVTQIPM to appear the most frequently and were selected for further evaluation. To evaluate the ability of the identified and pre-selected peptides to bind to LM, we incubated fluorescently labeled ligands, ADARYKS, IVTQIPM, Angiopep, CGKRK, and CREKA, with brains that were extracted from LM-bearing mice. Ideally, we would have tested peptide binding by directly injecting fluorescently labeled peptides *in vivo*, but issues with fluorescence stability through the decalcification process prohibited our ability to interpret the results. While all 5 of the peptides were found to bind to LM cells in both large and small lesions, CGKRK consistently displayed the greatest signal localization with CD2+ tumor cells (Figure 4.1). Using healthy brain controls, we also tested peptide binding specificity for LM compared to non-specific binding to healthy meninges. While all the peptides exhibited some degree of non-specific binding to healthy brain, minimal to no signal was seen in the CGKRK brains without increasing the image gain compared to the other peptides (Figure 4.1). Qualitatively, CGKRK exhibited both the lowest overall binding to healthy and the greatest difference in binding between healthy and LM cells among the peptides. Thus, we moved forward with the attachment of CGKRK to the FS.

4.3.2. FS PEGylation and Peptide Conjugation Characterization

Amine-PEG was covalently bound to the FS surface by EDC chemistry. DLS measurements showed an expected increase in average FS diameter from 100 to 108 nm and a shift in zeta potential from -45 mV towards a more neutral charge of -5.3 mV following the conjugation of PEG to the surface. CGRKR was attached to maleimide functionalized PEG on the FS surface via a Michael-type addition reaction with the free thiol on the N-terminal cysteine. The attachment of CGKRK also produced a further increase in size from 108 to 113 nm and caused a switch in zeta potential from -5.3 to 9.7 mV. The shift in FS zeta potential from negative to positive following peptide attachment

is expected to be caused by the positive charge of the KRK motif, suggesting successful attachment. To further confirm successful attachment of the CGKRK peptide, we ran ^{1}H NMR on maleimide functionalized FS before and after peptide conjugation (Figure 4.2). Although we were unable to directly detect the peptide by ^{1}H NMR, this is likely due to the low peptide content relative to PEG. As a surrogate, prior works conjugating similar short peptides have shown changes in the maleimide peak to accurately reflect peptide attachment[197,209]. A large peak at 3.6 corresponds to the successful attachment of PEG. Prior to peptide conjugation, there was a small peak at 7.9, confirming the presence of maleimide functionalized PEG, and the observed 30% decrease in maleimide after conjugation confirms successful CGKRK attachment.

4.3.3. In Vivo CGKRK-FS Targeting

The ability of CGKRK targeting to increase the delivery of FS to LM lesions was evaluated in LM bearing mice at 6, 24, 48 hours and 1 week after intracisternal administration. Due to the heterogeneous distribution of LM lesions between mice and the known potential for lesions to alter CSF flow[210], we were motivated to compare the distribution of targeted and non-targeted FS mixtures within the same subjects using a multispectral approach: differently colored FS were mixed together and administered to a single subject. We first confirmed that non-targeted red and green FS, when mixed together at the same concentration and administered to a single subject, exhibited equivalent distribution around the brain 2 hours after injection independent of color (Figure 4.3). Interestingly, we observed almost complete co-localization of the 2 FS signals. To ensure the observed signal overlap was not an artifact of the decalcification process or an issue of spectral overlap, we confirmed non-targeted FS distribution was significantly different between colors when FS were administered 2 hours apart instead

of simultaneously (Figure 4.3). These experiments confirm that FS color does not affect distribution, and, under the right conditions, we can observe differences in distribution.

The next experiments involved mixing targeted and non-targeted FS together to assess their distribution in LM bearing mice. Both CGKRK- and non-targeted FS distributed away from the injection site, through the meninges and around the entire brain. Surprisingly, the gross distribution pattern around the brain for both targeted and non-targeted FS was similar to the overall distribution patterns we previously observed for non-targeted FS administered to healthy mice (Chapter 3 and Figure 4.4). Specifically, the FS showed preferential distribution to the ventral brain, minimal delivery to the prefrontal cortex region of the SAS, and increased delivery to the supracerebellar cistern and pituitary recess. These data demonstrate that the presence of the lesion is not an impediment to NP movement through the leptomeningeal space. In all samples, both targeted and non-targeted FS were found to directly interact with LM lesions. In general, the intensity and patterns of FS delivery across lesions was found to vary significantly, both between mice (Figure 4.5A and B) and within the same subject (Figure 4.5 B and C). Although the FS were found to penetrate into most lesions, we did observe instances where the FS appeared to be confined to the meninges around the lesions (Figure 4.5D). Since CSF movement is expected to carry the FS through the SAS[113,211], the observed similar FS distribution compared to healthy would suggest the LM lesions were not disrupting the macro patterns of CSF flow around the brain. However, the variability in FS localization across lesions indicates the lesions were still altering the local mixing of CSF around them[96].

In our evaluation of targeting effects, we observed that the majority of detectable signal overlapped between targeted and non-targeted FS, both around the brain and within LM lesions. Although differences were observed in the distribution of targeted

versus non-targeted FS following IT injection (i.e., Figure 4.6), these differences were subtle, involving small fractions of weakly fluorescent FS. Targeting ligands have the potential to improve the localization and internalization of attached cargo through interactions with cell surface receptor or extracellular matrix proteins, which has been demonstrated in a number of other model systems [50,63,180,181]. Our over-arching hypothesis was that the presence of targeting ligand on the surface of NPs would enhance NP localization with LM. While the data presented here failed to show robust support of this hypothesis, several possible explanations exist.

First, it is possible that our approach for evaluating FS distributions does not possess the sensitivity needed to observe differences in targeted and non-targeted formulations. Our efforts to quantify differences in FS distribution were severely limited by the significant heterogeneity observed in FS intensity. To allow for accurate fluorescence quantification, signal gains were carefully adjusted to allow imaging parameters to be maintained across samples. The variability in FS delivery across a broad signal range within each lesion required adjustment of microscope settings to avoid saturation of the highest signals. This need to avoid saturation also inhibited our ability to detect and accurately quantify the smaller populations of low signal intensity FS within the lesion, where potential differences could be qualitatively observed. Similarly, the difference in magnitude of FS delivery across lesions meant the maintenance of imaging settings resulted in those lesions with lower total delivery to almost appear void of FS, but clear FS localization is seen at higher gains (e.g., Figure 4.7). Thus, it is possible that a smaller population of FS (e.g., non-aggregated FS) are in fact distributing differently, but that this low signal population is being lost in the visualization of brighter FS deposits. Better imaging techniques and/or drug distribution studies would be needed to explore this possibility.

As a second consideration, it is possible that CGKRK functionality after FS attachment was insufficient to achieve adequate binding with the LM cells. The peptide must be presented in both the proper orientation and be accessible beyond the PEG layer to allow for binding[212,213]. To further test CGKRK-FS functionality, we compared the co-localization of targeted versus non-targeted FS after *ex vivo* incubation with LM bearing brains. While we were able to observe differences in localization *ex vivo*, the effects of targeting were not as robust as the free peptide (Figure 4.8). These data indicate that some functionality of CGKRK is lost upon attachment to the NP surface. Future work modulating the PEG linker length[213] and peptide density[212] on the FS surface could potentially increase the binding affinity of CGKRK-FS to produce stronger interactions with LM cells. Given that we never observed any differences in distribution between 2 non-targeted FS *in vivo*, the minor differences observed between target and non-target, both *in vivo* and *ex vivo,* suggests the peptide was active. However, we cannot exclude the possibility the differences observed were actually caused by non-specific interactions due to the change in surface charge between our non-targeted and targeted particles. Future work would need to use a scrambled peptide with equivalent charge to our targeting peptide to differentiate between specific peptide-receptor interactions versus non-specific charge mediated alterations to NP distribution.

Third, the fact that we do not observe major differences in NP localization does not exclude the possibility that delivery of a NP payload could be altered. Prior works showing improved CGKRK-mediated targeting to tumors by intravenous delivery were tracking the distribution of DiR, a lipophilic fluorescent dye, encapsulated within the NP[182,192,214]. While encapsulated dyes like DiR are well retained within the NP in aqueous environments, they are not expected to be retained in vivo. We have previously shown when NPs interact with cells, DiR can be directly transferred into the lipid cellular

membrane in the absence of NP internalization, and remain after the NP has cleared[69]. The FS used here are internally dyed such that they do not exhibit direct transfer or leaching of the dye. Therefore, the prior CGKRK studies only definitively tell us the targeting was able to increase NP payload (DiR) delivery to the tumors but cannot determine if the actual NP fate was altered. In the absence of internalization, we have previously shown targeting ligand interactions with their receptor can still facilitate NP association with the cell but only for short periods under convective flow conditions[215], and that these enhanced cellular interactions can significantly increase NP payload delivery[69]. Thus, CGKRK mediated FS interactions with LM cells could have prolonged their association with cells, which would enable an increase in payload delivery, even though targeting was unable to overcome the convective forces of the CSF to significantly alter NP fate.

As a final consideration, it is important to acknowledge that our data support the alternative hypothesis that NP biophysical factors other than targeting are potentially more important for governing NP distribution by the convective forces of the CSF when NPs are administered IT. Similar observations on NP distribution following IV delivery have led to active discourse and some disagreement in literature regarding the significance of targeting in governing NP tissue distribution through the blood circulation relative to other major factors, such as NP size, surface charge, shape, and flexibility[55,64,187]. There is a growing body of evidence demonstrating that targeting does not produce dramatic changes in NP localization when measured at static time points. However, for the reasons outlined above, the lack of major change to NP localization by targeting does not exclude the possibility that drug delivery can still be impacted to provide an improvement in therapeutic efficacy.

4.4. Conclusions

Here, we identified CGKRK as an LM-targeting peptide and tested the ability of both targeted and non-targeted NPs to reach LM lesions after IT administration. We show CGKRK possessed strong binding and specificity for LM lesions and was able to increase NP interactions with LM lesions *ex vivo*. Although we were able to observe qualitative alterations to the NP distribution due to CGKRK targeting, we failed to observe a significant increase in targeted NP localization with LM *in vivo*. Regardless of targeting, we found 100 nm NPs administered IT, via the cisterna magna, were able to localize with LM lesions and penetrate throughout the tumors within hours of administration. These studies highlight the potential for NP drug carriers to deliver chemotherapy to LM after IT administration.

4.5. Tables and Figures

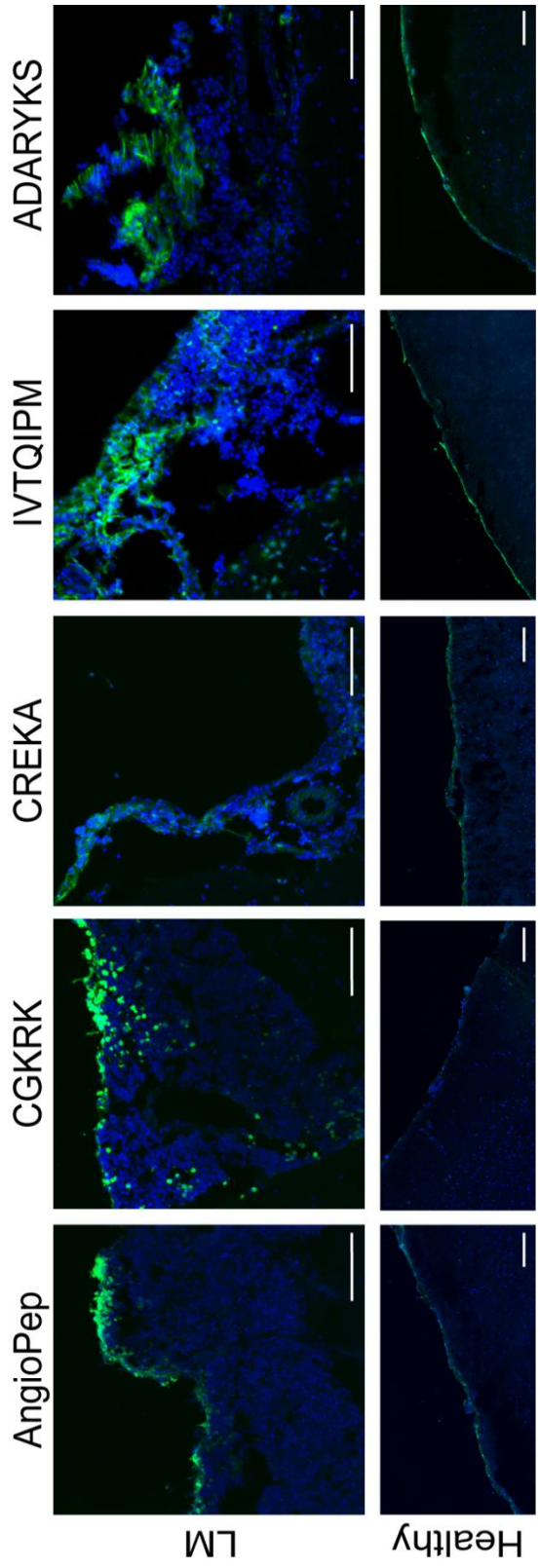

Figure 4.1: 5-FAM labeled peptide binding to LM lesions and healthy meninges *ex vivo*. The relative binding affinity of AngioPep, CGKRK, CREKA, IVTQIPM, ADARYKS for LM lesions were compared after *ex vivo* incubation with LM bearing brains. (Top panels) All 5 peptides (green) were found to localize to LM lesions (blue) with CGKRK showing the greatest binding across lesions. (Bottom panels) CGKRK also displayed the least non-specific binding to healthy meninges following *ex vivo* incubation with healthy brain controls. Cell nuclei (DAPI) are shown in blue. Scale bar = 100 μm

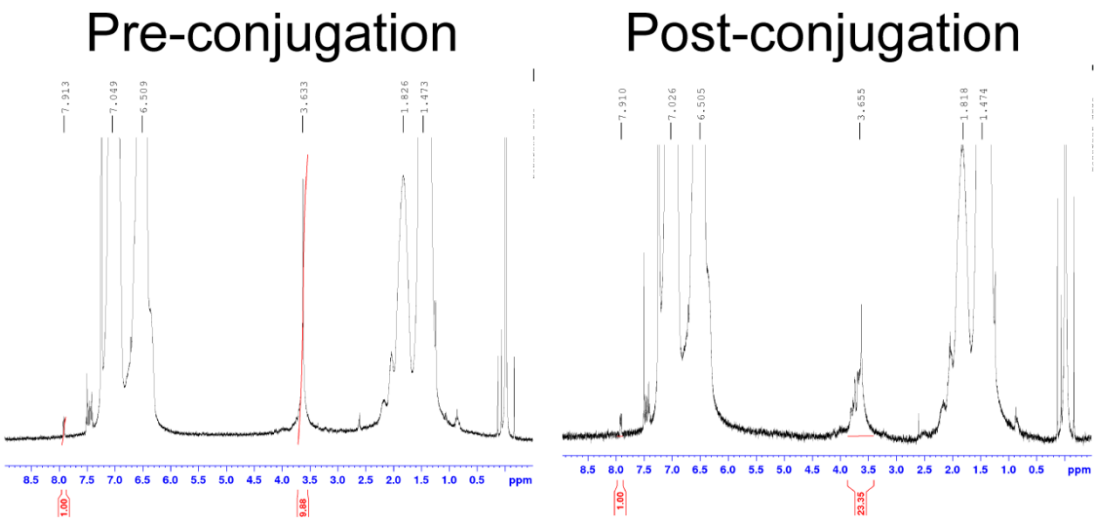

Figure 4.2: FS characterization by NMR. ^{1}H NMR spectra collected pre and post-CGKRK conjugation. A 30% reduction in maleimide (δ = 7.9) relative to PEG (δ = 3.6) was observed after peptide conjugation.

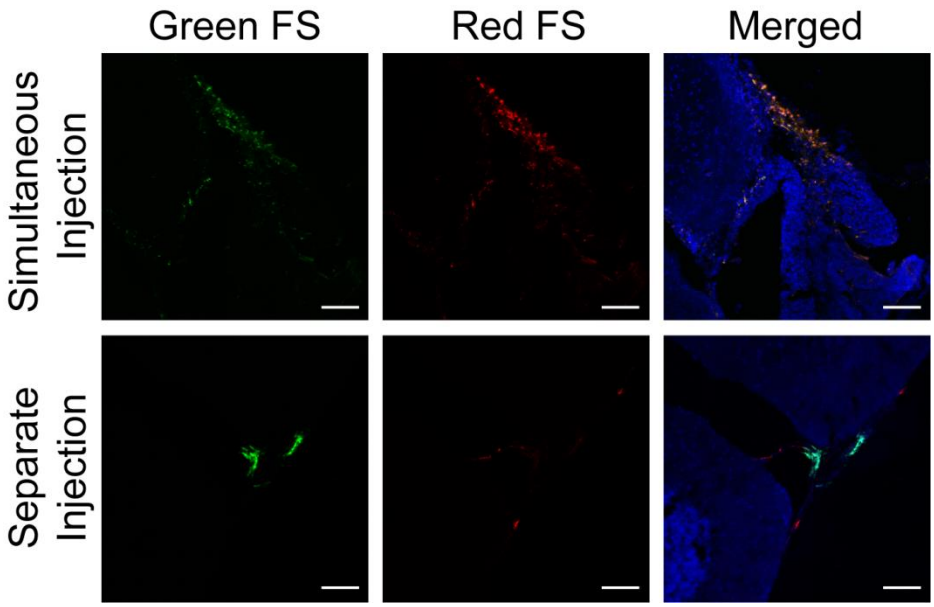

Figure 4.3: Testing the tracking of multiple FS formulations in a single mouse. (Upper panels) The simultaneous injection of a 1:1 mix of green and red non-targeted FS into the cisterna magna of mice resulted in complete signal co-localization between the 2 FS around the brain. (Lower panels) However, when the 2 colored FS were injected 2 hours apart, obvious differences in distribution could be observed. Cell nuclei (DAPI) are shown in blue. Scale bar = 100 μm

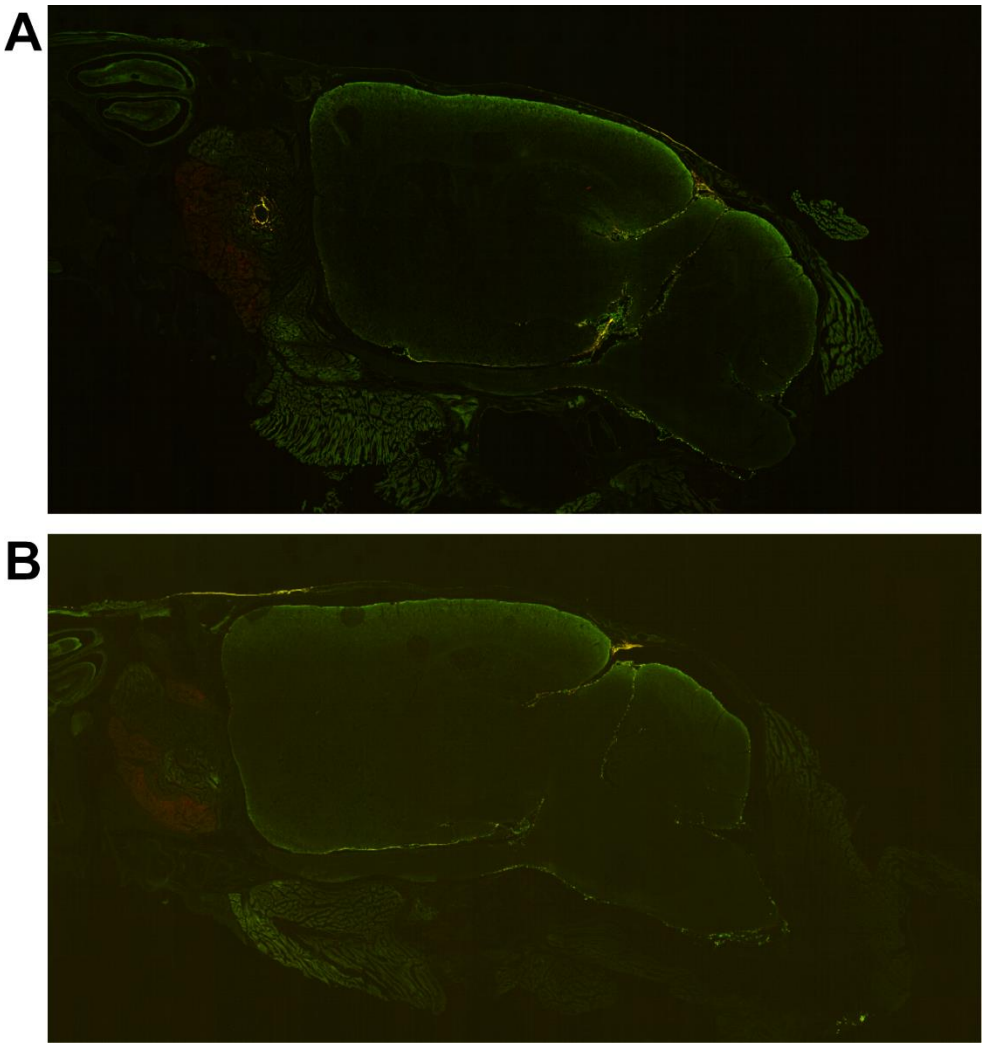

Figure 4.4: Targeted and non-targeted FS distribution around LM bearing brains. Sagittal brain slices from 6 (A) and 24 (B) hours after IT injection of CGKRK-targeted (red) and non-targeted (green) FS in LM bearing mice. Both FS were found to preferentially distribute along the ventral brain with minimal delivery to the prefrontal cortex region of the SAS and strong delivery to the supracerebellar and pituitary cisterns. The same patterns were also observed at 48 and 1 week after injection (not shown).

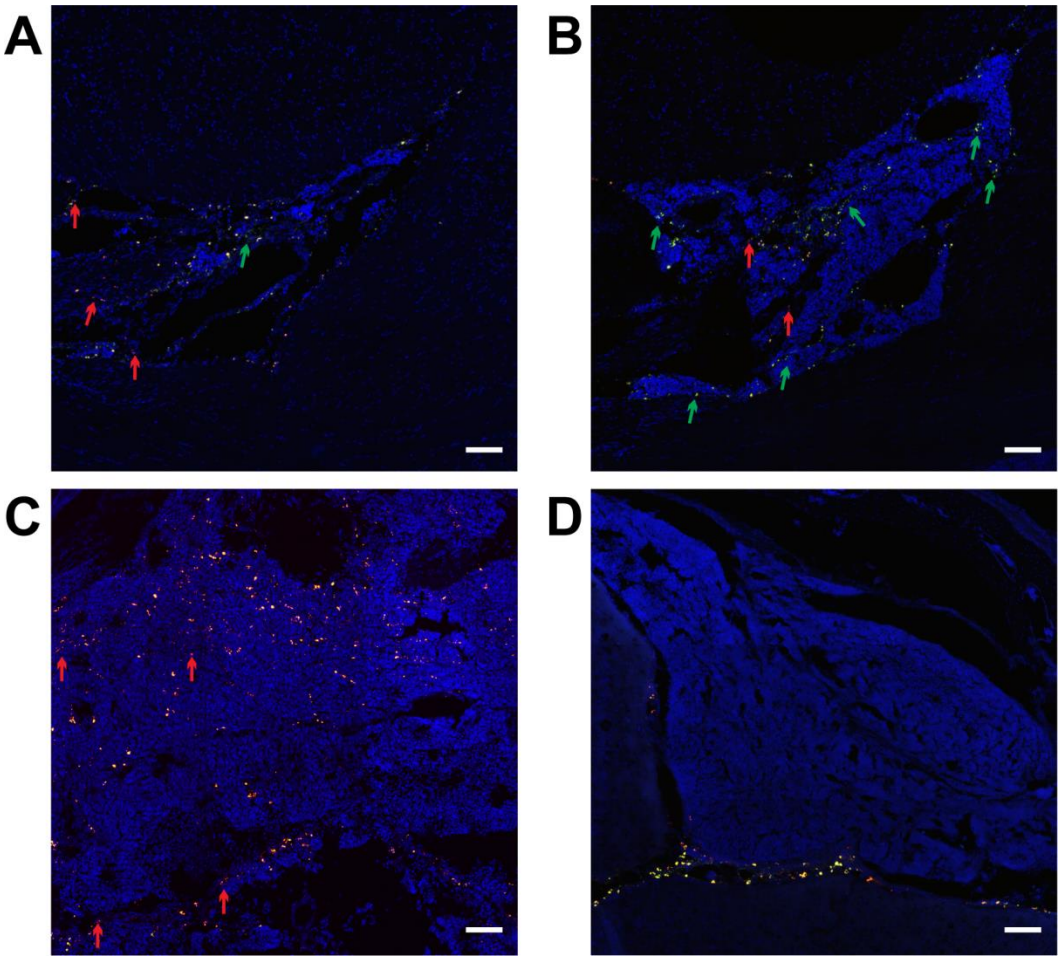

Figure 4.5: Targeted and non-targeted FS localization with LM lesions *in vivo*. Both CGKRK-targeted (red) and non-targeted FS (green) were found to directly interact with both large (A) and small (B) LM lesions (blue). While some lesions appeared to have more targeted (red arrows) versus non-targeted (green arrows) FS, these patterns varied both between mice (A vs B) and within the same mouse (A vs C). (D) Some lesions were also found to exclude the FS to the meninges around the lesion. Scale bar = 100 μm.

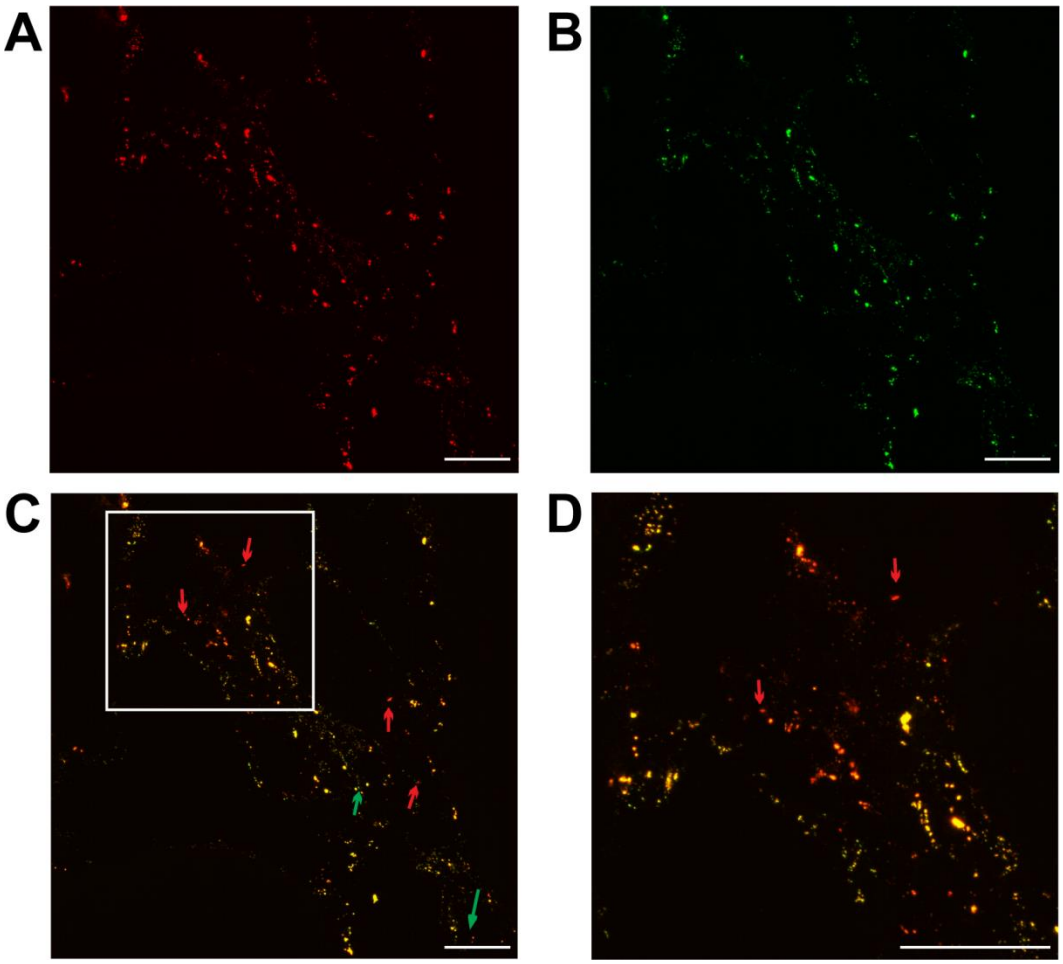

Figure 4.6: Detecting small differences in targeted and non-targeted FS localization *in vivo*. (A) Targeted (red) and (B) non-targeted (green) FS signals were found mostly co-localize within LM lesions (C). Within some regions, faint signals from small populations of both targeted (red arrows) and non-targeted (green arrows) FS could be seen exclusive of the other. (D) Zoomed in image of C showing regions with greater red targeted FS signal. Scale bars = 100μm.

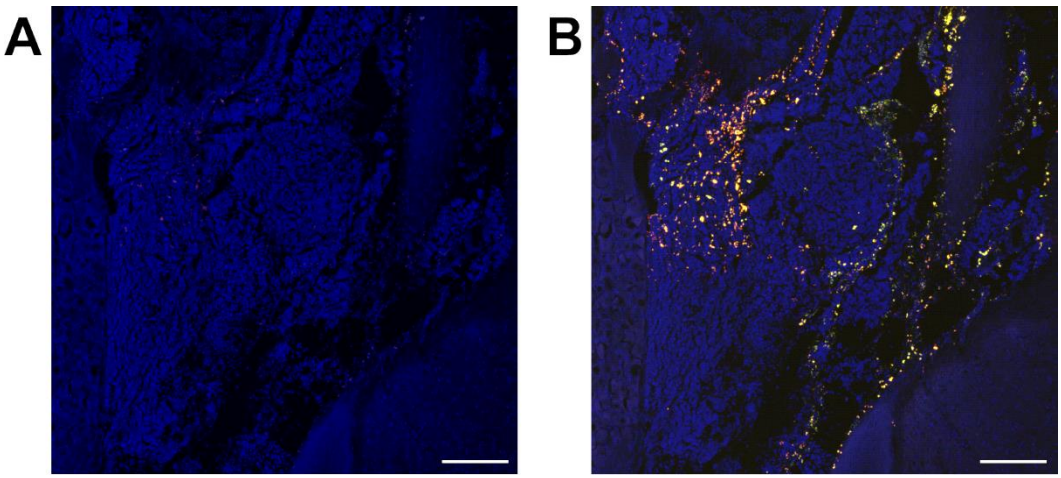

Figure 4.7: Limitations of FS detection. Maintenance of imaging setting across lesions (blue) meant those lesions with lower total FS delivery (A) to appear void of FS localization but (B) increasing the digital gain shows clear FS localization. Scale bars = 100μm.

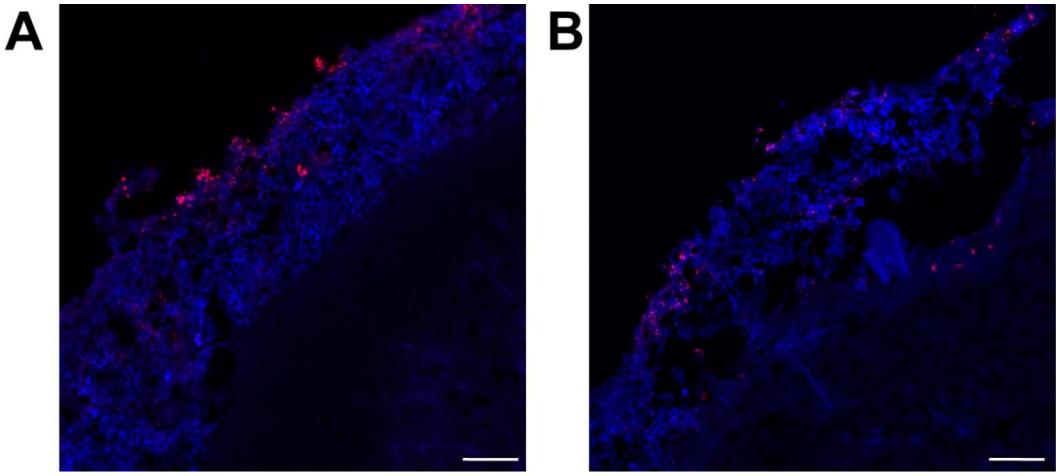

Figure 4.8: CGKRK-FS targeting *ex vivo*. Targeted-FS (A) showed a minor qualitative increase in localization with CD2 (blue) compared to non-targeted (B). Scale bars = 100μm.

CHAPTER 5

Conclusions and Future Directions

This final chapter summarizes the results achieved towards each of the specific aims and discusses the potential future directions to take these studies.

5.1. Specific Aim 1: Test the capacity of NPs to solubilize and enable the effective IV delivery of an otherwise intolerable lipophilic chemotherapy.

The first research chapter describes the fabrication of CPT-loaded PLGA NPs for intravenous delivery to orthotopic GL261 glioma tumors. PLGA is a biocompatible and biodegradable polymer capable of forming nanoparticles for the encapsulation and subsequent controlled release of a wide range of therapeutics. The hydrophobic core of PLGA NPs is especially effective at encapsulating hydrophobic and lipophilic small molecules like CPT. We demonstrate that a hydrophobic payload encapsulated within the PLGA NPs was delivered to the tumor core at ~10x higher levels compared to healthy brain. Payload delivery to the tumor core was higher for larger, more advanced tumors, indicating that interstitial pressure is not a barrier to effective small molecule delivery from NPs. Efficient loading of CPT was achieved at nearly 10 wt% in the NPs with sustained release occurring over 24 hrs. CPT solubilization within PLGA NPs reduced drug toxicity, enabling safe and tolerable intravenous administration at twice the free drug dose. This higher tolerable dose combined with the accumulation of NPs within the leaky tumor vasculature resulted in greater CPT activity within NP treated tumors compared to free drug. While the growth of intracranial GL261 tumors was unaffected by free CPT or blank NP (no drug), CPT-NPs administered at the max tolerable dose significantly slowed tumor growth and prolonged survival. These studies demonstrated

the solubilization of a lipophilic drug within PLGA NPs can improve drug tolerability and efficacy.

5.2. Specific Aim 2: Characterize the ability of NPs to be distributed by the convective flow of CSF to identify engineering opportunities for the design of IT NP systems.

The second research chapter characterizes the fate of 100 nm PEGylated NPs after direct administration into the CSF through injection into the cisterna magna of healthy mice. NP distribution was evaluated both *in vivo* using an IVIS imaging system and *ex vivo* in tissue slices using confocal microscopy. Both methods showed the rapid distribution of the NPs along the entire neruaxis, from olfactory bulb to sacral spinal cord, within 2 hours of injection, confirming that NPs are effectively carried by the convective movement of the CSF. Although the NPs' 100 nm diameter prevented any significant penetration into the brain or spinal cord parenchyma along perivascular routes, they were capable of following the meninges deep into the sulci of the brain and along nerve bundles. Despite the turnover of CSF multiple times a day, a significant population of NPs was retained within the SAS around both the brain and spinal cord for over 3 weeks post administration. NPs were found to clear from the brain CSF across the cribriform plate into the nasal mucosa, but NP delivery along the spinal cord did not significantly change over the 3 weeks. We also observed distinct regional distribution of the NPs due to the unique architectures of the brain and spinal cord. While NPs were relatively uniformly distributed around the circumference of the spinal cord, a significant preference for ventral distribution was observed around brain. Additionally, a high concentration of NPs was consistently found within the supracerebellar cistern and the pituitary recess. These results identified opportunities to tune NP drug release to take advantage of their prolonged retention and potential distribution patterns that would be

expected to influence therapeutic efficacy. Overall, this study demonstrated the potential of 100 nm NPs to be transported by the CSF to achieve rapid, wide spread delivery along the neuraxis.

5.3. Specific Aim 3: Identify a targeting ligand for LM cells and investigate the ability of targeting to alter NP fate after CSF administration.

This final research chapter discusses the identification of an LM targeting peptide and the effects of targeting on NP fate following IT administration. We evaluated the capacity of 3 targeting ligands to bind to LM lesions ex vivo, identifying the peptide CGKRK to have the greatest relative affinity and specificity for LM lesions compared to healthy CNS tissue and meninges. Following successful attachment to the NPs, we evaluated the fate of CGKRK-modified relative to non-targeted PEGylated NP after co-administration through the cisterna magna of LM bearing mice. Both NPs were distributed by the CSF through the meninges around the entire brain and were observed to interact with LM lesions. The overall distribution of the NPs around the brain was found to reflect similar patterns as those observed in Chapter 3 for non-targeted NPs in healthy mice, including strong ventral distribution, minimal distribution to the frontal cortex region, and high NP signal within the supracerebellar and pituitary cisterns. Total NP delivery across LM lesions was found to vary significantly, both within and between mice, but did not appear to be dependent on the size of the lesion. While the similar distribution compared to healthy suggests the LM lesions did not cause significant CSF flow disturbances on a macro scale around the brain, the highly variable FS delivery to lesions would indicate the lesions caused their own unique local CSF mixing. Although we were able to observe minor qualitative differences in distribution between the targeted and non-targeted NPs, the significant majority of the 2 NPs' signal were found to co-localize with each other, both around the brain and within LM lesions. No clear

benefit in LM localization of NPs was seen from CGKRK targeting in vivo. When we tested the functionality of CGKRK-NPs ex vivo with LM brains, we were able to observe a small increase in LM binding relative to non-targeted NPs. However, the binding capacity of CGKRK-NPs was clearly diminished compared to free peptide. Taken in sum, we hypothesize CGKRK was active after NP attachment, and the minor differences in NP distribution were due to increased NP interactions with LM cells; the overall NP fate was governed by the convective forces of the CSF. Regardless of targeting, we show IT administered NPs were able to localize with and penetrate into LM lesions, demonstrating their strong potential as a future system for delivering lipophilic chemotherapies to LM.

5.4. Future Directions

5.4.1. Improving Tracking of NP Distribution in the CSF

The work presented in this thesis provided us with the some of the first investigation into the engineering opportunities and potential barriers for the development of NP drug carriers for IT administration. Although we were not the first to inject NPs into the CSF[83–86,166,216,217], the collective understanding of how NPs move within the SAS is severely lacking, and our work begins to address this gap. Compared to the 175 intravenous NP papers already published this year on PubMed, there are only 3 IT nanoparticle papers. The work in Chapters 3 provides the first information into the distribution kinetics and fate of 100 nm PEGylated NPs injected IT. Our data highlights the potential for 100 nm NPs to be rapidly distributed throughout the entire meninges of the neuraxis by the convective flow of CSF and, to our surprise, be retained for over 3 weeks, despite the multiple CSF turnovers each day[99]. NP concentration was found to be nearly constant over the 3 weeks. We also found NPs distributed to the meninges along exiting nerve roots, which suggests potential opportunities to design a NP system to

provide sustained delivery of therapeutics for the treatment of diseases affecting motor neurons, such as amyotrophic lateral sclerosis. However, the localization with the nerves could also become an issue for chemotherapy delivery due to potential toxicity and nerve pain. Similarly, the heterogeneous distribution we observed around the surfaces of the brain were on an order of magnitude that could impact therapeutic efficacy or lead to toxicity. While these studies deepened our understanding of 100 nm NP movement within the CSF, they only provided the first snapshots into the potential of NPs for IT therapies. These initial observations emphasize that toxicity may be a key concern for designing NP systems for IT administration, and future studies could focus on engineering drug retention or NP localization to circumvent potential toxicity.

The work presented in Chapters 3 and 4 highlighted key limitations to our approach of looking at static endpoint analysis. The small volume and inaccessibility of the IT space combined with complexity of the CNS geometries restricted our ability to quantify over the meninges large surface area, leaving much of our data to be observational. Additionally, the heterogeneity of LM combined with our poor understanding of the complex interplay between LM lesions and CSF movement made the variability of static endpoint analysis difficult to interpret. Thus, for the future studies discussed in the following sections, we propose the use of Positron Emission Tomography (PET) to allow for quantitative, 3-dimensional (3D) analysis of radiolabeled-NPs (or drugs) after IT administration. PET is particularly sensitive in concentration quantification, but the limitations of PET's spatial resolution to about 1-2 mm[218] make the use of rat models in future work a better choice than mouse. PET could further be combined with the use of magnetic resonance imaging (MRI) to visualize the distribution of LM lesions along the neuraxis, allowing us to directly correlate NP or drug delivery with LM lesions[219,220].

5.4.2. Drug Delivery and Efficacy in LM

Our overall goal for IT administered NPs is to improve drug delivery to LM in MB. In Chapters 3 and 4, we showed 100 nm NPs achieve widespread distribution along the neuraxis and penetrate into LM lesions. However, as discussed, the encapsulated payload will have its own fate compared to the intact NP. Although we did not observe a significant change in NP fate with CGKRK targeting, as discussed in Chapter 4, it is still possible for the ligand to prolong NP-cell interactions resulting in increased payload delivery. Before returning to *in vivo* studies, we would be interested to test the effects of altering ligand density, or PEG length, using an *in vitro* flow cell, to improve the strength of peptide binding[213,221]. By radiolabeling the drug, the use of PET-MRI should enable us to track drug delivery to localized groups of lesions and monitor the tumors responses within the same subject[222,223]. Therapeutic efficacy is the ultimate goal and test of a NP system. One of the believed limitations of current IT therapies is a lack of penetration into the lesions; therefore, our observation of NP penetration into most lesions could provide a significant benefit. Using post-survival tissue, it would be important to look for markers of drug activity within the lesions to see how well the drug is transported into the core of lesions. Similarly, we would want to look for drug activity in the healthy parenchyma, as the lack of penetration of the NPs into the parenchyma is expected to help reduce drug toxicity to healthy tissue. Current treatments are largely ineffective at providing a significant survival benefit in LM. Together, these studies would expand our understanding into the requirements to achieve cellular and lesion responses to treatment and how those responses translate to survival.

To expand these studies, we would also propose to further develop our nanoparticles for prolonged release. While the ~24 hr release of CPT from PLGA NPs was sufficient to improve tolerability in chapter 2, the burst release profile observed for

these NPs would not be able to fully take advantage of the prolonged 3 week retention observed for NPs within the CSF. At the 100 nm size, we would not expect to achieve adequate drug concentrations for 3 weeks but alterations to NP design could still enable prolonged release compared to the PLGA NPs. For example, the addition of a lipid monolayer around the PLGA NPs has previously been shown to prolong the release of docetaxol from 3 days to over 5 days[224]. More complex release mechanisms utilizing covalently attached drug could also be tested. For example, attachment of drugs by radiation liable linkers could enable drug release only during radiation treatment[225]. Attachment of radio-sensitizing drugs by this method would be expected to enhance radiation efficacy and potentially reduce the necessary dose. We could also explore larger diameter NPs which could allow for larger drug doses to be delivered in a single injection. Considering we found 10 μm FS are able to transverse the leptomeninges, larger NPs may be able to achieve similar NP distributions as the 100 nm NPs. In conclusion, this body of work establishes multiple drug delivery strategies to intracranial tumors by IV or IT administration. Our future work will focus on identifying the necessary NP properties for the delivery of specific drugs to LM in MB.

REFERENCES

1. Householder, K. T. *et al.* Intravenous delivery of camptothecin-loaded PLGA nanoparticles for the treatment of intracranial glioma. *Int. J. Pharm.* **479,** 374–380 (2015).

2. Shi, D., Sadat, M. E., Dunn, A. W. & Mast, D. B. Photo-fluorescent and magnetic properties of iron oxide nanoparticles for biomedical applications. *Nanoscale* **7,** 8209–8232 (2015).

3. Cabuzu, D., Cirja, A., Puiu, R. & Grumezescu, A. M. Biomedical applications of gold nanoparticles. *Curr. Top. Med. Chem.* **15,** 1605–1613 (2015).

4. Yamada, M., Foote, M. & Prow, T. W. Therapeutic gold, silver, and platinum nanoparticles. *Wiley Interdiscip. Rev. Nanomed. Nanobiotechnol.* **7,** 428–445

5. Lohcharoenkal, W., Wang, L., Chen, Y. C. & Rojanasakul, Y. Protein Nanoparticles as Drug Delivery Carriers for Cancer Therapy. *BioMed Res. Int.* **2014,** (2014).

6. Sripriyalakshmi, S., Jose, P., Ravindran, A. & Anjali, C. H. Recent trends in drug delivery system using protein nanoparticles. *Cell Biochem. Biophys.* **70,** 17–26 (2014).

7. Bozzuto, G. & Molinari, A. Liposomes as nanomedical devices. *Int. J. Nanomedicine* **10,** 975–999 (2015).

8. Madni, A. *et al.* Liposomal drug delivery: a versatile platform for challenging clinical applications. *J. Pharm. Pharm. Sci. Publ. Can. Soc. Pharm. Sci. Soc. Can. Sci. Pharm.* **17,** 401–426 (2014).

9. Ma, Y., Nolte, R. J. M. & Cornelissen, J. J. L. M. Virus-based nanocarriers for drug delivery. *Adv. Drug Deliv. Rev.* **64,** 811–825 (2012).

10. Lai, P., Daear, W., Löbenberg, R. & Prenner, E. J. Overview of the preparation of organic polymeric nanoparticles for drug delivery based on gelatine, chitosan, poly(d,l-lactide-co-glycolic acid) and polyalkylcyanoacrylate. *Colloids Surf. B Biointerfaces* **118,** 154–163 (2014).

11. Priya James, H., John, R., Alex, A. & Anoop, K. R. Smart polymers for the controlled delivery of drugs – a concise overview. *Acta Pharm. Sin. B* doi:10.1016/j.apsb.2014.02.005

12. Grottkau, B. E., Cai, X., Wang, J., Yang, X. & Lin, Y. Polymeric nanoparticles for a drug delivery system. *Curr. Drug Metab.* **14,** 840–846 (2013).

13. Bulbake, U., Doppalapudi, S., Kommineni, N. & Khan, W. Liposomal Formulations in Clinical Use: An Updated Review. *Pharmaceutics* **9,** (2017).

14. Anselmo, A. C. & Mitragotri, S. Nanoparticles in the clinic. *Bioeng. Transl. Med.* **1,** 10–29 (2016).

15. Bawa, R., Audette, G. F. & Rubinstein, I. *Handbook of Clinical Nanomedicine: Nanoparticles, Imaging, Therapy, and Clinical Applications*. (CRC Press, 2016).

16. Navarro, G., Pan, J. & Torchilin, V. P. Micelle-like nanoparticles as carriers for DNA and siRNA. *Mol. Pharm.* **12,** 301–313 (2015).

17. Scripture, C. D., Figg, W. D. & Sparreboom, A. Paclitaxel chemotherapy: from empiricism to a mechanism-based formulation strategy. *Ther. Clin. Risk Manag.* **1,** 107–114 (2005).

18. Park, I. H. *et al.* An Open-Label, Randomized, Parallel, Phase III Trial Evaluating the Efficacy and Safety of Polymeric Micelle-Formulated Paclitaxel Compared to Conventional Cremophor EL-Based Paclitaxel for Recurrent or Metastatic HER2-Negative Breast Cancer. *Cancer Res. Treat. Off. J. Korean Cancer Assoc.* **49,** 569–577 (2017).

19. Cirpanli, Y., Bilensoy, E., Dogan, A. L. & Calis, S. Development of polymeric and cyclodextrin nanoparticles for camptothecin delivery. *J. Controlled Release* **148,** e21–e23 (2010).

20. Zhao, Y. & Huang, L. Lipid Nanoparticles for Gene Delivery. *Adv. Genet.* **88,** 13–36 (2014).

21. Pereira, G. C. *et al.* Drug-induced cardiac mitochondrial toxicity and protection: from doxorubicin to carvedilol. *Curr. Pharm. Des.* **17,** 2113–2129 (2011).

22. Theodoulou, M. & Hudis, C. Cardiac profiles of liposomal anthracyclines: greater cardiac safety versus conventional doxorubicin? *Cancer* **100,** 2052–2063 (2004).

23. Sunoqrot, S., Bugno, J., Lantvit, D., Burdette, J. E. & Hong, S. Prolonged blood circulation and enhanced tumor accumulation of folate-targeted dendrimer-polymer hybrid nanoparticles. *J. Control. Release Off. J. Control. Release Soc.* **191,** 115–122 (2014).

24. Klibanov, A. L., Maruyama, K., Torchilin, V. P. & Huang, L. Amphipathic polyethyleneglycols effectively prolong the circulation time of liposomes. *FEBS Lett.* **268,** 235–237 (1990).

25. Barenholz, Y. Doxil®--the first FDA-approved nano-drug: lessons learned. *J. Control. Release Off. J. Control. Release Soc.* **160,** 117–134 (2012).

26. Mistry, A. *et al.* Effect of physicochemical properties on intranasal nanoparticle transit into murine olfactory epithelium. *J. Drug Target.* **17,** 543–552 (2009).

27. Hrkach, J. *et al.* Preclinical Development and Clinical Translation of a PSMA-Targeted Docetaxel Nanoparticle with a Differentiated Pharmacological Profile. *Sci. Transl. Med.* **4,** 128ra39-128ra39 (2012).

28. Kamaly, N., Xiao, Z., Valencia, P. M., Radovic-Moreno, A. F. & Farokhzad, O. C. Targeted polymeric therapeutic nanoparticles: design, development and clinical translation. *Chem. Soc. Rev.* **41,** 2971–3010 (2012).

29. Stylianopoulos, T. & Jain, R. K. Design considerations for nanotherapeutics in oncology. *Nanomedicine Nanotechnol. Biol. Med.* **11,** 1893–1907 (2015).

30. Kulkarni, S. A. & Feng, S.-S. Effects of Particle Size and Surface Modification on Cellular Uptake and Biodistribution of Polymeric Nanoparticles for Drug Delivery. *Pharm. Res.* **30,** 2512–2522 (2013).

31. Sonavane, G., Tomoda, K. & Makino, K. Biodistribution of colloidal gold nanoparticles after intravenous administration: effect of particle size. *Colloids Surf. B Biointerfaces* **66,** 274–280 (2008).

32. Yadav, K. S., Chuttani, K., Mishra, A. K. & Sawant, K. K. Effect of Size on the Biodistribution and Blood Clearance of Etoposide-Loaded PLGA Nanoparticles. *PDA J. Pharm. Sci. Technol.* **65,** 131–139 (2011).

33. Desai, J. & Thakkar, H. Effect of particle size on oral bioavailability of darunavir-loaded solid lipid nanoparticles. *J. Microencapsul.* **33,** 669–678 (2016).

34. Ensign, L. M., Cone, R. & Hanes, J. Oral Drug Delivery with Polymeric Nanoparticles: The Gastrointestinal Mucus Barriers. *Adv. Drug Deliv. Rev.* **64,** 557–570 (2012).

35. Mistry, A., Stolnik, S. & Illum, L. Nose-to-Brain Delivery: Investigation of the Transport of Nanoparticles with Different Surface Characteristics and Sizes in Excised Porcine Olfactory Epithelium. *Mol. Pharm.* **12,** 2755–2766 (2015).

36. Mistry, A., Stolnik, S. & Illum, L. Nanoparticles for direct nose-to-brain delivery of drugs. *Int. J. Pharm.* **379,** 146–157 (2009).

37. MacKay, J. A., Deen, D. F. & Szoka, F. C. Distribution in brain of liposomes after convection enhanced delivery; modulation by particle charge, particle diameter, and presence of steric coating. *Brain Res.* **1035,** 139–153 (2005).

38. Nance, E. A. *et al.* A Dense Poly(ethylene glycol) Coating Improves Penetration of Large Polymeric Nanoparticles within Brain Tissue. *Sci. Transl. Med.* **4,** 149ra119 (2012).

39. Choi, H. S. *et al.* Renal Clearance of Nanoparticles. *Nat. Biotechnol.* **25,** 1165–1170 (2007).

40. Longmire, M., Choyke, P. L. & Kobayashi, H. Clearance Properties of Nano-sized Particles and Molecules as Imaging Agents: Considerations and Caveats. *Nanomed.* **3,** 703–717 (2008).

41. Mishra, D., Hubenak, J. R. & Mathur, A. B. Nanoparticle systems as tools to improve drug delivery and therapeutic efficacy. *J. Biomed. Mater. Res. A* **101,** 3646–3660

42. Ferrari, R. *et al.* Investigation of size, surface charge, PEGylation degree and concentration on the cellular uptake of polymer nanoparticles. *Colloids Surf. B Biointerfaces* **123,** 639–647 (2014).

43. Fröhlich, E. The role of surface charge in cellular uptake and cytotoxicity of medical nanoparticles. *Int. J. Nanomedicine* **7,** 5577–5591 (2012).

44. Boegh, M. & Nielsen, H. M. Mucus as a barrier to drug delivery – understanding and mimicking the barrier properties. *Basic Clin. Pharmacol. Toxicol.* **116,** 179–186 (2015).

45. Sonvico, F. *et al.* Surface-Modified Nanocarriers for Nose-to-Brain Delivery: From Bioadhesion to Targeting. *Pharmaceutics* **10,** (2018).

46. Suk, J. S., Xu, Q., Kim, N., Hanes, J. & Ensign, L. M. PEGylation as a strategy for improving nanoparticle-based drug and gene delivery. *Adv. Drug Deliv. Rev.* **99,** 28–51 (2016).

47. Saito, R. *et al.* Tissue affinity of the infusate affects the distribution volume during convection-enhanced delivery into rodent brains: implications for local drug delivery. *J. Neurosci. Methods* **154,** 225–232 (2006).

48. Pelaz, B. *et al.* Surface Functionalization of Nanoparticles with Polyethylene Glycol: Effects on Protein Adsorption and Cellular Uptake. *ACS Nano* **9,** 6996–7008 (2015).

49. Chen, M. Y. *et al.* Surface properties, more than size, limiting convective distribution of virus-sized particles and viruses in the central nervous system. *J. Neurosurg.* **103,** 311–319 (2005).

50. Schneider, C. S. *et al.* Minimizing the non-specific binding of nanoparticles to the brain enables active targeting of Fn14-positive glioblastoma cells. *Biomaterials* **42,** 42–51 (2015).

51. Davis, M. E. The first targeted delivery of siRNA in humans via a self-assembling, cyclodextrin polymer-based nanoparticle: from concept to clinic. *Mol. Pharm.* **6,** 659–668 (2009).

52. Pillai, G. J., Greeshma, M. M. & Menon, D. Impact of poly(lactic-co-glycolic acid) nanoparticle surface charge on protein, cellular and haematological interactions. *Colloids Surf. B Biointerfaces* **136,** 1058–1066 (2015).

53. Avgoustakis, K. Pegylated poly(lactide) and poly(lactide-co-glycolide) nanoparticles: preparation, properties and possible applications in drug delivery. *Curr. Drug Deliv.* **1,** 321–333 (2004).

54. Jokerst, J. V., Lobovkina, T., Zare, R. N. & Gambhir, S. S. Nanoparticle PEGylation for imaging and therapy. *Nanomed.* **6,** 715–728 (2011).

55. Bae, Y. H. & Park, K. Targeted drug delivery to tumors: Myths, reality and possibility. *J. Controlled Release* **153,** 198–205 (2011).

56. Costa, P. M. *et al.* Tumor-targeted Chlorotoxin-coupled Nanoparticles for Nucleic Acid Delivery to Glioblastoma Cells: A Promising System for Glioblastoma Treatment. *Mol. Ther. Nucleic Acids* **2,** e100 (2013).

57. Chung, E. J. *et al.* Fibrin-binding, peptide amphiphile micelles for targeting glioblastoma. *Biomaterials* **35,** 1249–1256 (2014).

58. Sá, L. T. M., Simmons, S., Missailidis, S., da Silva, M. I. P. & Santos-Oliveira, R. Aptamer-based nanoparticles for cancer targeting. *J. Drug Target.* **21,** 427–434 (2013).

59. Zhou, W. *et al.* Aptamer-nanoparticle bioconjugates enhance intracellular delivery of vinorelbine to breast cancer cells. *J. Drug Target.* **22,** 57–66 (2014).

60. Guo, J. *et al.* Aptamer-functionalized PEG-PLGA nanoparticles for enhanced anti-glioma drug delivery. *Biomaterials* **32,** 8010–8020 (2011).

61. Cardoso, M. M., Peça, I. N. & Roque, A. C. A. Antibody-conjugated nanoparticles for therapeutic applications. *Curr. Med. Chem.* **19,** 3103–3127 (2012).

62. Han, H. & Davis, M. E. Single-Antibody, Targeted Nanoparticle Delivery of Camptothecin. *Mol. Pharm.* **10,** 2558–2567 (2013).

63. Loureiro, J. A., Gomes, B., Coelho, M. A. N., do Carmo Pereira, M. & Rocha, S. Targeting nanoparticles across the blood-brain barrier with monoclonal antibodies. *Nanomed.* **9,** 709–722 (2014).

64. Kwon, I. K., Lee, S. C., Han, B. & Park, K. Analysis on the current status of targeted drug delivery to tumors. *J. Control. Release Off. J. Control. Release Soc.* **164,** (2012).

65. Lee, K. J. *et al.* Novel peptides functionally targeting in vivo human lung cancer discovered by in vivo peptide displayed phage screening. *Amino Acids* **47,** 281–289 (2015).

66. Molek, P., Strukelj, B. & Bratkovic, T. Peptide Phage Display as a Tool for Drug Discovery: Targeting Membrane Receptors. *Molecules* **16,** 857–887 (2011).

67. Darmostuk, M., Rimpelova, S., Gbelcova, H. & Ruml, T. Current approaches in SELEX: An update to aptamer selection technology. *Biotechnol. Adv.* **33,** 1141–1161 (2015).

68. Szeto, K. *et al.* RAPID-SELEX for RNA aptamers. *PloS One* **8,** e82667 (2013).

69. Cook, R. L. *et al.* A critical evaluation of drug delivery from ligand modified nanoparticles: Confounding small molecule distribution and efficacy in the central nervous system. *J. Control. Release Off. J. Control. Release Soc.* **220,** 89–97 (2015).

70. Gao, H. *et al.* RGD and Interleukin-13 Peptide Functionalized Nanoparticles for Enhanced Glioblastoma Cells and Neovasculature Dual Targeting Delivery and Elevated Tumor Penetration. *Mol. Pharm.* **11,** 1042–1052 (2014).

71. Brooks, H., Lebleu, B. & Vivès, E. Tat peptide-mediated cellular delivery: back to basics. *Adv. Drug Deliv. Rev.* **57,** 559–577 (2005).

72. Todorova, N. *et al.* Surface presentation of functional peptides in solution determines cell internalization efficiency of TAT conjugated nanoparticles. *Nano Lett.* **14,** 5229–5237 (2014).

73. Mallick, A. *et al.* Dual Drug Conjugated Nanoparticle for Simultaneous Targeting of Mitochondria and Nucleus in Cancer Cells. *ACS Appl. Mater. Interfaces* **7,** 7584–7598 (2015).

74. Field, L. D., Delehanty, J. B., Chen, Y. & Medintz, I. L. Peptides for Specifically Targeting Nanoparticles to Cellular Organelles: Quo Vadis? *Acc. Chem. Res.* **48,** 1380–1390 (2015).

75. Kamaly, N., Yameen, B., Wu, J. & Farokhzad, O. C. Degradable Controlled-Release Polymers and Polymeric Nanoparticles: Mechanisms of Controlling Drug Release. *Chem. Rev.* **116,** 2602–2663 (2016).

76. Hussain, M. *et al.* Regulation of Drug Release by Tuning Surface Textures of Biodegradable Polymer Microparticles. *ACS Appl. Mater. Interfaces* **9,** 14391–14400 (2017).

77. Swanson, L. J., Seely, J. H. & Garnick, M. B. Gonadotropin-releasing hormone analogs and prostatic cancer. *Crit. Rev. Oncol. Hematol.* **8,** 1–26 (1988).

78. Okada, H. & Toguchi, H. Biodegradable microspheres in drug delivery. *Crit. Rev. Ther. Drug Carrier Syst.* **12,** 1–99 (1995).

79. Langer, R. & Folkman, J. Polymers for the sustained release of proteins and other macromolecules. *Nature* **263,** 797–800 (1976).

80. Zamboni, W. C. *et al.* Systemic and tumor disposition of platinum after administration of cisplatin or STEALTH liposomal-cisplatin formulations (SPI-077 and SPI-077 B103) in a preclinical tumor model of melanoma. *Cancer Chemother. Pharmacol.* **53,** 329–336 (2004).

81. Kim, S. *et al.* Extended CSF cytarabine exposure following intrathecal administration of DTC 101. *J. Clin. Oncol.* **11,** 2186–2193 (1993).

82. Dengler, E. C. *et al.* Mesoporous silica-supported lipid bilayers (protocells) for DNA cargo delivery to the spinal cord. *J. Control. Release Off. J. Control. Release Soc.* **168,** 209–224 (2013).

83. Soderquist, R. G. *et al.* Release of Plasmid DNA-Encoding IL-10 from PLGA Microparticles Facilitates Long-Term Reversal of Neuropathic Pain Following a Single Intrathecal Administration. *Pharm. Res.* **27,** 841–854 (2010).

84. Donaghue, I. E., H. Tator, C. & S. Shoichet, M. Sustained delivery of bioactive neurotrophin-3 to the injured spinal cord. *Biomater. Sci.* **3,** 65–72 (2015).

85. Cerqueira Susana R. *et al.* Microglia Response and In Vivo Therapeutic Potential of Methylprednisolone-Loaded Dendrimer Nanoparticles in Spinal Cord Injury. *Small* **9,** 738–749 (2013).

86. Tan, J. *et al.* Changes in compressed neurons from dogs with acute and severe cauda equina constrictions following intrathecal injection of brain-derived neurotrophic factor-conjugated polymer nanoparticles. *Neural Regen. Res.* **8,** 233–243 (2013).

87. Bomgaars, L. *et al.* Phase I trial of intrathecal liposomal cytarabine in children with neoplastic meningitis. *J. Clin. Oncol. Off. J. Am. Soc. Clin. Oncol.* **22,** 3916–3921 (2004).

88. Chamberlain, M. C. Neurotoxicity of intra-CSF liposomal cytarabine (DepoCyt) administered for the treatment of leptomeningeal metastases: a retrospective case series. *J. Neurooncol.* **109,** 143–148 (2012).

89. Moreno, L. *et al.* Liposomal cytarabine for the treatment of leptomeningeal dissemination of central nervous system tumours in children and adolescents. *An. Pediatría Engl. Ed.* **85,** 274.e1-274.e8 (2016).

90. Shapiro, W. R., Schmid, M., Glantz, M. & Miller, J. J. A randomized phase III/IV study to determine benefit and safety of cytarabine liposome injection for treatment of neoplastic meningitis. *J. Clin. Oncol.* **24,** 1528–1528 (2006).

91. Glantz, M. J. *et al.* Randomized Trial of a Slow-Release Versus a Standard Formulation of Cytarabine for the Intrathecal Treatment of Lymphomatous Meningitis. *J. Clin. Oncol.* **17,** 3110–3116 (1999).

92. Brinker, T., Stopa, E., Morrison, J. & Klinge, P. A new look at cerebrospinal fluid circulation. *Fluids Barriers CNS* **11,** 10 (2014).

93. Sakka, L., Coll, G. & Chazal, J. Anatomy and physiology of cerebrospinal fluid. *Eur. Ann. Otorhinolaryngol. Head Neck Dis.* **128,** 309–316 (2011).

94. Spector, R., Robert Snodgrass, S. & Johanson, C. E. A balanced view of the cerebrospinal fluid composition and functions: Focus on adult humans. *Exp. Neurol.* **273,** 57–68 (2015).

95. Simon, M. J. & Iliff, J. J. Regulation of cerebrospinal fluid (CSF) flow in neurodegenerative, neurovascular and neuroinflammatory disease. *Biochim. Biophys. Acta BBA - Mol. Basis Dis.* **1862,** 442–451 (2016).

96. Tangen, K. M., Hsu, Y., Zhu, D. C. & Linninger, A. A. CNS wide simulation of flow resistance and drug transport due to spinal microanatomy. *J. Biomech.* **48,** 2144–2154 (2015).

97. Ridgway, J. P., Turnbull, L. W. & Smith, M. A. Demonstration of pulsatile cerebrospinal-fluid flow using magnetic resonance phase imaging. *Br. J. Radiol.* **60,** 423–427 (1987).

98. Yamada, S. *et al.* Visualization of Cerebrospinal Fluid Movement with Spin Labeling at MR Imaging: Preliminary Results in Normal and Pathophysiologic Conditions. *Radiology* **249,** 644–652 (2008).

99. Rudick, R. A., Zirretta, D. K. & Herndon, R. M. Clearance of albumin from mouse subarachnoid space: a measure of CSF bulk flow. *J. Neurosci. Methods* **6,** 253–259 (1982).

100. Coluccia, D., Figuereido, C., Isik, S., Smith, C. & Rutka, J. T. Medulloblastoma: Tumor Biology and Relevance to Treatment and Prognosis Paradigm. *Curr. Neurol. Neurosci. Rep.* **16,** 43 (2016).

101. DeSouza, R.-M., Jones, B. R. T., Lowis, S. P. & Kurian, K. M. Pediatric Medulloblastoma – Update on Molecular Classification Driving Targeted Therapies. *Front. Oncol.* **4,** (2014).

102. Northcott, P. A. *et al.* Medulloblastoma Comprises Four Distinct Molecular Variants. *J. Clin. Oncol.* **29,** 1408–1414 (2011).

103. Wetmore, C. *et al.* Reirradiation of recurrent medulloblastoma: does clinical benefit outweigh risk for toxicity? *Cancer* **120,** 3731–3737 (2014).

104. Massimino, M. *et al.* No salvage using high-dose chemotherapy plus/minus reirradiation for relapsing previously irradiated medulloblastoma. *Int. J. Radiat. Oncol. Biol. Phys.* **73,** 1358–1363 (2009).

105. McDonald, M. W., Wolanski, M. R., Simmons, J. W. & Buchsbaum, J. C. Technique for sparing previously irradiated critical normal structures in salvage proton craniospinal irradiation. *Radiat. Oncol. Lond. Engl.* **8,** 14 (2013).

106. Blakeley, J. Drug Delivery to Brain Tumors. *Curr. Neurol. Neurosci. Rep.* **8,** 235–241 (2008).

107. Bhowmik, A., Khan, R. & Ghosh, M. K. Blood Brain Barrier: A Challenge for Effectual Therapy of Brain Tumors. *BioMed Res. Int.* **2015,** (2015).

108. Berg, S. L. & Poplack, D. G. Treatment of Meningeal Malignancy. *The Oncologist* **1,** 56–61 (1996).

109. Bottros, M. M. & Christo, P. J. Current perspectives on intrathecal drug delivery. *J. Pain Res.* **7,** 615–626 (2014).

110. Brinker, T., Stopa, E., Morrison, J. & Klinge, P. A new look at cerebrospinal fluid circulation. *Fluids Barriers CNS* **11,** 10 (2014).

111. Stienstra, R. & Veering, B. T. Intrathecal drug spread: Is it controllable? *Reg. Anesth. Pain Med.* **23,** 347–351 (1998).

112. Kuttler, A. *et al.* Understanding pharmacokinetics using realistic computational models of fluid dynamics: biosimulation of drug distribution within the CSF space for intrathecal drugs. *J. Pharmacokinet. Pharmacodyn.* **37,** 629–644 (2010).

113. Papisov, M. I., Belov, V. V. & Gannon, K. S. Physiology of the intrathecal bolus: the leptomeningeal route for macromolecule and particle delivery to CNS. *Mol. Pharm.* **10,** 1522–1532 (2013).

114. Blaney, S. M. & Poplack, D. G. New cytotoxic drugs for intrathecal administration. *J. Neurooncol.* **38,** 219–223 (1998).

115. Canova, F. *et al.* Intrathecal chemotherapy in lymphomatous meningitis. *Crit. Rev. Oncol. Hematol.* **79,** 127–134 (2011).

116. Gwak, H.-S. *et al.* Recent Advancements of Treatment for Leptomeningeal Carcinomatosis. *J. Korean Neurosurg. Soc.* **58,** 1–8 (2015).

117. Hayakawa, T. *et al.* Intrathecal Chemotherapy. *Br. J. Cancer* **24,** 489–497 (1970).

118. Kwong, Y.-L., Yeung, D. Y. M. & Chan, J. C. W. Intrathecal chemotherapy for hematologic malignancies: drugs and toxicities. *Ann. Hematol.* **88,** 193–201 (2009).

119. Ruggiero, A. *et al.* Intrathecal chemotherapy with antineoplastic agents in children. *Paediatr. Drugs* **3,** 237–246 (2001).

120. Yoshimura, J., Nishiyama, K., Mori, H., Takahashi, H. & Fujii, Y. Intrathecal chemotherapy for refractory disseminated medulloblastoma. *Childs Nerv. Syst. ChNS Off. J. Int. Soc. Pediatr. Neurosurg.* **24,** 581–585 (2008).

121. Zimm, S., Collins, J. M., Miser, J., Chatterji, D. & Poplack, D. G. Cytosine arabinoside cerebrospinal fluid kinetics. *Clin. Pharmacol. Ther.* **35,** 826–830 (1984).

122. Bokstein, F., Lossos, A. & Siegal, T. Leptomeningeal metastases from solid tumors: a comparison of two prospective series treated with and without intra-cerebrospinal fluid chemotherapy. *Cancer* **82,** 1756–1763 (1998).

123. Kitamura, I. *et al.* Intrathecal chemotherapy with 1,3-bis(2-chloroethyl)-1-nitrosourea encapsulated into hybrid liposomes for meningeal gliomatosis: an experimental study. *Cancer Res.* **56,** 3986–3992 (1996).

124. Wolf, D. A. *et al.* Dynamic dual-isotope molecular imaging elucidates principles for optimizing intrathecal drug delivery. *JCI Insight* **1,** (2016).

125. Ummenhofer, W. C., Arends, R. H., Shen, D. D. & Bernards, C. M. Comparative Spinal Distribution and Clearance Kinetics of Intrathecally Administered Morphine, Fentanyl, Alfentanil, and Sufentanil. *J. Am. Soc. Anesthesiol.* **92,** 739–753 (2000).

126. Friedman, H. S., Kerby, T. & Calvert, H. Temozolomide and treatment of malignant glioma. *Clin. Cancer Res. Off. J. Am. Assoc. Cancer Res.* **6,** 2585–2597 (2000).

127. Grossman, S. A. & Batara, J. F. Current management of glioblastoma multiforme. *Semin. Oncol.* **31,** 635–644 (2004).

128. Yang, L.-J., Zhou, C.-F. & Lin, Z.-X. Temozolomide and radiotherapy for newly diagnosed glioblastoma multiforme: a systematic review. *Cancer Invest.* **32,** 31–36 (2014).

129. Mross, K. *et al.* A phase I clinical and pharmacokinetic study of the camptothecin glycoconjugate, BAY 38-3441, as a daily infusion in patients with advanced solid tumors. *Ann. Oncol.* **15,** 1284–1294 (2004).

130. Dawidczyk, C. M., Russell, L. M. & Searson, P. C. Nanomedicines for cancer therapy: state-of-the-art and limitations to pre-clinical studies that hinder future developments. *Chem. Eng.* **2,** 69 (2014).

131. Dinarvand, R., Sepehri, N., Manoochehri, S., Rouhani, H. & Atyabi, F. Polylactide-co-glycolide nanoparticles for controlled delivery of anticancer agents. *Int. J. Nanomedicine* **6,** 877–895 (2011).

132. Tosi, G. *et al.* Potential use of polymeric nanoparticles for drug delivery across the blood-brain barrier. *Curr. Med. Chem.* **20,** 2212–2225 (2013).

133. Sawyer, A. J. *et al.* Convection-enhanced delivery of camptothecin-loaded polymer nanoparticles for treatment of intracranial tumors. *Drug Deliv. Transl. Res.* **1,** 34–42 (2011).

134. Jacobs, V. L., Valdes, P. A., Hickey, W. F. & De Leo, J. A. Current review of in vivo GBM rodent models: emphasis on the CNS-1 tumour model. *ASN NEURO* **3,** (2011).

135. Newcomb, E. W. & Zagzag, D. The Murine GL261 Glioma Experimental Model to Assess Novel Brain Tumor Treatments. in *CNS Cancer* (ed. Meir, E. G.) 227–241 (Humana Press, 2009).

136. McCall, R. L. & Sirianni, R. W. PLGA nanoparticles formed by single- or double-emulsion with vitamin E-TPGS. *J. Vis. Exp. JoVE* 51015 (2013). doi:10.3791/51015

137. Deng, Y. *et al.* The effect of hyperbranched polyglycerol coatings on drug delivery using degradable polymer nanoparticles. *Biomaterials* **35,** 6595–6602 (2014).

138. Abdelwahab, M. G., Sankar, T., Preul, M. C. & Scheck, A. C. Intracranial Implantation with Subsequent 3D In Vivo Bioluminescent Imaging of Murine Gliomas. *J. Vis. Exp.* (2011). doi:10.3791/3403

139. Dhruv, H. D. *et al.* Reciprocal Activation of Transcription Factors Underlies the Dichotomy between Proliferation and Invasion of Glioma Cells. *PLoS ONE* **8,** e72134 (2013).

140. Lu, J. *et al.* Free paclitaxel loaded PEGylated-paclitaxel nanoparticles: preparation and comparison with other paclitaxel systems in vitro and in vivo. *Int. J. Pharm.* **471,** 525–535 (2014).

141. Yao, J. *et al.* Nanoparticle delivery and combination therapy of gambogic acid and all-trans retinoic acid. *Int. J. Nanomedicine* **9,** 3313–3324 (2014).

142. Fox, S. B. *et al.* Relationship of Endothelial Cell Proliferation to Tumor Vascularity in Human Breast Cancer. *Cancer Res.* **53,** 4161–4163 (1993).

143. McCarron, P. A. *et al.* Antibody Targeting of Camptothecin-Loaded PLGA Nanoparticles to Tumor Cells. *Bioconjug. Chem.* **19,** 1561–1569 (2008).

144. Seligman, A. M., Shear, M. J. & Alexander, L. Studies in Carcinogenesis: VIII. Experimental Production of Brain Tumors in Mice with Methylcholanthrene. *Am. J. Cancer* **37,** 364–395 (1939).

145. Szatmári, T. *et al.* Detailed characterization of the mouse glioma 261 tumor model for experimental glioblastoma therapy. *Cancer Sci.* **97,** 546–553 (2006).

146. Oh, T. *et al.* Immunocompetent murine models for the study of glioblastoma immunotherapy. *J. Transl. Med.* **12,** 107 (2014).

147. Clark, A. J. *et al.* Stable luciferase expression does not alter immunologic or in vivo growth properties of GL261 murine glioma cells. *J. Transl. Med.* **12,** (2014).

148. Acharya, S. & Sahoo, S. K. PLGA nanoparticles containing various anticancer agents and tumour delivery by EPR effect. *Adv. Drug Deliv. Rev.* **63,** 170–183 (2011).

149. Fang, J., Nakamura, H. & Maeda, H. The EPR effect: Unique features of tumor blood vessels for drug delivery, factors involved, and limitations and augmentation of the effect. *Adv. Drug Deliv. Rev.* **63,** 136–151 (2011).

150. Greish, K. Enhanced Permeability and Retention (EPR) Effect for Anticancer Nanomedicine Drug Targeting. in *Cancer Nanotechnology* (eds. Grobmyer, S. R. & Moudgil, B. M.) 25–37 (Humana Press, 2010).

151. Prabhakar, U. *et al.* Challenges and key considerations of the enhanced permeability and retention (EPR) effect for nanomedicine drug delivery in oncology. *Cancer Res.* **73,** 2412–2417 (2013).

152. Furuta, T. *et al.* Phosphorylation of Histone H2AX and Activation of Mre11, Rad50, and Nbs1 in Response to Replication-dependent DNA Double-strand Breaks Induced by Mammalian DNA Topoisomerase I Cleavage Complexes. *J. Biol. Chem.* **278,** 20303–20312 (2003).

153. McCall, R. L. *et al.* Pathogen-inspired drug delivery to the central nervous system. *Tissue Barriers* e944449 (2014). doi:10.4161/21688362.2014.944449

154. Pardridge, W. M. The Blood-Brain Barrier: Bottleneck in Brain Drug Development. *NeuroRx* **2,** 3–14 (2005).

155. Beck, M. *et al.* Autonomic dysfunction in ALS: A preliminary study on the effects of intrathecal BDNF. *Amyotroph. Lateral Scler. Other Motor Neuron Disord.* **6,** 100–103 (2005).

156. Ghersi-Egea, J. F. *et al.* Fate of cerebrospinal fluid-borne amyloid beta-peptide: rapid clearance into blood and appreciable accumulation by cerebral arteries. *J. Neurochem.* **67,** 880–883 (1996).

157. Nutt, J. G. *et al.* Randomized, double-blind trial of glial cell line-derived neurotrophic factor (GDNF) in PD. *Neurology* **60,** 69–73 (2003).

158. Kalra, S., Genge, A. & Arnold, D. L. A prospective, randomized, placebo-controlled evaluation of corticoneuronal response to intrathecal BDNF therapy in ALS using magnetic resonance spectroscopy: feasibility and results. *Amyotroph. Lateral Scler. Mot. Neuron Disord. Off. Publ. World Fed. Neurol. Res. Group Mot. Neuron Dis.* **4,** 22–26 (2003).

159. Pardridge, W. M. Drug transport in brain via the cerebrospinal fluid. *Fluids Barriers CNS* **8,** 7 (2011).

160. Papisov, M. I. *et al.* Delivery of proteins to CNS as seen and measured by positron emission tomography. *Drug Deliv. Transl. Res.* **2,** 201–209 (2012).

161. Flack, S. H. & Bernards, C. M. Cerebrospinal Fluid and Spinal Cord Distribution of Hyperbaric Bupivacaine and Baclofen during Slow Intrathecal Infusion in Pigs. *J. Am. Soc. Anesthesiol.* **112,** 165–173 (2010).

162. Swami, A. *et al.* Nanoparticles for Targeted and Temporally Controlled Drug Delivery. in *Multifunctional Nanoparticles for Drug Delivery Applications* (eds. Svenson, S. & Prud'homme, R. K.) 9–29 (Springer US, 2012).

163. Householder, K. T. *et al.* pH driven precipitation of quisinostat onto PLA-PEG nanoparticles enables treatment of intracranial glioblastoma. *Colloids Surf. B Biointerfaces* **166,** 37–44 (2018).

164. Kelly, E. J. & Yamada, S. Cerebrospinal Fluid Flow Studies and Recent Advancements. *Semin. Ultrasound CT MRI* **37,** 92–99 (2016).

165. Dengler, E. C. *et al.* Mesoporous silica-supported lipid bilayers (protocells) for DNA cargo delivery to the spinal cord. *J. Control. Release Off. J. Control. Release Soc.* **168,** 209–224 (2013).

166. Hagihara, Y., Saitoh, Y., Kaneda, Y., Kohmura, E. & Yoshimine, T. Widespread gene transfection into the central nervous system of primates. *Gene Ther.* **7,** 759–763 (2000).

167. Shyam, R. *et al.* Intraventricular Delivery of siRNA Nanoparticles to the Central Nervous System. *Mol. Ther. — Nucleic Acids* **4,** e242 (2015).

168. Gupta, S., Soellinger, M., Boesiger, P., Poulikakos, D. & Kurtcuoglu, V. Three-Dimensional Computational Modeling of Subject-Specific Cerebrospinal Fluid Flow in the Subarachnoid Space. *J. Biomech. Eng.* **131,** 021010–021010 (2008).

169. Loth, F., Yardimci, M. A. & Alperin, N. Hydrodynamic Modeling of Cerebrospinal Fluid Motion Within the Spinal Cavity. *J. Biomech. Eng.* **123,** 71–79 (2000).

170. Bluestein, D., Niu, L., Schoephoerster, R. T. & Dewanjee, M. K. Steady Flow in an Aneurysm Model: Correlation Between Fluid Dynamics and Blood Platelet Deposition. *J. Biomech. Eng.* **118,** 280–286 (1996).

171. Boussel, L. *et al.* Phase-Contrast MRI measurements in intra-cranial aneurysms in-vivo of flow patterns, velocity fields and wall shear stress: A comparison with CFD. *Magn. Reson. Med. Off. J. Soc. Magn. Reson. Med. Soc. Magn. Reson. Med.* **61,** 409–417 (2009).

172. Ma, Q., Ineichen, B. V., Detmar, M. & Proulx, S. T. Outflow of cerebrospinal fluid is predominantly through lymphatic vessels and is reduced in aged mice. *Nat. Commun.* **8,** 1434 (2017).

173. Aspelund, A. *et al.* A dural lymphatic vascular system that drains brain interstitial fluid and macromolecules. *J. Exp. Med.* **212,** 991–999 (2015).

174. Hladky, S. B. & Barrand, M. A. Mechanisms of fluid movement into, through and out of the brain: evaluation of the evidence. *Fluids Barriers CNS* **11,** 26 (2014).

175. Date, A. A., Hanes, J. & Ensign, L. M. Nanoparticles for oral delivery: design, evaluation and state-of-the-art. *J. Control. Release Off. J. Control. Release Soc.* **240,** 504–526 (2016).

176. Saboori, P. & Sadegh, A. Histology and Morphology of the Brain Subarachnoid Trabeculae. *Anat. Res. Int.* **2015,** e279814 (2015).

177. Lü, J. & Zhu, X. L. Characteristics of distribution and configuration of intracranial arachnoid membranes. *Surg. Radiol. Anat.* **27,** 472 (2005).

178. Thorne, R. G. & Nicholson, C. In vivo diffusion analysis with quantum dots and dextrans predicts the width of brain extracellular space. *Proc. Natl. Acad. Sci.* **103,** 5567–5572 (2006).

179. Lam, M. A. *et al.* The ultrastructure of spinal cord perivascular spaces: Implications for the circulation of cerebrospinal fluid. *Sci. Rep.* **7,** 12924 (2017).

180. Bazak, R., Houri, M., El Achy, S., Kamel, S. & Refaat, T. Cancer active targeting by nanoparticles: a comprehensive review of literature. *J. Cancer Res. Clin. Oncol.* **141,** 769–784 (2015).

181. Young Yhee, J., Lee, S. & Kim, K. Advances in targeting strategies for nanoparticles in cancer imaging and therapy. *Nanoscale* **6,** 13383–13390 (2014).

182. Hu, Q. *et al.* CGKRK-modified nanoparticles for dual-targeting drug delivery to tumor cells and angiogenic blood vessels. *Biomaterials* **34,** 9496–9508 (2013).

183. Bi, C. *et al.* Intranasal delivery of rotigotine to the brain with lactoferrin-modified PEG-PLGA nanoparticles for Parkinson's disease treatment. *Int. J. Nanomedicine* **11,** 6547–6559 (2016).

184. Wen, Z. *et al.* Brain targeting and toxicity study of odorranalectin-conjugated nanoparticles following intranasal administration. *Drug Deliv.* **18,** 555–561 (2011).

185. Hadjipanayis, C. G. *et al.* EGFRvIII antibody-conjugated iron oxide nanoparticles for magnetic resonance imaging-guided convection-enhanced delivery and targeted therapy of glioblastoma. *Cancer Res.* **70,** 6303–6312 (2010).

186. Weng, K. C. *et al.* Convection-enhanced delivery of targeted quantum dot-immunoliposome hybrid nanoparticles to intracranial brain tumor models. *Nanomed.* **8,** 1913–1925 (2013).

187. Lammers, T. *et al.* Cancer nanomedicine: Is targeting our target? *Nat. Rev. Mater.* **1,** (2016).

188. Pande, J., Szewczyk, M. M. & Grover, A. K. Phage display: Concept, innovations, applications and future. *Biotechnol. Adv.* **28,** 849–858 (2010).

189. Nemudraya, A. A., Richter, V. A. & Kuligina, E. V. Phage Peptide Libraries As a Source of Targeted Ligands. *Acta Naturae* **8,** 48–57 (2016).

190. Wu, C.-H., Liu, I.-J., Lu, R.-M. & Wu, H.-C. Advancement and applications of peptide phage display technology in biomedical science. *J. Biomed. Sci.* **23,** (2016).

191. Hoffman, J. A. *et al.* Progressive vascular changes in a transgenic mouse model of squamous cell carcinoma. *Cancer Cell* **4,** 383–391 (2003).

192. Lv, L. *et al.* Enhanced Antiglioblastoma Efficacy of Neovasculature and Glioma Cells Dual Targeted Nanoparticles. *Mol. Pharm.* **13,** 3506–3517 (2016).

193. Numata, K., Reagan, M. R., Goldstein, R. H., Rosenblatt, M. & Kaplan, D. L. Spider silk-based gene carriers for tumor cell-specific delivery. *Bioconjug. Chem.* **22,** 1605–1610 (2011).

194. Agemy, L. *et al.* Proapoptotic Peptide-Mediated Cancer Therapy Targeted to Cell Surface p32. *Mol. Ther.* **21,** 2195–2204 (2013).

195. Spyrou, A. *et al.* Inhibition of Heparanase in Pediatric Brain Tumor Cells Attenuates their Proliferation, Invasive Capacity, and In Vivo Tumor Growth. *Mol. Cancer Ther.* **16,** 1705–1716 (2017).

196. Giordana, M. T. *et al.* Glycosaminoglycans in human cerebral tumors. Part II. Histochemical findings and correlations. *Acta Neuropathol. (Berl.)* **57,** 299–305 (1982).

197. Zhao, J. *et al.* CREKA peptide-conjugated dendrimer nanoparticles for glioblastoma multiforme delivery. *J. Colloid Interface Sci.* **450,** 396–403 (2015).

198. Simberg, D. *et al.* Biomimetic amplification of nanoparticle homing to tumors. *Proc. Natl. Acad. Sci.* **104,** 932–936 (2007).

199. Wang, X. *et al.* Glioma and microenvironment dual targeted nanocarrier for improved antiglioblastoma efficacy. *Drug Deliv.* **24,** 1401–1409 (2017).

200. Okur, A. C., Erkoc, P. & Kizilel, S. Targeting cancer cells via tumor-homing peptide CREKA functional PEG nanoparticles. *Colloids Surf. B Biointerfaces* **147,** 191–200 (2016).

201. Li, Y., Zheng, X., Gong, M. & Zhang, J. Delivery of a peptide-drug conjugate targeting the blood brain barrier improved the efficacy of paclitaxel against glioma. *Oncotarget* **7,** 79401–79407 (2016).

202. Zhang, D. *et al.* NDRG1 promotes the multidrug resistance of neuroblastoma cells with upregulated expression of drug resistant proteins. *Biomed. Pharmacother. Biomedecine Pharmacother.* **76,** 46–51 (2015).

203. Warshawsky, I., Broze, G. J. & Schwartz, A. L. The low density lipoprotein receptor-related protein mediates the cellular degradation of tissue factor pathway inhibitor. *Proc. Natl. Acad. Sci. U. S. A.* **91,** 6664–6668 (1994).

204. Pei, Y. *et al.* An animal model of MYC-driven medulloblastoma. *Cancer Cell* **21,** 155–167 (2012).

205. Gattazzo, F., Urciuolo, A. & Bonaldo, P. Extracellular matrix: A dynamic microenvironment for stem cell niche. *Biochim. Biophys. Acta* **1840,** 2506–2519 (2014).

206. Juliano, R. L. & Haskill, S. Signal transduction from the extracellular matrix. *J. Cell Biol.* **120,** 577–585 (1993).

207. Kim, S.-H., Turnbull, J. & Guimond, S. Extracellular matrix and cell signalling: the dynamic cooperation of integrin, proteoglycan and growth factor receptor. *J. Endocrinol.* **209,** 139–151 (2011).

208. Trappmann, B. *et al.* Extracellular-matrix tethering regulates stem-cell fate. *Nat. Mater.* **11,** 642–649 (2012).

209. Zhan, C. *et al.* Cyclic RGD conjugated poly(ethylene glycol)-co-poly(lactic acid) micelle enhances paclitaxel anti-glioblastoma effect. *J. Controlled Release* **143,** 136–142 (2010).

210. Chamberlain, M. C. Spinal 111Indium-DTPA CSF flow studies in leptomeningeal metastasis. *J. Neurooncol.* **25,** 135–141 (1995).

211. Papisov, M. I. *et al.* Investigation of intrathecal transport of NPT002, a prospective therapeutic based on phage M13, in nonhuman primates. *Drug Deliv. Transl. Res.* **2,** 210–221 (2012).

212. Stefanick, J. F., Ashley, J. D. & Bilgicer, B. Enhanced Cellular Uptake of Peptide-Targeted Nanoparticles through Increased Peptide Hydrophilicity and Optimized Ethylene Glycol Peptide-Linker Length. *ACS Nano* **7,** 8115–8127 (2013).

213. Stefanick, J. F., Ashley, J. D., Kiziltepe, T. & Bilgicer, B. A Systematic Analysis of Peptide Linker Length and Liposomal Polyethylene Glycol Coating on Cellular Uptake of Peptide-Targeted Liposomes. *ACS Nano* **7,** 2935–2947 (2013).

214. Hu, Q. *et al.* Tumor Microenvironment and Angiogenic Blood Vessels Dual-Targeting for Enhanced Anti-Glioma Therapy. *ACS Appl. Mater. Interfaces* **8,** 23568–23579 (2016).

215. Medina, D. X. *et al.* Optical barcoding of PLGA for multispectral analysis of nanoparticle fate in vivo. *J. Controlled Release* **253,** 172–182 (2017).

216. Akita, H. *et al.* Effect of hydrophobic scaffold on the cellular uptake and gene transfection activities of DNA-encapsulating liposomal nanoparticles via intracerebroventricular administration. *Int. J. Pharm.* **490,** 142–145 (2015).

217. Shyam, R. *et al.* Intraventricular Delivery of siRNA Nanoparticles to the Central Nervous System. *Mol. Ther. — Nucleic Acids* **4,** e242 (2015).

218. Cherry, S. R. & Gambhir, S. S. Use of Positron Emission Tomography in Animal Research. *ILAR J.* **42,** 219–232 (2001).

219. Beiderwellen, K. *et al.* Accuracy of [18F]FDG PET/MRI for the Detection of Liver Metastases. *PloS One* **10,** e0137285 (2015).

220. Garcia, J., Tang, T. & Louie, A. Y. Nanoparticle-based multimodal PET/MRI probes. *Nanomed.* **10,** 1343–1359 (2015).

221. Elias, D. R., Poloukhtine, A., Popik, V. & Tsourkas, A. Effect of ligand density, receptor density, and nanoparticle size on cell targeting. *Nanomedicine Nanotechnol. Biol. Med.* **9,** 194–201 (2013).

222. Wang, X. *et al.* 18F-FDG PET Biomarkers Help Detect Early Metabolic Response to Irreversible Electroporation and Predict Therapeutic Outcomes in a Rat Liver Tumor Model. *Radiology* **287,** 137–145 (2018).

223. Ahn, S. Y., Goo, J. M., Lee, K. H., Ha, S. & Paeng, J. C. Monitoring tumor response to the vascular disrupting agent CKD-516 in a rabbit VX2 intramuscular tumor model using PET/MRI: Simultaneous evaluation of vascular and metabolic parameters. *PloS One* **13,** e0192706 (2018).

224. Zhang, L. *et al.* Self-Assembled Lipid–Polymer Hybrid Nanoparticles: A Robust Drug Delivery Platform. *ACS Nano* **2,** 1696–1702 (2008).

225. Ito, T., Tanabe, K., Yamada, H., Hatta, H. & Nishimoto, S. Radiation- and photo-induced activation of 5-fluorouracil prodrugs as a strategy for the selective treatment of solid tumors. *Mol. Basel Switz.* **13,** 2370–2384 (2008).

APPENDIX A

CO-AUTHOR APPROVAL OF PUBLICATION USAGE

APPENDIX A

CO-AUTHOR APPROVAL OF PUBLICATION USAGE

The co-authors of prior published works (described in the Preface) have given their consent for this material to be reproduced in this dissertation